A Charge Controlled Switched-Voltage Mode Neurostimulator

For effective, safe and efficient multi-channel intracortical visual stimulation

F. Varkevisser

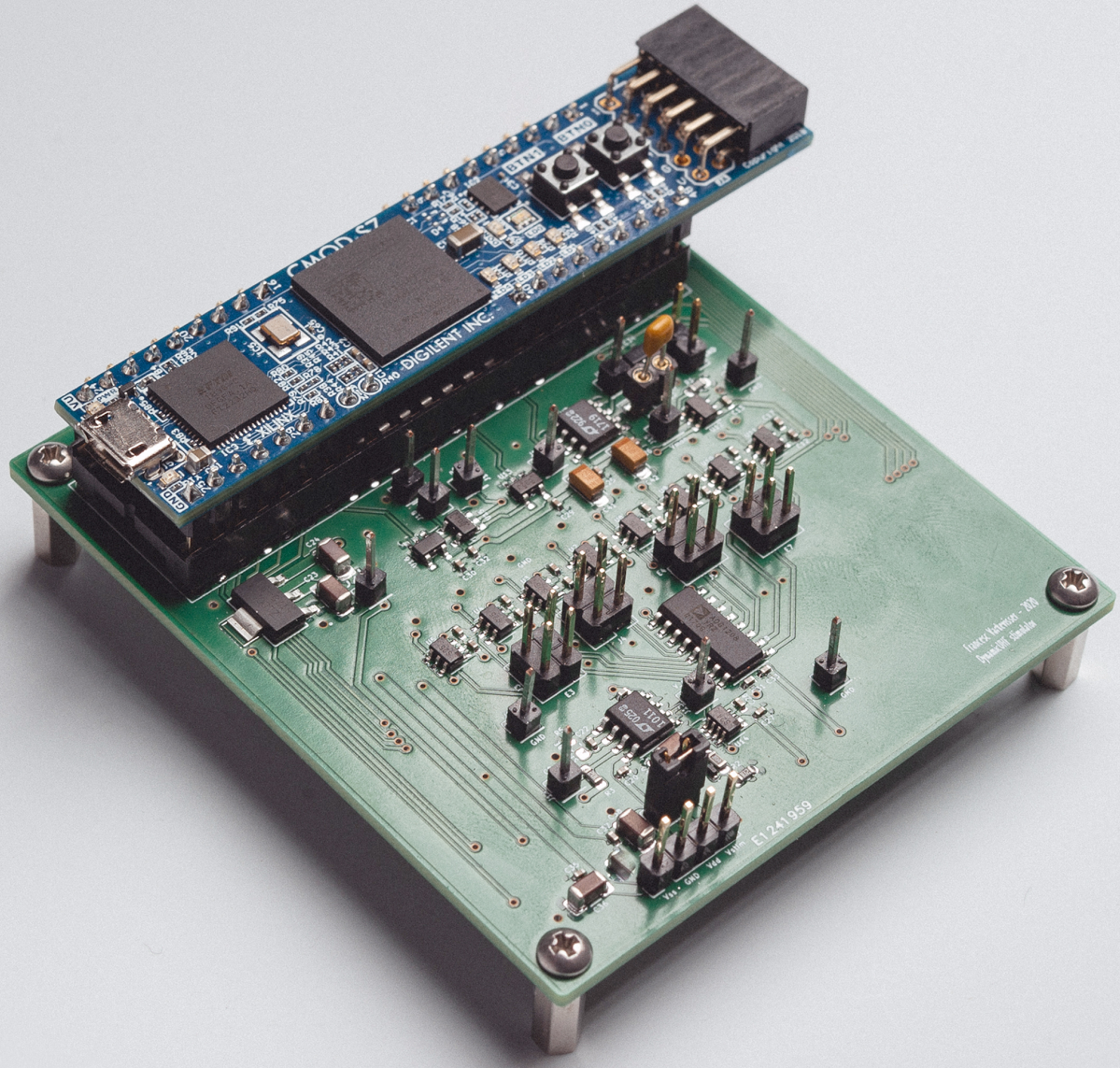

Technische Universiteit Delft

TU Delft

A Charge Controlled Switched-Voltage Mode Neurostimulator

For effective, safe and efficient multi-channel intracortical visual stimulation

by

F. Varkevisser

to obtain the degree of Master of Science
at the Delft University of Technology,
to be defended publicly on Friday November 27, 2020 at 9:30 AM.

Student number:	4362233	
Project duration:	December, 2019 – November, 2020	
Thesis committee:	Prof. dr. ir. W.A. Serdijn,	TU Delft, supervisor
	Dr. T.M.L. Costa,	TU Delft, daily supervisor
	Dr. ir. C.J.M. Verhoeven,	TU Delft

This thesis is confidential and cannot be made public until December 2021.

TU Delft

Abstract

Development of a visual prosthesis has the potential to help millions of patients with visual impairment around the world. One approach of visual prostheses is intracortical stimulation, where electrodes penetrating the visual cortex are used to create small light dots in the patients visual field. Said therapy requires an implantable neurostimulator that is able to stimulate more than 1000 micro-electrodes for sufficient resolution. Conventional stimulation methods are not suitable for this purpose as they are inefficient in multi-channel stimulation or lack control of injected charge.

In this thesis a novel stimulation method is presented based on dynamic duty cycle control of ultra high frequency (UHF) pulses. The duty cycle is charge-controlled using a monostable multivibrator control loop. With this novel topology, the injected charge of a stimulation pulse is controlled even when electrode impedance changes. The presented system uses spatio-temporal stimulation to share the stimulator circuit among multiple output channels. Another contribution of this work is the implementation of an active charge balancing method. This method monitors the residual voltage at the electrode-tissue interface in between UHF pulses and stops stimulation when this voltage is brought back close to zero. The charge balancing circuit consists of a single comparator connected to the stimulation path. Overall, the proposed stimulator circuit consists of two comparators, one capacitor, three logic gates, and switches. The circuit is easily scalable depending on the stimulation parameters, requiring only two switches per output electrode.

For validation purposes, the circuit has been implemented on a printed circuit board (PCB). The PCB has 8 output pins and operates up to 15V. Using a linear model of the electrode tissue interface, charge injection accuracy of the circuit was measured. The charge injected during a single UHF pulse is scalable with C*V. The implemented PCB uses a capacitor value of C=400 pF, while the voltage V is scaled from 62.5 mV to 1.25 V such that the stimulation intensity ranges from 25 pC to 500 pC per UHF pulse. Furthermore, the charge balancing method was verified with the linear tissue model. The proposed method successfully reduced the residual voltage to 3.1 mV, well within the safety limit of 50 mV. Measurements on a micro-electrode array confirmed functionality of the circuit for non-linear loads. Finally, the work presents an important insight regarding the development of power efficient neurostimulators. It has been shown that it is important to consider not only power efficiency of the circuit but also the energy efficiency of the stimulation waveform to decrease the power consumption of the system.

Acknowledgements

The completion of this thesis brings my time as a student in Delft to an end. I could not have finished the project all on my own and I am very thankful for everyone who has helped me to reach this point.
First of all, I want to thank Wouter and Tiago for supervising the project. Thank you for your guidance, the many discussions we have had and the trust in my competence.
To everyone in the Bioelectronics group: I have enjoyed every moment being part of this group. The brainstorms, activities and coffee breaks have helped me a lot to get through graduation life. Thank you Ali for the technical support and Ger for helping me with difficulties in the PCB design.
I would like to thank Pieter, Bing and Xing from the vision and cognition lab of the Netherlands Institute for Neuroscience for the internship opportunity prior to this project. It was a good learning experience that has helped me to understand the physiological side of the project. Also, I want to thank Bing for lending me the electrode array for my measurements.
Of course, I have to thank all of my friends for the great moments we have shared in the past years. A special thank you to Demi for her unconditional patience and support. And last but not least, thank you to mom, dad and Núria for believing in me and making me the person I am today.

Francesc Varkevisser
Delft, November 2020

Contents

List of Figures

List of Tables

1 Introduction

Throughout the world people are affected by neurological disorders, such as hearing loss, visual impairment or Parkinson's disease. To improve the quality of life of these patients, neural prostheses are commonly used. Neural prostheses are devices that can restore neuronal functions that have been damaged due to accidents or diseases. Examples of neural prostheses that have been used over the last years are cochlear implants for deaf patients, cardiac pacemakers to treat heart arrhythmia's or deep brain stimulators for patients with Parkinson's disease. For patients with visual impairment, a visual prosthesis could restore some sense of vision [1, 2]. Despite several decades of research into visual prostheses, available devices on the market are still very limited. The resolution of the artificial vision is low, reducing usability for everyday tasks [3]. To improve the resolution of visual prostheses, different research groups are developing a prosthesis that stimulates directly to the brain. In this thesis, the design of a multi-channel neurostimulator is presented with the aim to increase the number of available stimulation sites, which is necessary to increase the spatial resolution of said device.

1.1. Background

1.1.1. Visual Prostheses

In order to understand how visual prostheses could restore vision in blind patients, it is necessary to understand the functioning of the visual pathway.

Visual Pathway

The human visual pathway is illustrated in Fig. 1.1. Light enters the nervous system via the retina in the back of the eye. In the retina, incoming photons are converted into electrical signals by light sensitive

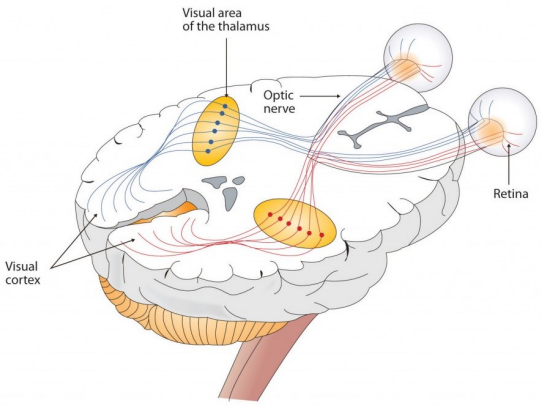

Figure 1.1: Illustration of the human visual pathway from retina to the visual cortex. Figure taken from [4]

photoreceptor cells. Through ganglion cells, electrical signals containing visual information are sent to the optic nerve. The optic nerve is a bundle of nerve cell axons that transports the information from the retina to the lateral geniculate nucleus (LGN), which is part of the thalamus. The LGN performs multiple functions, including spatial as well as temporal correlations of the incoming signals. The processed information is then sent to the visual cortex. The visual cortex is the part of the cerebral cortex that is involved with visual perception and cognition. It is divided into five areas (V1-V5) and going from V1 to V5, the information becomes more abstract [2]. The first three areas are illustrated in Fig. 1.2a. Horizontally the cerebral cortex is divided into six layers (with sub layers) based on cell type and their function [5]. The layers are depicted in Fig. 1.2b, where layer 1 is most dorsal and layer 6 is most ventral. Information from the LGN enters the brain at layer 4c of the primary visual cortex (V1) [5]. The size of V1 differs from patient to patient, it is reported that a surface area in the order of 40 cm^2 can be expected [6]

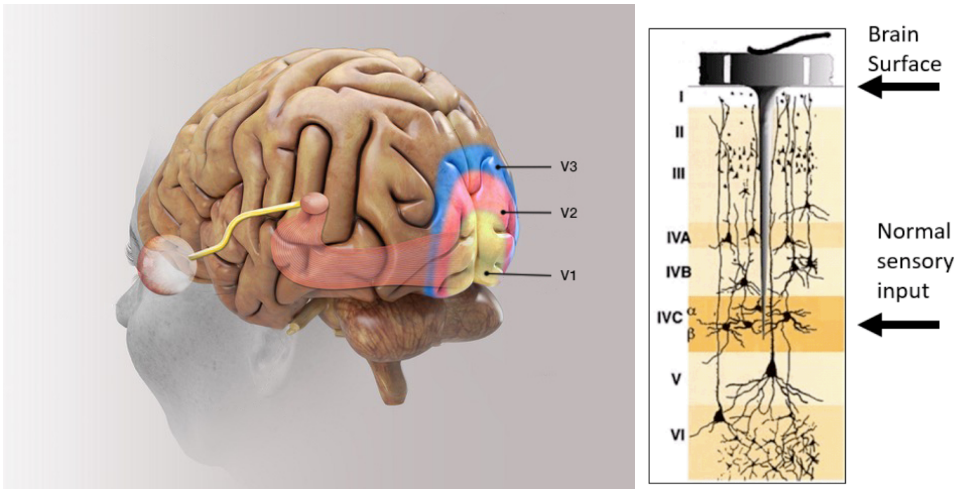

(a) (b)

Figure 1.2: Organization of the visual cortex. (a) The visual areas V1, V2 and V3 are indicated in yellow, red and blue respectively. (b) Division of the cortex in horizontal layers 1-6, visual sensory input enters V1 at layer 4c. Figures adapted from [7] and [5]

Restoring Vision

Damage to any part of the visual pathway could cause blindness or severe vision impairment. Loss of vision can severely complicate participation in society and thus sophisticated devices to restore some degree of vision are being developed [2]. A functional visual prosthesis has to perform three main functions: capture the patients visual environment, process the visual information and transfer the information to the patient [2]. The first function would typically be implemented using a camera that is being carried by the patient, for example on a pair of glasses. Second, processing of the visual information is done in a video processing unit (VPU), usually outside the body. The VPU can implement many functions highly dependent on the implementation of the prosthesis. It could perform functions like edge detection or face recognition [8]. Moreover, the VPU adapts the information in such a way that it can be transferred to the patient by the last part of the system. The last part of the system can be implemented in many ways. One way is through electrical stimulation. Several locations along the visual pathway as target for electrical visual stimulation are suggested in literature: the retina, optic nerve, LGN or primary layers of the visual cortex (see Figure 1.3) [9]. In some other approaches the visual information is converted into other sensory information, for example auditory [10] or tactile [11] information, that can be sensed by blind patients. An implantable neurostimulator can be used for electrical stimulation of the visual pathway. The stimulator transfers visual information from the VPU to the visual pathway with electrical signals through electrodes.

This thesis aims for the stimulation of the visual cortex, which has several advantages over other implementations. First of all, the visual cortex has more space available to implant large numbers of electrodes than the other locations [9]. Moreover, this approach can treat blindness caused anywhere along the visual pathway because the last stage is being stimulated. Other approaches are limited in the causes of blindness that can be treated. For example, diseases beyond the retina such as glaucoma

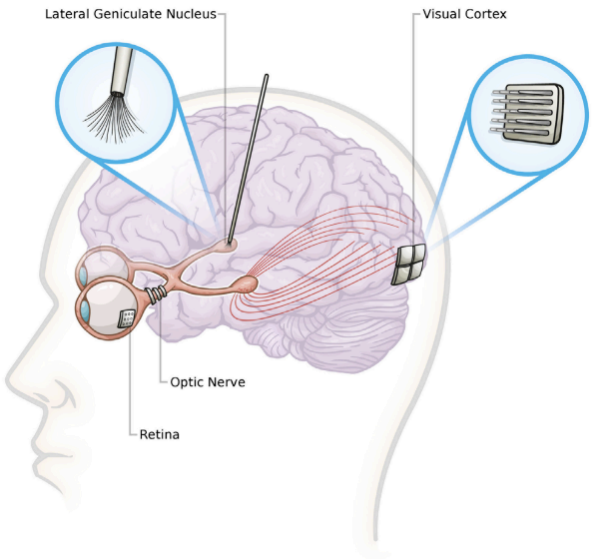

Figure 1.3: Common approaches of visual electrical stimulation. Figure taken from [9]

can not be treated using a retinal implant [12]. Last, the implantation procedure of cortical electrodes is more straightforward than for electrodes at the retina or LGN [9].

Cortical stimulation: intracortical vs surface stimulation
In the cortical approach, neurons located in the primary visual cortex are stimulated in order to create small light dots, called phosphenes, in the visual field [13]. The evoked phosphenes can be mapped onto a map of the visual field [12]. The combination of multiple phosphenes could create an artificial pixelized vision [14]. Layer 4c of V1 is the target area for cortical visual prostheses, as it is the first cortical stage of visual information in which abstraction of the signals is still low [2]. In order to electrically stimulate neurons in layer 4c, generally two approaches are considered: cortical surface stimulation and intracortical stimulation. In cortical surface stimulation, planar electrodes are placed along the surface of the visual cortex, whereas for intracortical stimulation, electrodes are at the tip of penetrating needles, such that they are located at the 4th cortical layer approximately 1.5 mm into the cortex [15]. Both approaches are illustrated in Fig. 1.4.

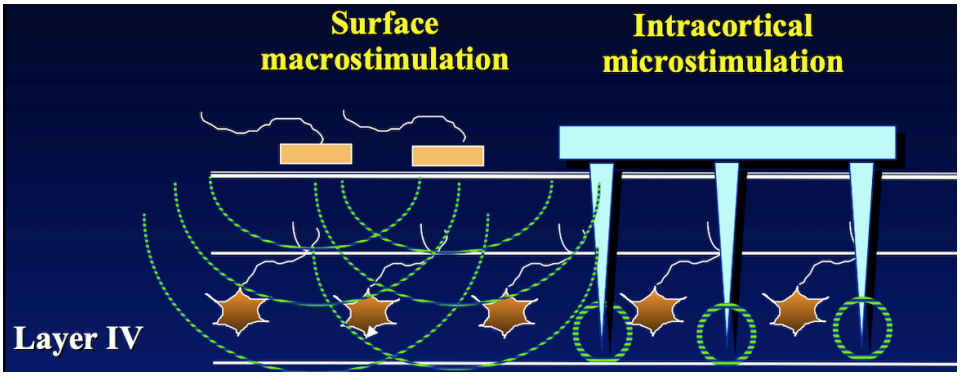

Figure 1.4: Illustration of (left) cortical surface stimulation and (right) intracortical stimulation.

An advantage of surface electrodes is that their implantation will lead to less damage to brain tissue. However, a major disadvantage is that stimulation amplitudes needed to reach neurons in layer 4 are three orders of magnitude higher than for penetrating electrodes [2], which might evoke multiple phosphenes for one electrode, cause cross-talk between electrodes or lead to epileptic seizures [16]. Therefore, penetrating electrodes are preferred for this application [15].

Intracortical Stimulation Challenges

Stimulation of the visual cortex using intracortical electrodes imposes a few big challenges to the design of the implantable stimulator.

First of all, the resolution of the artificial vision depends on the number of stimulation channels. As will be explained later, a stimulation channel can be created using one or more electrodes. Each active channel should be able to elicit one phosphene; thus increasing the number of stimulation channels increases the number of pixels in the artificial vision [17]. Although literature suggests that 625 pixels are enough to provide functional vision to perform everyday tasks [18], it is expected that future visual prostheses will have more than 1000 channels.

Furthermore, the power consumption of stimulating a high number of channels for multiple hours per day omits the possibility of a battery-powered stimulator as the battery would be too big to be implanted inside the skull. Therefore, some form of wireless power transfer to the implanted device will be required. The transfer of sufficient power is a technological challenge behind the scope of this project, but it could be a limitation to the number of channels that can be stimulated simultaneously.

Last, the level of excitation required to evoke a phosphene is, among other things, dependent on the electrode impedance and placement of the electrode [19]. This does not only differ between channels, but also over time [19]. Therefore, the intensity of each channel should be controllable separately.

1.1.2. Electrical Neuromodulation

In the previous section, the case for a visual prostheses has been introduced. There it was explained that electrical signals applied to electrodes could evoke phosphenes. In order to evoke phosphenes, neurons need to be activated. The electrochemical (a combination of both electrical and chemical signals) nature of our nervous system makes the activation of cells by means of electrical signals possible.

Nerve cells are enclosed by a membrane. This membrane contains ion-channel proteins that facilitate the flow of ions (a.o. potassium and sodium) in and out of the cell. The presence of different concentrations of ions on both sides of the cell membrane causes a potential difference across the membrane, called the membrane voltage V_m. The ion-specific permeability of the cell membrane is dependent on V_m. At rest, V_m is kept around $-70\,\text{mV}$ [20]. If the membrane voltage is changed to a certain threshold, an action-potential is initiated. The action-potential is an all-or-nothing reaction during which the flow of ions through the membrane increases immensely for a short period. An action-potential travels along the axis of the nerve cell, the axon. At the end of the axon, the arrival of an action-potential can lead to the release of neurotransmitters into the synapse, which is a gap between the axon terminals of the transmitting neuron and the dendrites of the receiving neuron. Neurotransmitters are chemicals used to activate or inhibit the receiving (post-synaptic) nerve cell [4]. In case of cell activation, an action-potential will be created in the post-synaptic nerve that leads to signalling to other neurons. Thus, the cells use chemical recipients to cause electrical signals. The signalling between neurons is illustrated in Fig. 1.5.

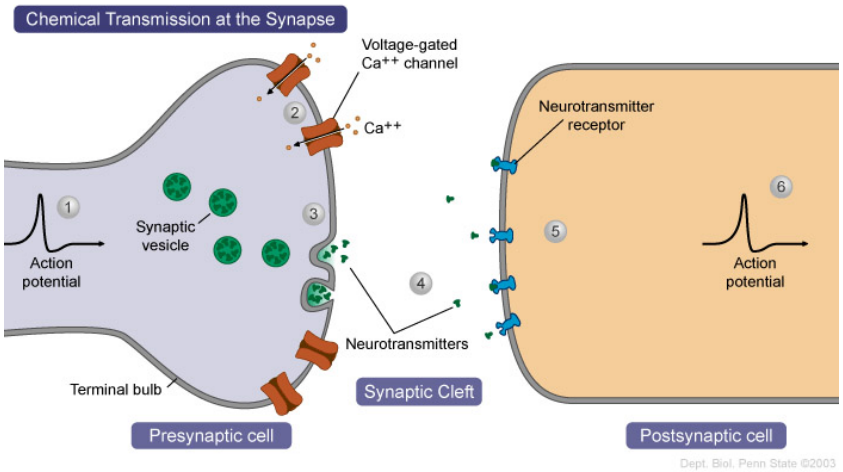

Figure 1.5: Signalling between neurons at the synaptic cleft using neurotransmitters [21].

Since sodium and potassium ion-channel proteins are voltage-gated, the membrane voltage of a cell can be modulated by applying external electrical stimuli. One way of doing so is by sending electrical pulses to polarizable electrodes in the proximity of said cells. Polarization of the electrodes leads to an electric field. The electric field exerts a force on ions, causing charge redistribution in the tissue. The charge redistribution leads to a change in V_m, which can activate or inhibit nerve cells. The mechanisms of charge transfer during stimulation are highly non-linear; However, the linearized electrode-tissue interface (ETI) model depicted in Fig. 1.6 can be used as a first-order approximation of the charge transfer [22]. This model consists of three components: tissue resistance R_{tis}, a double layer capacitor C_{dl}, modeling the capacitive electrode/electrolyte interface and $Z_{faradaic}$, modeling faradaic charge transfer from the electrode to the tissue through redox reactions. Faradaic charge transfer through $Z_{faradaic}$ is non-reversible and could lead to tissue or electrode damage [22], thus should be kept minimal for safe stimulation.

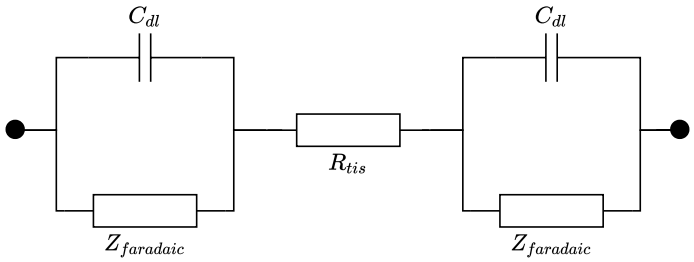

Figure 1.6: Electrical model of the electrode-tissue interface in a two-electrode configuration. The two contact points are the electrode contacts to the circuit, R_{tis} represents the resisitve tissue impedance, C_{dl} the capacitive electrode/electrolyte interface and $Z_{faradaic}$ models faradaic charge transfer from the electrodes to the tissue through redox reactions.

Whether a stimulation pulse leads to the activation of a cell depends on both the strength and duration of the pulse. This dependence is illustrated with the *strength-duration* and *charge-duration* curves (Fig. 1.7) [20]. The rheobase current (I_{rh}) is the minimum stimulation intensity which theoretically, with an infinite long pulse, could lead to an action potential. The chronaxie time (t_c) is the pulse width required for activation at an intensity of $2I_{rh}$. Both curves can be obtained experimentally and are dependent on tissue properties such as the thickness of the cell membrane [20].

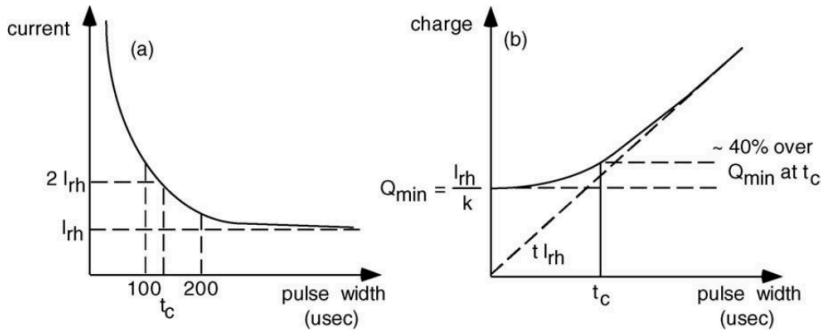

Figure 1.7: Example plots of (a) the *strength-duration* curve and (b) *charge-duration* curve. The rheobase current (I_{rh}) is the minimal current needed to reach an action potential [22].

There are two conventional methods of electrical stimulation used to apply pulses to the tissue: Current mode stimulation (CMS) and voltage mode stimulation (VMS). Other types of stimulation, such as charge mode stimulation, do exist but will not be covered here. Stimulation pulses are typically biphasic, consisting of two consecutive phases with opposite polarity. During the first phase, or activation phase, an electric field is applied in order to initiate an action potential. The second phase, the reversal phase, is used to reverse the accumulated charges at the ETI. A short delay between the two phases, an interphase delay, can be introduced to enhance the efficacy of the stimulation [23]. Monophasic pulses could also be used, but for repetitive stimulation pulses this would lead to a voltage built up over the ETI that could harm the tissue and electrodes [22].

In VMS and CMS, a square biphasic voltage or current pulse is applied to the electrodes. The transient waveforms of both stimulation methods are depicted in Fig. 1.8. In CMS, the slope of voltage increases as the current is kept constant. The slope of the voltage is caused by charge accumulation at the double layer capacitance C_{dl}. Similarly, the voltage is constant in VMS, while the stimulation current decreases. For cell activation it is important to control the amount of charge applied during the pulse. In CMS, the total amount of charge injected during the first phase is equal to $I_{stim}t_{phase}$ and thus independent of the tissue impedance. In VMS, the amount of injected charge is dependent on the non-linear ETI impedance. The control over the injected charge makes CMS a favoured method for most applications [24].

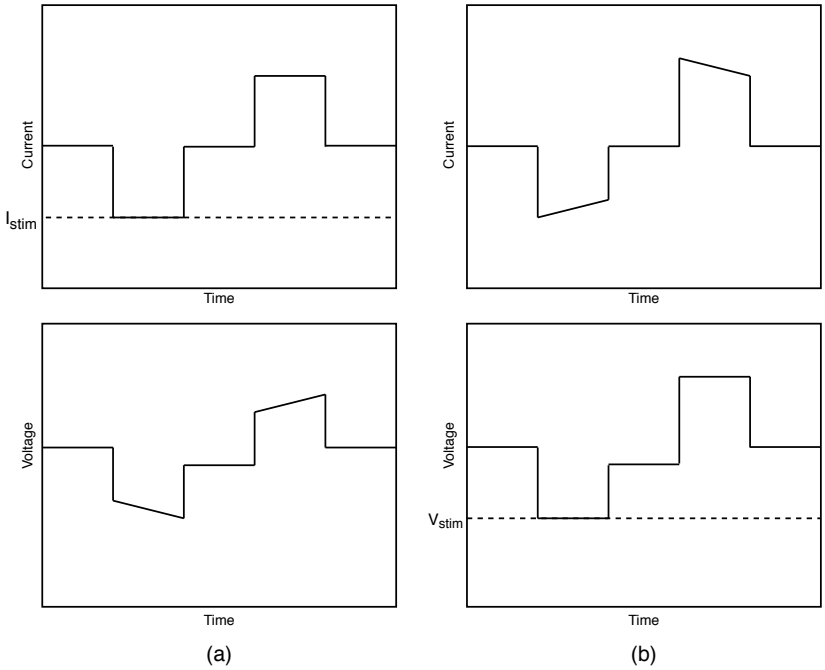

Figure 1.8: Current and voltage transients during (a) CMS and (b) VMS.

Accurate control of charge in CMS comes at the cost of power efficiency. Here, efficiency of the stimulator is considered to be $\eta = \frac{P_{tissue}}{P_{supply}}$. In VMS power is transferred from the supply directly into the tissue, while in CMS the current source dissipates power as well, degrading power efficiency [24]. The power dissipated by the tissue and current source during a CMS pulse with a constant supply voltage is depicted in Fig. 1.9. Especially in multi-channel systems where tissue impedance and required intensity are different from channel to channel this leads to inefficient stimulation [25]. In that case the voltage source has to accommodate the worst case channel and consequently the power efficiency of all other channels is affected.

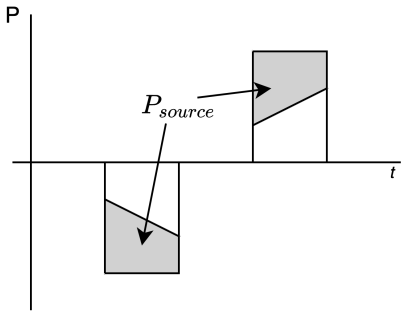

Figure 1.9: Power dissipation in the current source during current mode stimulation (grey area) causes inherent inefficiency of this method [26].

Although VMS does not suffer from power conversion losses, the lack of charge control can lead to unsafe situations for both the tissue and electrodes. To ensure safe stimulation, too much charge accumulation at the capacitive electrode/electrolyte interface should be avoided because the presence of non-reversible reactions through $Z_{faradaic}$ increases with depolarization of the electrodes [22]. An important limit for the voltage over C_{dl} is the water window. This threshold is the voltage at which oxidation and reduction of water through electrolysis occurs. If the water window is exceeded, the charge transfer will primarily consist of non-reversible oxidation reactions damaging both the electrodes and the tissue [22]. It is important to notice that for much lower voltages, non-reversible reactions already occur. Therefore, a voltage much lower than the water window is often considered as a safety window for the electrode voltage. Furthermore, due to the presence of non-reversible faradaic reactions, even a perfectly matched biphasic pulse will lead to a residual voltage at the tissue interface. This is illustrated in Fig. 1.10, where a perfectly matched biphasic current pulse is applied to an ETI model with and without considering the faradaic impedance. For repetitive stimulation pulses, residual charge can build up to the point where the safety threshold is exceeded. Consequently, charge balancing methods are required to prevent charge build up in order to keep the residual voltage in between safety limits.

In conclusion, charge control is very important for both stimulation efficacy and safety. VMS has good power efficiency, but should be used with care because of the lack of charge control. CMS on the other hand has good charge control but generally has lower power efficiency. Even with precise charge control of CMS, charge balancing techniques are important to ensure long term safety of stimulation.

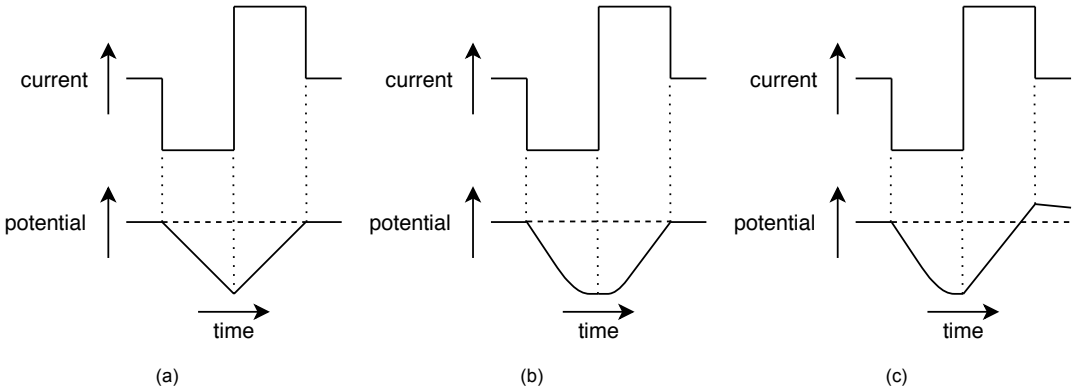

Figure 1.10: Potential waveform on the capacitive double layer during a CMS pulse for different charge-transfer mechanisms; (a) Transient during capacitive charge transfer. (b) Transient for reversible faradaic reactions. (c) Non-reversible faradaic reactions cause charge imbalance after a perfectly charge-balanced current waveform. Figures reproduced and adapted from [22].

1.2. Problem Statement & Research Questions

Intracortical visual prostheses are under development in order to treat patients with severe loss of vision. For the development of such devices an implantable neurostimulator capable of stimulating 1000 or more channels is needed. When stimulating this many channels in a wireless powered system, it is crucial to minimize power consumption of stimulation [27]. The duration and charge of a stimulation pulse need to be controlled precisely with high power efficiency of the stimulation source for effective, safe and efficient neurostimulation. Conventional stimulation methods have disadvantages for multi-channel stimulators: Current mode stimulation has low power efficiency in multichannel configuration and the charge injected in voltage mode stimulation is dependent of channel impedance. In the application of intracortical visual stimulation, channel impedance varies both in location and over time. Even with accurate charge control, repetitive stimulation can lead to unsafe situations. Therefore, a charge balancing scheme should be used to ensure minimal residual voltage at the electrode tissue interface.

Considering all the above, the main research question of this thesis is defined as follows:

> How can stimulation pulses be delivered to multiple intracortical microelectrodes in a safe and efficient manner to effectively evoke phosphenes?

1.3. Report Outline

The rest of this report is organized as follows; First, a literature review on intracortical visual stimulation and state-of-the art multi-channel stimulation is presented in Chapter 2. Then, both system and circuit level design of the proposed system along with a proof of concept printed circuit board (PCB) implementation are discussed in Chapter 3. Following that, the system is validated using simulations and measurements on the PCB in Chapter 4. Last of all, Chapter 5 contains a discussion and conclusion of the presented work with recommendations for future work.

2

Literature Review

In order to find an answer to the research question, existing literature is presented in this chapter. The chapter is divided into three parts. First, the main components of implantable neurostimulators together with important design considerations will be covered. Second, the physiological properties of intracortical visual stimulation are described. This includes stimulation parameters necessary to effectively evoke phosphenes and the effect of parameter scaling to the physiological response. Furthermore, electrical properties of intracortical micro-electrodes are described. The third part of this review consists of a state-of-the-art analysis on stimulator implementations that focus on power efficiency and charge controllability. At the end of this chapter, the thesis objectives and approach are stated.

2.1. Implantable Neurostimulator Design

2.1.1. System Components

The goal of an implantable electrical neurostimulator is to deliver stimulation pulses to tissue. Although different applications require different stimulation parameters and system requirements, some essential circuit components found in all stimulators can be distinguished. These components include telemetry, power management, control circuits and stimulator sources. A system level block diagram of a generic implantable neurostimulator is depicted in Fig. 2.1.

First of all, the device needs a transceiver for communication with the device from outside the body. This can be used to transfer stimulation parameters to the device and to get measured data or system status from the device. Next to data transfer, implantable stimulators commonly require a power link to transfer power to the device. If the device is powered from a non-rechargeable battery only, it should be big for longevity of the device. For devices implanted in the torso, a non-rechargeable battery can

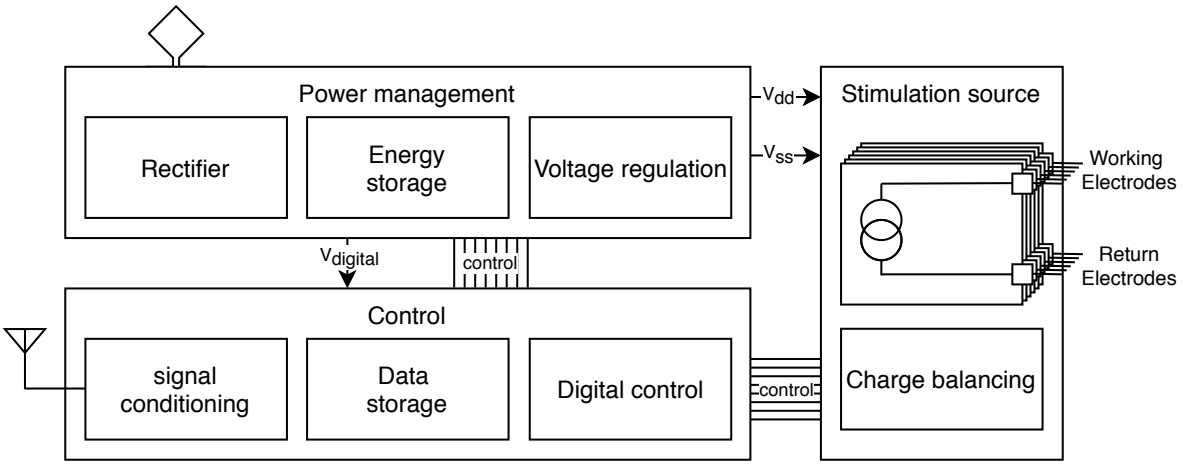

Figure 2.1: System level block diagram incorporating the typical system components of an implantable neurostimulator.

sometimes be used as there is available space to implement the device. However, when designing stimulators for the brain, total dimensions of the implant are critical as there is little space between the brain and the skull. The battery for these devices should be small and rechargeable and thus a power link is needed to recharge the battery.

In the power management block, incoming power is regulated for correct operation of the system. Circuits in this block regulate voltages for the rest of the system and manage the system's battery. Often the incoming AC signal from the wireless power delivery is rectified and regulated to the appropriate voltage levels for the rest of the system. Some recent stimulator designs try to omit power conversion losses in this part of the system by stimulating tissue directly with the incoming power signal [28].

A control block is used to manage correct operation of all other system components. Control signals received by the wireless data link are decoded to system commands. This could include stimulation commands or configuration of the stimulation channels. Stimulation parameters for each channel can either be stored in a memory block or be included in the control signals over the wireless link [17]. An advantage of storing stimulation parameters on chip is that stimulation commands become shorter and thus less data has to be sent over the wireless link. Specifically in systems with a high number of stimulation channels or high stimulation rates, the data link can be a bottleneck to the stimulation patterns. For such systems, on-chip memory would be beneficial. When the data link is not a limiting factor for the system, sending stimulation parameters with each stimulation command adds flexibility to the device. Flexibility of the stimulation parameters is often required for research purposes [17].

The last essential block of the implant is the stimulation source. The stimulation source is used to drive electrodes and deliver stimulation pulses to the tissue. Important considerations in the design of the stimulation source are the mode of stimulation, efficacy and safety of the stimulation signal, and power efficiency. In Chapter 1 some design trade-offs between efficiency, safety and charge control were already introduced. Options of dealing with the aforementioned trade-offs will be discussed in Section 2.3.

2.1.2. Electrode Configuration

For electrical neurostimulation at least two electrodes are needed. Potential difference between the electrodes creates an electric field that can lead to cell activation. One electrode, the working electrode, is driven either positive (anode) or negative (cathode). The other electrode(s) is used as return path for the current and is called the return electrode. Cell activation occurs due to tissue depolarization near the cathode [22]. To create biphasic pulses, the stimulator should put current through the load in opposite directions. This can be achieved with different electrode configurations as illustrated in Fig. 2.2. In monopolar stimulation (Fig. 2.2a), one electrode is driven negative and positive with respect to a distant reference electrode to create a biphasic pulse. This configuration requires two stimulator output drivers coming from a positive and negative supply voltage. Monopolar stimulation has the advantage that the same return electrode can be used for multiple stimulation channels. The area of the return electrode is much bigger than the working electrode, resulting in negligible charge accumulation on the return electrode. Monopolar stimulation causes a point-source electric field around the working electrode. For bipolar stimulation, the stimulator drives two adjacent electrodes. The electric field of an electric dipole is created between the two stimulation electrodes. As can be seen in Fig. 2.2b, a biphasic pulse can be created from a single supply by interchanging the relative position of the electrodes in the circuit. Single supply stimulator design is beneficial for power consumption [29]. When a dual supply is used, bipolar stimulation doubles the voltage compliance with respect to a monopolar configuration. Similar to bipolar stimulation, multiple electrodes can be used as cumulative return electrode. Multipolar electrode configuration allows for current steering techniques. Current steering minimizes cross-talk during multichannel operation [30]. Also, the power supply of each channel can be isolated to further reduce cross-talk [31]. For multichannel applications, a bipolar or multipolar configuration is often preferred because of the current steering possibilities [32].

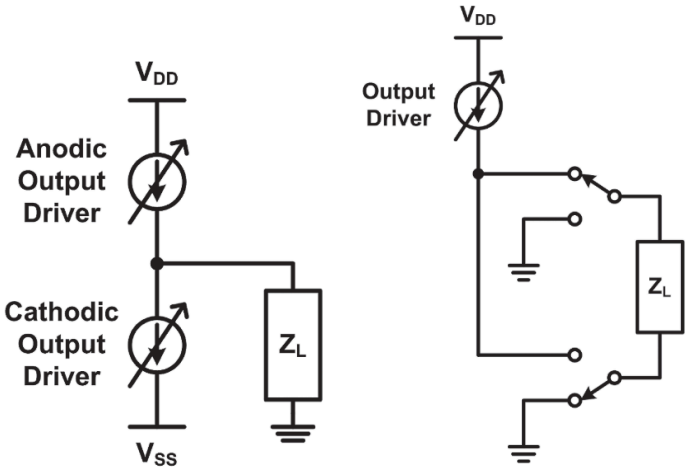

Figure 2.2: Two possible electrode configurations to create biphasic stimulation pulses. (a) Monopolar electrode configuration, using two separate output drivers with opposite polarity to the same electrode. (b) Bipolar electrode configuration, using a single output driver to opposite electrodes for biphasic pulses. Figures taken from [32].

2.1.3. System Level Architecture

The integration of all blocks into a complete system and the way they are connected can be done in a few different ways. Depending on the application a choice for the best architecture can be made. In [17], four possible system level architectures are distinguished; monolithic, remote, modular and distributed. An illustration of each architecture is depicted in Fig. 2.3.

In the monolithic approach all system components are integrated into one chip. In this approach, the site of stimulation determines the location of the stimulator chip. For efficient and reliable power and data transfer, proximity and correct alignment of the chip and the outside transceivers is important. Therefore, this architecture is not appropriate for applications where tissue deep into the body needs to be stimulated. Furthermore, the size of the chip is determined by the area that needs to be covered by the electrodes. This makes this architecture suitable only for applications with relatively small stimulation areas. An advantage of this approach is that there is no need for interconnection between different system parts. Interconnection between different parts is often a source for unreliability and packaging issues [33].

Second, the remote approach separates the site of stimulation and the stimulator circuitry. The stimulation electrodes are connected to the stimulator using leads. This approach is advantageous because the stimulator can be placed on a location where there is enough space and proper alignment of wireless transceivers is possible while electrodes can be placed close to target cells. This approach is used for example in cardiac pacemakers or deep brain stimulators. When the number of stimulation channels is high, this approach can lead to interconnection problems at the chip as each electrode is connected separately to the chip [33].

The system is divided into multiple connected integrated circuits (ICs) in the modular approach. One chip containing telemetry, power management and control circuits is placed at a convenient location for power and data transfer. This chip is connected to multiple stimulation modules containing stimulation sources and interconnection to the electrodes. This architecture is proposed in both intracortical visual stimulator designs presented in [34] and [17]. Again, the central module can be placed close to the outside transceiver for efficient power and data transfer. Power recovery is also done on the central module together with general control. The required voltage levels and control signals are sent to each stimulation module. Each stimulation module can contain multiple stimulation sources and some local control logic. Using this architecture it is possible to cover a large area with electrodes while a single central module is used for communication and power transfer.

The distributed architecture is similar to the modular approach, but the stimulation modules are no longer connected to a central module. Each module has its own telemetry, power recovery and data control circuits. This approach gets rid of wires used to connect the modules in the modular approach. These wires can be a source for system failure and take up a lot of space when many stimulation

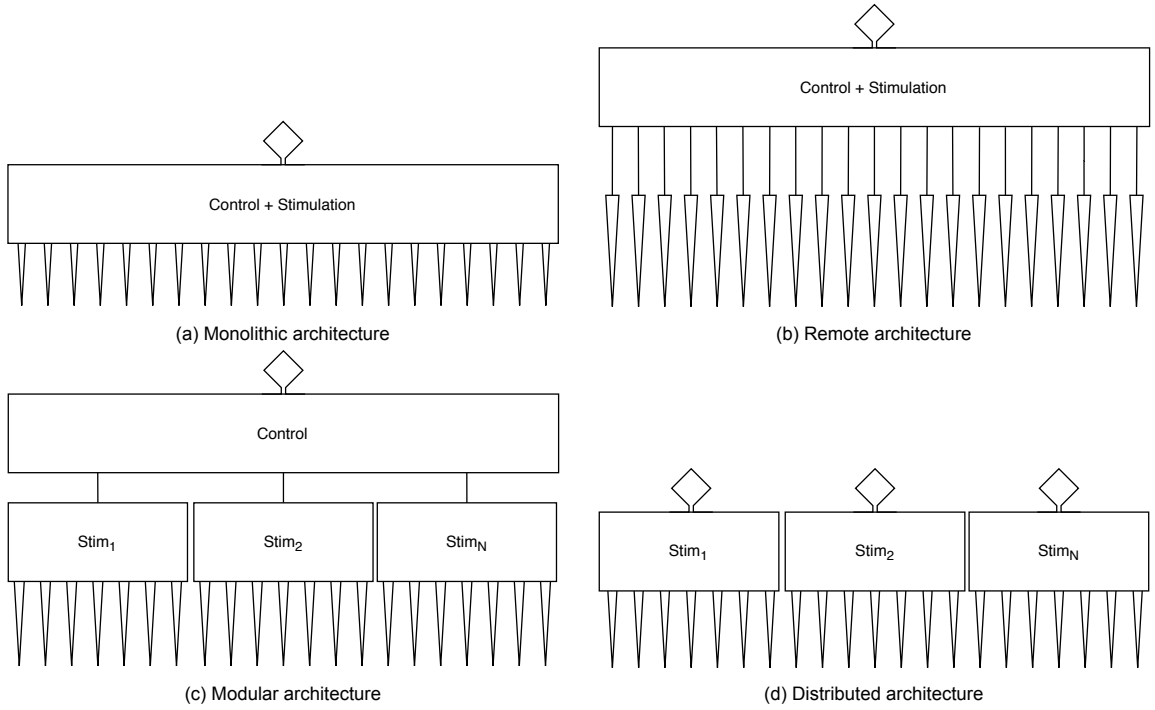

Figure 2.3: Different system level architectures distinguished in [17].

modules are connected to a single central module [35]. A disadvantage of the distributed architecture is that all modules need to be addressed separately from outside the body. Proper transceiver alignment with each individual module can be impractical. Also, the telemetry and power recovery circuits will increase the size of each module.

2.2. Intracortical Visual Stimulation

Although there is no commercially available intracortical visual stimulator yet, numerous studies have investigated the possibility of such devices in clinical trials. As such, these studies have developed a large body of knowledge about important stimulation parameters for effectively evoking phosphenes. Also, microelectrodes for intracortical stimulation have been developed and accepted for clinical studies. Electrical properties of these electrodes indicate output requirements for the implantable stimulator.

2.2.1. Phosphene Generation

Repetitive biphasic current pulses are commonly used to stimulate the visual cortex. The amount of current necessary to evoke a phosphene is called the phosphene threshold [12]. The effect of varying waveform parameters on phosphene thresholds have been researched extensively [12, 13, 36]. Not only waveform parameters, but also electrode placement, size and material influence phosphene thresholds. The waveform parameters of a biphasic square pulse are illustrated in Fig. 2.4. First of all, the polarity of the pulse is indicated by the polarity of the first phase. This can either be anodic first (AF) or cathodic first (CF). In an anodic phase, the potential at the electrode is driven positive with respect to a reference electrode, while during a cathodic phase the electrode-potential is driven negative. In a biphasic pulse, the second phase will have the opposite polarity with respect to the first phase. Second, the phase duration of both phases is indicated with t_{ph1} and t_{ph2} respectively. The phase duration of both phases does not have to be equal. As mentioned earlier, an interphase delay is often applied to improve the efficacy of the stimulation. The interphase delay is indicated with t_{iph}. For effective stimulation, a burst of pulses or pulse train is being applied to each channel. The pulses in the burst are applied at a frequency of f_{rep} $\left(=\frac{1}{t_{rep}}\right)$. As can be observed in Fig. 2.4, the interpulse delay t_{ip} can be derived as t_{rep}-t_{ph2}-t_{iph}-t_{ph1}. Last, the amplitude of the pulse is indicated with I_{stim} or V_{stim}. In CMS, the amplitude and phase duration are commonly selected in a way that the applied charge in

both phases is equal, e.g. (2.1) holds.

$$I_{stim,1}t_{ph,1} = I_{stim,2}t_{ph,2} \tag{2.1}$$

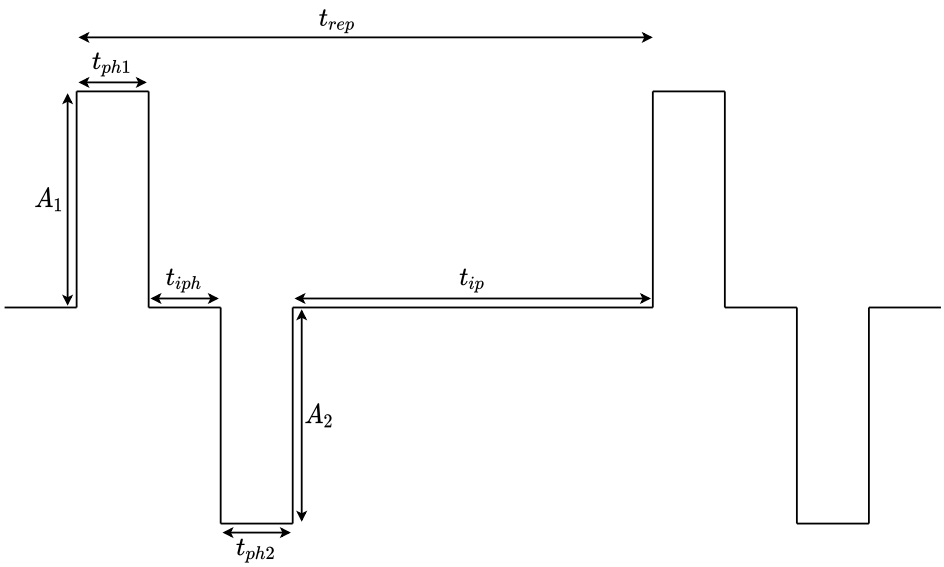

Figure 2.4: Illustration of the variable stimulation parameters of a biphasic waveform.

Inconsistency in stimulation parameters and electrodes as well as differences between patients makes comparison of reported phosphene thresholds difficult. Nevertheless, some conclusions can be drawn from studies relating phosphene thresholds to variations in stimulation parameters. First of all, phosphene thresholds are systematically lower for CF stimulation than for AF stimulation [13]. Stimulation frequencies between 100 Hz to 200 Hz are most effective for visual stimulation [12]. For frequencies below 150 Hz, a decrease in frequency results in a higher phosphene threshold, while for frequencies above 150 Hz the threshold is not affected by frequency change [13]. Second, a phase duration ranging from 10 µs to 1000 µs has been shown to be effective [12], with a decreasing threshold for increasing pulse duration. However, usually a phase duration around 200 µs is being used for visual stimulation [13, 37–39]. Last, an increase in train length causes a decrease in phosphene thresholds [12, 13]. Typically, a train duration of 125 ms to 300 ms is used [13, 37–39]. As can be seen, a wide spread of waveform parameters are being used for visual stimulation. Although thresholds as low as 5 nC (25 µA for 200 µs) have been reported in [13], currents up to 100 µA are being used in physiological studies [34, 37]. This diversity of waveform parameters requires flexibility in the stimulator in order to facilitate clinical trials [17]. A list of typical waveform parameters can be found in Table 2.1. These parameters will be used to establish the system requirements of the stimulator later on.

Table 2.1: List of typical waveform parameters used in cortical visual stimulation studies.

Parameter	Typical value
Polarity	CF
f_{rep}	200 Hz
t_{ph}	200 µs
I_{stim}	1 µA–100 µA
Train duration	125 ms–300 ms

2.2.2. Intracortical Microelectrodes

Next to the waveform parameters, the system requirements depend on the type of electrodes that need to be driven with the device. Complications with surface electrodes motivated the development of an

array of penetrating electrodes for intracortical stimulation, the Utah Electrode Array (UEA) [40]. The geometry of the UEA allows the electrodes to be penetrated into the cortex, close to the target neurons. By doing so, the current threshold for evoking phosphenes is decreased enormously [40]. This decrease in amplitude also allows the electrodes to be placed closer to each other, thereby increasing the stimulation resolution [41]. A consequence of miniaturizing electrodes is the increase in their impedance. For intracortical micro-electrodes, impedances ranging from 50 kΩ up to a few hundred kΩ can be expected [19, 42–44], while the impedance of surface electrodes is typically around 10 kΩ. Although the injected charge should be independent of the electrode impedance, the required supply voltage is dependent on the impedance. The linearized model of the ETI depicted in Fig. 1.6 will be used during the design phase of the system and initial testing. Based on impedance measurements presented in [19, 43] and electrode characterization presented in [45], the values listed in Table 2.2 will be used to model the electrode tissue interface.

Table 2.2: List of model parameters that will be used to model the electrode tissue interface of intracortical microelectrodes.

Parameter	Value
R_{tis}	50 kΩ–150 kΩ
C_{dl}	10 nF–100 nF
$Z_{faradaic}$	>1 MΩ

The listed model values will be used as a guideline for the system requirements. The impedance characteristics of each channel will depend on many conditions such as electrode placement, variances in the manufacturing process or scar tissue encapsulating the electrode. Also the impedance of implanted electrodes will change over time [37]. Moreover, development of stimulation micro-electrodes could decrease the impedance and increase the capacitance of future electrodes. Therefore, the system will be designed such that the operation is largely independent of the electrode impedance and could simply be modified when the development of new electrodes facilitates lower electrode impedances.

2.3. State-of-the-Art

Several research groups around the world have been developing multi-channel intracortical stimulators [15, 17, 46]. In each of these full system implementations, the stimulator output is implemented with a current mode stimulator. As explained in Chapter 1, this leads to inefficient multichannel stimulation. The power efficiency of current mode stimulation could be improved by minimizing the voltage drop over the current source. On the other hand, the addition of charge control to voltage mode stimulators would make the method both safe and efficient. An overview of state-of-the-art stimulator designs that tackle the disadvantages of both techniques will be presented below. Furthermore, an overview of state-of-the-art charge balancing techniques is given.

2.3.1. Efficiency in Current Mode Stimulation

When current mode stimulation is being used, the stimulators efficiency can be improved by minimizing the power consumption of the current source. The following stimulators are designed for efficient current mode stimulation.

First of all, [25] presents a current mode stimulator that is based on a high frequency unfiltered DC-DC buck-boost converter. An inductor is charged using the supply voltage and discharged over the tissue in a rapid sequence. The output voltage of the DC-DC converter follows the voltage needed for the stimulation signal. In [47], this design is implemented into an 8-channel stimulator by interleaved stimulation which is possible due to the high-frequency property of the waveform. The presented design has a high efficiency compared to current mode stimulators; however, the stimulator requires an off-chip inductor, which compromises area and implantability. Even if the system could be improved in order to stimulate up to one hundred channels with one inductor, a visual prosthesis would still require multiple off-chip inductors. Off-chip components are bulky and will increase the size of the stimulator. Moreover, bond pads connecting the components to the chip are fragile and thus affect the reliability of the system.

Second, [48] uses a technique called dynamic voltage scaling (DVS). A DC-DC converter with

switched capacitor output is used to create four different voltage levels, which can be switched according to the needed voltage at the output. Similarly, the design of [49] uses charge pumps to create a dynamic supply voltage with steps of 0.5 mV. The circuit automatically increases the voltage headroom when the current source is not in saturation.

Last, [50] and [51] present adiabatic stimulator designs. Adiabatic stimulator design is the optimal form of dynamic voltage scaling. The voltage steps are minimized and the output voltage is followed accurately in order to minimize the power consumption of the current source.

The efficiency of current stimulation using dynamic voltage supplies is illustrated in Fig. 2.5. Although the power efficiency of the output stage might improve significantly using DVS, there are some drawbacks in this approach. First, there is a trade-off between power and area. As illustrated in Fig. 2.5, the power efficiency is inversely proportional to the number of steps in the voltage supply. The capacitors used to create voltage steps make the implementation generally bulky. Moreover, the dynamic voltage supply does not solve inefficiency of multichannel current stimulation. Still, the supply voltage has to accommodate the worst case channel impedance, making all other channels inefficient. This could be solved by creating a dynamic supply for each channel separately, although this will cost a lot of area. Last, the implementation of an adiabatic design is only beneficial when the voltage slope at the ETI is significant during the stimulation pulse [26]. Properly designed stimulation electrodes should have a high charge-injection capacity which decreases the voltage slope during stimulation [52]. Therefore, it is to be expected that technological advances in micro-electrode design diminishes the advantages of dynamic voltage supplies.

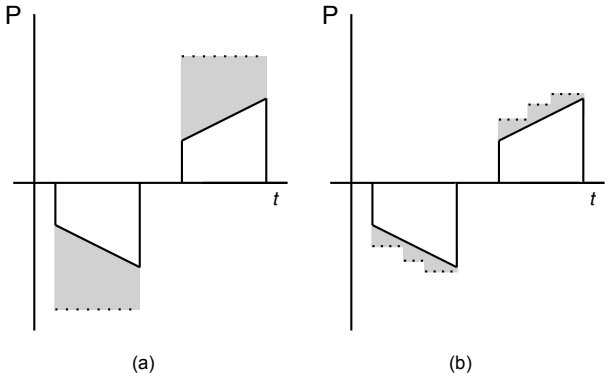

Figure 2.5: Power consumption of the current source in current mode stimulation (grey area) for (a) a constant supply voltage and (b) a stepped supply voltage.

2.3.2. Charge Control in Voltage Mode Stimulation

Voltage mode stimulation is fundamentally more efficient but the stimulation intensity is dependent on the channel impedance. The stimulator designs presented below have implemented ways to control the stimulation intensity for voltage mode stimulation.

A voltage mode stimulator based on the principle of a switching regulator was introduced in [53]. The design aims to limit the voltage built up over the double layer capacitance. Short voltage pulses are applied to the electrode and after each pulse, the voltage at the interface is compared to a reference voltage. In between the pulses, the voltage over C_{dl} can be measured directly across two electrodes since there is no voltage drop across the resistive part of the tissue. When the measured voltage is below the limit, a consecutive pulse is applied. When the limit is exceeded, the stimulation will pause for one time period after which the voltage is measured again. This method results in a stimulation signal depicted in Fig. 2.6. Even though this method ensures that the electrode voltage stays within safe limits, the charge injected during stimulation is not monitored and thus still unknown.

Moreover, voltage mode variants on adiabatic stimulators have been developed. In the CMS adiabatic designs, a current source was used which was kept at the edge of saturation by scaling the driving voltage. In [26], the current source is omitted and the stepped voltage signal is applied directly to the tissue. The resulting stimulation current looks like a rippled constant current waveform as depicted in Fig. 2.7; however, the actual waveform depends heavily on the channel impedance. As a consequence, the resulting injected charge is still unknown. [54] presents an adiabatic design in which the current

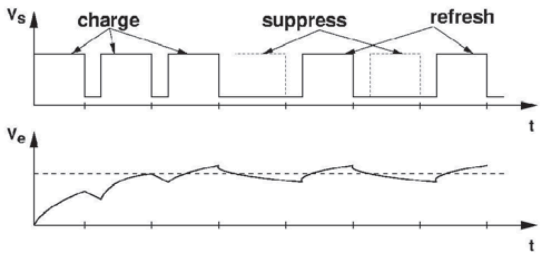

Figure 2.6: Output voltage waveform of the switched-voltage regulator stimulator presented in [53], where V_S is the stimulation voltage and V_e is the voltage on the capacitive double layer.

source is replaced with a current monitor. Based on the measured current, the voltage to the electrode is adapted. This design has an increased power efficiency compared to the CMS variant because there is no voltage drop over the current source anymore. However, disadvantages for multichannel implementation still apply as the system is only efficient for the worst case channel. In order to efficiently stimulate in a multi-channel system, multiple adiabatic sources will be needed which increases chip area.

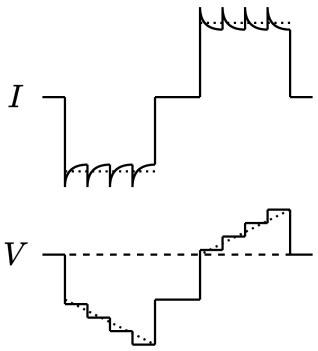

Figure 2.7: Theoretical rippled output current of the stimulator design presented in [26].

Last, an Ultra High Frequency (UHF) Switched Voltage stimulator was introduced in [55]. In switched-mode stimulation, the tissue is being stimulated using high-frequency pulse width modulated voltage waveforms. The pulse width modulation (PWM) allows control over the average output voltage: $V_{avg} = \delta V_{supply}$, where δ is the duty cycle of the signal. A pulse width modulated biphasic pulse is illustrated in Fig. 2.8. PWM is an efficient power conversion method. When the pulse is high, power is transferred from the supply directly into the load. When the pulse is low, there is no current flow and thus the power consumption is zero. Theoretically, this could lead to a power conversion efficiency of 100%. However, modulation of the voltage introduces switching losses which decrease practical conversion efficiencies of this method. In power converters, the output of a PWM DC-DC converter is low-pass filtered to create a constant output voltage. In [56], it has been shown that tissue properties can be used as the output filter for this application. To show this, the axon cable model depicted in Fig. 2.9 was considered. A voltage V_{ext} applied to the electrode placed at distance d_{axon}, results in an attenuated voltage $\mathrm{V}(d_{axon})$ at the cell membrane described by (2.2) [20], where R_s is the tissue resistance and σ the extracellular conductivity. Here, a linear and homogeneous tissue is assumed for simplicity.

$$V(r) = \frac{V_{ext}}{4\pi\sigma R_s r} \tag{2.2}$$

In Fig. 2.10, the resulting membrane voltage for a UHF voltage pulse and a constant current pulse ($V_{ext} = I_{stim}R_s$) with a comparable amplitude are compared [56]. As can be seen, the membrane acts as a low-pass filter and the UHF stimulation is able to depolarize the membrane in a comparable manner as the constant current pulse. Using tissue properties as output filter introduces the advantage that no filtering components are required in the stimulator circuit, resulting in a simple and small design.

The efficacy of switched stimulation has been proven in [56]. However, the long term effects of a pulsed waveform have not yet been investigated and should be considered before implementation in

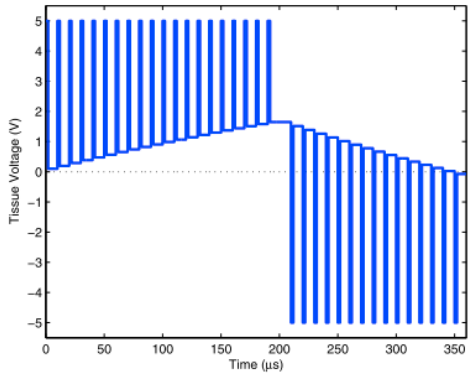

Figure 2.8: PWM modulated voltage mode stimulation waveform.

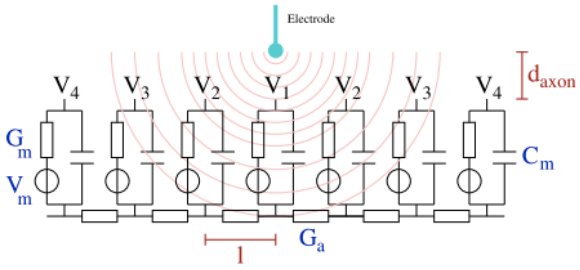

Figure 2.9: Axon cable model with the electrode modeled as a point source [55].

a commercial device.

2.3.3. Charge Metering

Although the switched mode voltage stimulators presented in the previous section add control to the stimulation intensity during voltage mode stimulation, the injected charge during stimulation is still unknown in both implementations. The injected charge can be measured by integration of the stimulation current. A capacitor is used as integrating component in most integrators [57]. The injected charge is represented by the voltage over the capacitor as described by (2.3).

$$V = \frac{1}{C}\int i\,dt = \frac{Q}{C} \tag{2.3}$$

A simple implementation of a current integration uses a sensing capacitor in series with the tissue [58, 59]. A disadvantage of this implementation is the voltage drop over the capacitor, limiting the headroom of the stimulator. In order to keep the voltage drop low, the capacitor value could be increased; however, the capacitor values required for stimulator parameters are often too big for integration on a chip [60]. Off-chip capacitors increase the total volume of the system dramatically, making this method unpractical in most stimulation applications. The design presented in [60] uses a small capacitor and a digital counter to measure the injected charge. The capacitor is used to sense a small packet of charge, Q_{unit}. A digital counter is used to record the total amount of charge packets delivered to the tissue. This allows the design to have a low voltage drop while using a small capacitor. Also, the digital output of this method is beneficial for integration of the measured charge in the digital control.

Another possible implementation of a low voltage drop current monitor is a shunt resistor in series with the tissue [61]. The voltage across the resistor represents the real-time stimulation current. The voltage is integrated using an active voltage integration circuit, resulting in the injected charge. The disadvantage of this implementation is the active circuit that requires area and power. Moreover, the implementation suffers from sampling and gain errors.

Last, instead of directly integrating the stimulation current, a copy of the stimulation current can be used [57]. Copying the stimulation current using a current mirror allows for current scaling before integration. This can be beneficial in applications requiring a high dynamic range in the injected charge.

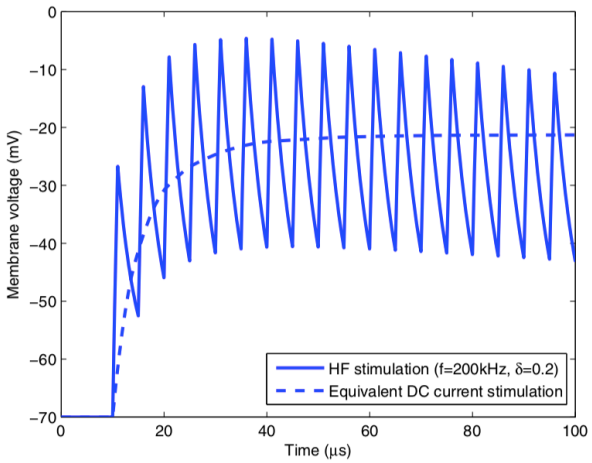

Figure 2.10: Simulation of the membrane depolarization caused by a UHF voltage pulse compared to a constant current pulse [56].

Furthermore, the direction of the integration current can be reversed while the stimulation current is constant. This is used in the design of [57] to create a periodical signal for integration.

In conclusion, although direct current integration using a capacitor offers the most accurate charge measurement, the required size of the capacitor makes it impractical for neurostimulators. To decrease the size of the capacitor, sampling of multiple charge packets can be used. However, sampling errors decrease the accuracy of measured charge. Thus, this implementation is a trade-off between area and accuracy. The other proposed implementations require active circuitry or a copy of the current, which increases the power consumption of the measurement. Also, sampling errors are present in both methods. Therefore, sampling charge packets on a small capacitor is the preferred implementation for small area, low power charge metering.

2.3.4. Stimulation Safety: Charge Balancing

The first and most common approach of charge balancing is the addition of a passive charge balance phase to the stimulation waveform. During passive charge balancing, both electrodes are connected to the same potential after a stimulation pulse [22]. This leads to the removal of any residual charge at the electrode interface. However, the rate of discharge depends on the time constant τ_{dis}, which is mostly determined by $R_s C_{dl}$. Particularly in applications using micro-electrodes (high impedance), the time constant will limit the discharging capabilities of this method [62]. Therefore, the passive charge balancing method should only be used for applications with small charge mismatch and low electrode impedances or in combination with other charge balancing techniques.

For applications where passive discharge is insufficient, active approaches should be implemented. Active charge balancing techniques presented in literature can be divided into three categories. In the first category, an active charge injection phase is added after the stimulation waveform. This idea was first introduced in the pulse insertion method of [63]. In the pulse insertion method, a measurement of the tissue voltage after stimulation is done. Based on the voltage, a short current pulse with opposite polarity is inserted. The insertion of pulses is repeated until the measured tissue voltage is inside predefined safety margins. The operation of the pulse insertion method is illustrated in Fig. 2.11a.

The second category of active charge balancing adapts the stimulation waveform based on the imbalance measured in preceding waveforms. For example, the circuit presented in [64] samples the electrode voltage after one stimulation pulse. Based on the sample, either the amplitude or phase duration of the second phase of following pulses is adjusted. The closed loop design converges to a stimulation pulse after which no residual charge is left over. The resulting waveform is depicted in Fig. 2.11b. Similarly, the closed loop system presented in [65] adjusts the stimulation parameters to minimize the charge error. Moreover, in the offset-regulation method presented in [62], an offset current is added to the stimulation current to minimize the charge imbalance. The design in [66] combines pulse insertion with waveform adaptation. After the first stimulation pulse, multiple insertion pulses are needed to reach charge balance. Adaptation of the stimulation parameters minimizes the number of

insertion pulses required for following stimulation pulses.

In the last category of active charge balancing, the second stimulation phase is combined with the charge balancing phase. The stimulation waveform in both [67] and [68] has a pulsed anodic phase. In between the pulses, the tissue voltage is sampled until the desired safe region has been reached. The resulting waveform is illustrated in Fig. 2.11c. An advantage of this method is that it prevents overcompensation of the injected charge during the second phase. In voltage stimulation, this is especially important to prevent the electrode potential from exceeding the safe limits [68]. Moreover, this makes the stimulation waveform more efficient because both overcompensation in the second phase and restoration thereof is a waste of energy in the first two categories.

In conclusion, charge balancing can be implemented with both passive and active schemes. The passive method is often not fast enough for systems using micro-electrodes and high repetition frequencies. Therefore, active charge balancing techniques are required to rapidly bring the residual voltage to a safe limit. The safety window for residual voltage is often considered to be $\pm 50\,\text{mV}$ [69] or $\pm 100\,\text{mV}$ [70]. A small amount of leftover charge after active charge balancing can be removed using a passive charge balancing period.

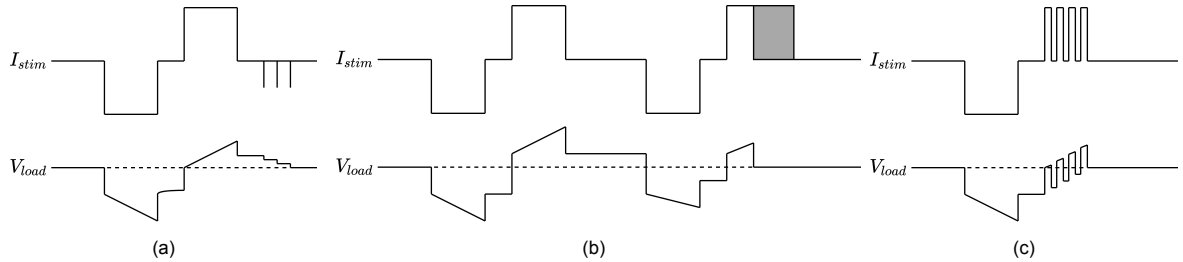

Figure 2.11: Illustration of the three categories of active charge balancing presented in literature. (a) Pulse-insertion: applying short stimulation pulses after the second stimulation phase, based on the sampled residual voltage. (b) Waveform adaptation: Based on the sampled residual voltage, waveform parameters (phase length or amplitude) of successive pulses are adapted. (c) A priori charge balancing: Active charge balancing is combined with the reversal phase of stimulation to prevent overcompensation of injected charge.

2.3.5. Multi-Channel Stimulation

The application of this project requires a multi-channel stimulator, meaning that multiple electrodes need to be stimulated at the same time. In that way, a pixelized vision could be created. There are several ways to achieve multi-channel stimulation, as will be shortly discussed below.

First of all, each channel could have its own stimulation source. The full system implementations presented in [15] and [46] contain a separate current source for each output channel. As a current signal is not easily distributed to parallel channels, this implementation will often be required for current mode stimulators. Also, for safe voltage mode stimulation, each channel will need to have its own charge monitor.

Another possibility is to group multiple electrodes to one stimulation source. In this implementation, it is not possible to stimulate all output electrodes at the same time; however, it might not be necessary for the application to do so. The intracortical stimulator presented in [17] consist of stimulation modules, each module is connected to 16 electrodes and can stimulate a maximum of four channels at the same time. The stimulator presented in [71] connects five current sources to twenty electrodes. The system is able to deliver spatio-temporal patterns to the electrodes: each stimulation source delivers stimulation pulses to multiple electrodes in an interleaved fashion. As can be seen from the typical stimulation parameters presented in Table 2.1, interleaved stimulation is possible for intracortical visual stimulation. When stimulation pulses of 500 µs (biphasic pulse with interphase delay) at a frequency of 200 Hz $\left(t_{rep} = 5\,\text{ms}\right)$ need to be stimulated at each channel, up to ten electrodes can be connected to each stimulation source.

Last, a single stimulation source could be used to stimulate multiple channels in parallel. The current mode UHF switched stimulator presented in [25] is capable of interleaving UHF pulses to multiple channels. However, this way of interleaving comes at the cost of reducing the pulse frequency which might affect the efficacy of the system.

To conclude the state-of-the-art analysis, a qualitative comparison of the discussed stimulation meth-

ods is presented in Table 2.3. In this table, the charge balancing column is an assessment of the possibility to combine each stimulation method with active charge balancing methods discussed in Section 2.3.4.

Table 2.3: Comparison of the improved stimulation methods regarding efficiency, safety (charge control and prospect for charge balancing) and size.

Stimulation Method*	Multi-channel Efficiency	Charge Control	Size	Charge Balancing	Implemented in
UHF CMS	+	+	-	++	[25, 47]
DVS CMS	-	+	-	+	[48–51]
DVS VMS	-	-	-	+	[26, 54]
UHF VMS	+	-	+	++	[55]

**UHF = ultra high frequency, CMS = current mode stimulation, DVS = dynamic voltage scaling, VMS = voltage mode stimulation.*

2.4. Thesis Objectives & Approach

Based on the literature presented in this chapter, it is hypothesized that the combination of the UHF switched voltage stimulation method and an appropriate charge sensing method could lead to an efficient, safe and implantable multi-channel stimulator. The UHF stimulation technique is promising for the visual cortex stimulator for the following reasons:

- Pulse width modulation allows for stimulation intensity control on each channel without affecting stimulation efficiency of other channels.
- The pulse width modulated waveform benefits from efficiency of voltage mode stimulation.
- The stimulation pulse is divided into small pulses injecting small amounts of charge for each pulse. An on-chip capacitor could be used to sense the injected charge during each pulse.
- Adjustment of the duty-cycle could be used to control injected charge.
- As the stimulation waveform is already pulsed, charge balancing can be integrated into the second stimulation phase as was done in [67].

The objective of this thesis is to come to a system design to validate this hypothesis. A multi-channel UHF voltage stimulator using a novel charge monitoring circuit will be designed. Furthermore, the system will make use of an active charge balancing scheme to ensure stimulation safety.

3

System Design: Charge Controlled UHF Voltage Multi-Channel Stimulator

This chapter describes the design process of the proposed stimulator circuit. First, system level design considerations for the implantable neurostimulator are covered. Based on these considerations, a stimulation source capable of multi-channel intracortical stimulation is designed. Finally, the circuit is implemented on a printed circuit board (PCB) for validation.

3.1. Intracortical Visual Stimulator Design

3.1.1. System Level Architecture

The application of intracortical visual stimulation requires a system that stimulates many electrodes covering a large area. As has been discussed in Chapter 2, either a modular or distributed system level architecture is most suitable in this situation. For both architectures, electrodes will be distributed over the visual cortex by means of stimulation modules. A disadvantage of the modular approach is the necessity for interconnections between the stimulation modules and a central module. Movement between the modules will cause stress on the leads, possibly causing system failure. On the other hand, the use of a central module is advantageous because it can be aligned to the external system components for optimal energy and data transfer. A distributed approach does not have interconnections between system modules, taking away an important failure mechanism. On the other hand, the stimulation modules become more complex as each module requires its own communication and power regulation circuits. Furthermore, it is more difficult to position each module for optimal alignment with external system components, which decreases power transfer efficiency and data transfer integrity. Apart from communication, data control and power regulation, the stimulation modules are similar for both architectures. Depending on the number of electrodes and the technique used for multi-stimulation, each module requires a number of stimulation sources.

For this specific application, spatio-temporal multi-channel stimulation is suitable. In spatio-temporal stimulation, multi-channel stimulation is achieved by time interleaving of channels with a single stimulation source. Considering typical stimulation pulses with a duration of 500 µs at a frequency of 200 Hz $(t_{rep} = 5\,\text{ms})$, a source stimulating only one single channel would not be used most of the time. The period between stimulation pulses can be used to share the source between multiple channels. Doing so has a number of advantages in terms of area, safety and power. First of all, only $\frac{M}{N}$ stimulation sources capable of stimulating N channels are needed in a system with M output channels. This is both beneficial for the total area of the circuit and for safety. Sharing resources creates design space for the stimulator to implement monitoring and charge balance circuits which can improve safety of stimulation. Moreover, spatio-temporal stimulation relaxes power requirements of the system. If all channels would be stimulated synchronously using separate stimulation sources, this would demand high peaks of power followed by an idle period of low power demand. Using spatio-temporal stimulation, the total power is spread out over the period, lowering the instantaneous power requirements. Considering the advantages described above, a stimulation source as part of the stimulation module

used in distributed and modular architectures will be designed. For this design, it is assumed that a constant supply voltage is available from either a central module or local power circuitry.

In Chapters 1 and 2, the importance of an active charge-balancing circuit has been illustrated. Similar to the stimulation source, this circuit will be shared among multiple output channels. The implemented active charge-balance method cooperates with the stimulation source to ensure safety, as will be explained in Section 3.4. Again, this implementation saves chip area and power consumption of the total system.

3.1.2. Stimulator Proposal: Charge Controlled UHF Voltage Stimulation

Based on the literature review presented in Chapter 2, it was decided to design a stimulation source based on the UHF voltage stimulation method in [55]. However, this method lacks charge control as will be explained below. Therefore, a novel addition to this method is proposed. The principle of operation will be explained in this section and the design of the circuit is described in Section 3.3.

In visual stimulation, the phosphene threshold of each stimulation channel is determined during a threshold procedure. One possible procedure to determine the threshold of a stimulation channel is to a use fixed set of stimulation parameters (t_{ph}, t_{ip} and t_{rep}) while gradually increasing the stimulation intensity (charge per phase) until a phosphene is perceived. The goal of this procedure is to find the minimal stimulation intensity that leads to the perception of a phosphene for each stimulation channel. For UHF voltage stimulation, the intensity can be scaled by changing the duty cycle of the signal. One problem of using a fixed duty cycle is that the stimulation intensity depends on the tissue impedance. When the threshold is determined at a certain time instance, variance of the tissue impedance over time will change stimulation intensity causing either under- or overstimulation of the tissue. With understimulation the cell is not activated, while overstimulation causes wasted power as the same result could be reached with less power. More importantly, overstimulation could lead to harmful situations for both tissue and electrodes. Thus, controlling stimulation intensity using a fixed duty cycle is not effective and possibly dangerous. Instead, a novel stimulation method with a dynamic duty cycle is presented in this thesis: Charge controlled UHF voltage stimulation.

A block level circuit diagram of the proposed stimulator is depicted in Fig. 3.1. In the proposed design, stimulation intensity is controlled based on injected charge instead of the duty cycle. The duty cycle will be controlled dynamically such that the stimulation intensity does not change when the tissue impedance changes. For this stimulation principle it is assumed that a channel with varying tissue impedance requires the same amount of charge for successful cell activation. This assumption can be justified by the fact that conventional current mode stimulation works in the same way: For a varying load, the current stays constant and thus the amount of charge injected during one phase is also constant. Furthermore, impedance changes are mostly caused by changes in the tissue surrounding the electrode rather than changes in the target cell. Therefore, it is assumed that the strength-duration curve of the target cell will not change with changes in channel impedance and thus a constant strength (charge/phase) and duration will lead to cell activation.

The UHF voltage technique modulates stimulation pulses at a known switching frequency f_{sw}. For a given phase duration t_{ph}, the stimulation source will apply $N = t_{ph} f_{sw}$ pulses to the channel. If the threshold charge for a given phase duration is determined to be Q_{th}, the charge injected during each UHF pulse has to be $Q_{UHF} = Q_{th}/N$ for cell activation. The proposed stimulator monitors the charge during each UHF pulse and dynamically controls the duty cycle in order to satisfy $Q_{UHF} = Q_{th}/N$ for each UHF pulse.

3.1.3. Stimulation Source Requirements

Based on information presented up until now, the following set of requirements have been conducted for the stimulation source:

- The source should produce biphasic waveforms with configurable parameters t_{ph}, t_{ip}, t_{rep} and intensity. The parameters should at least be configurable to the typical values listed in Table 2.1.
- Multiple-channels should be stimulated in a spatio-temporal pattern.
- During a stimulation phase of 200 µs, the system should be able to deliver 1 nC to 20 nC to the tissue, corresponding to a stimulation current of 5 µA to 100 µA.

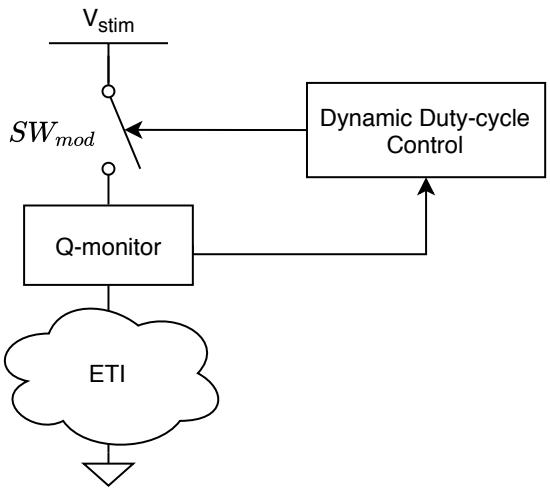

Figure 3.1: Block level diagram of the proposed design consisting of a modulation switch SW_{mod}, a charge monitor *Q-monitor* and a dynamic duty-cycle controller.

- The source should be able to deliver pulses to loads equivalent to the linear ETI model with R_s = 50 kΩ to 150 kΩ, $Z_{faradaic}$ = 1 MΩ and C_{dl} = 40 nF.
- The duty cycle of the stimulation waveform should be dynamically controlled in order to keep the stimulation intensity constant for a varying load impedance.
- An active charge balancing scheme should ensure safety of repetitive stimulation by ensuring a residual voltage over C_{dl} of less than ±50 mV [69].

3.2. Circuit Diagram of Proposed Design

A circuit diagram of the proposed proposed stimulation source is depicted in Fig. 3.2. The circuit consists of the following components:

- **Constant voltage source -** Supplied by the central module or local power regulators on the stimulation module.
- **Modulation switch SW_{mod} -** Used for pulse width modulation of the UHF stimulation signal.
- **Multi-channel H-bridge -** By connecting one electrode to V_{anodic} and one electrode to V_{sense}, a bipolar electrode configuration can be created. In Fig. 3.2, a stimulation channel is created between electrodes one and two for illustration. A biphasic pulse is created by connecting the electrodes to the opposite node for the reversal phase of the waveform.
- **Dynamic duty cycle controller, Q-control -** Controls the modulation switch based on the principle introduced in Section 3.1.2.
- **Charge balancing circuit -** Measures the residual voltage at the ETI. Logic output goes to digital control unit.
- **Digital control -** Controls the H-bridge and the duty cycle controller to create biphasic stimulation waveforms.

Operation and design of the duty cycle controller and charge balancing circuit are described in the following sections.

3.3. Dynamic Duty Cycle Controller

The charge control principle introduced in Section 3.1.2 requires a controller that is able to monitor the charge during each UHF pulse and control the modulation switch SW_{mod} in order to create a dynamic

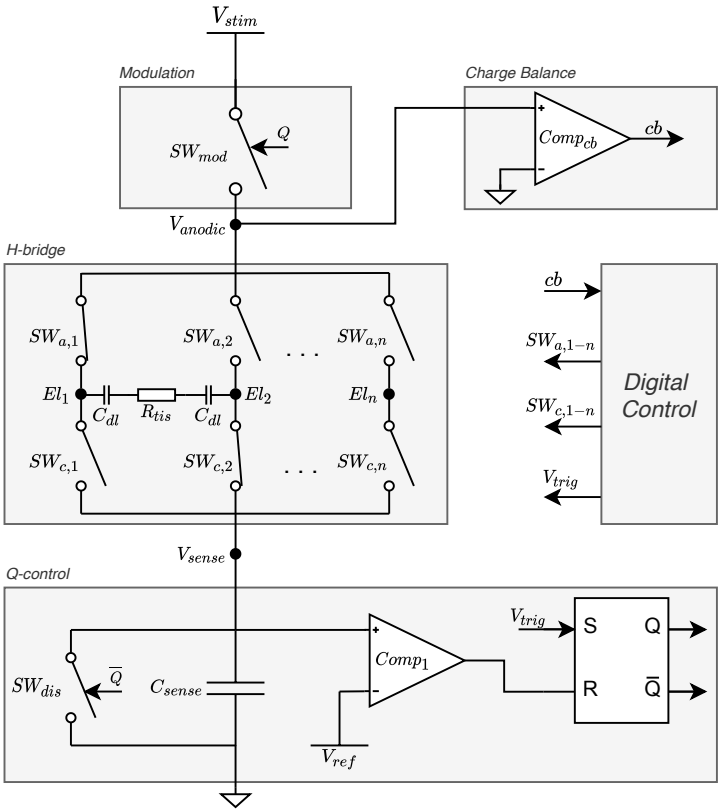

Figure 3.2: Circuit diagram for dynamic duty cycle control with active charge balancing. The charge controller controls modulation switch SW_{mod}. The multi-channel H-bridge control signals, V_{ref} and V_{trig} are generated by digital control.

duty cycle. This is implemented using a monostable multivibrator, which is an oscillator circuit with one stable state [72]. Monostable multivibrators are commonly used to produce a single pulse with an accurate duration when triggered externally. In this case, the control loop will produce a single pulse inserting a predefined amount of charge.

3.3.1. Monostable Multivibrator Design

The operation of a monostable multivibrator can be described using the state-model representation depicted in Fig. 3.3. Each circle represents a state of the system and an arrow between two state

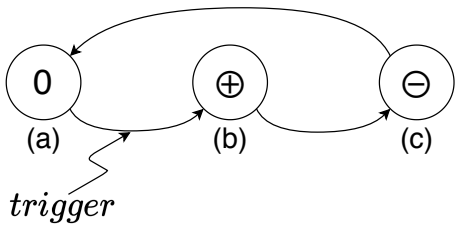

Figure 3.3: State-model representation of a mono-stable multivibrator consisting of three states: a, b and c. The sign of the integration signal is indicated inside the states. A circle around the integration sign indicates an auto-excitatory state. State (a) is a stable state. The external trigger signal is required for the transition from state (a) to (b). Figure reproduced from [72].

represents a state transition. In each state, the input signal of the system is integrated with an integration constant α. The sign inside a state represents the sign of the integration constant. The output of the integrator is described with $E_o(t)$. Auto-excitatory states have a threshold value for $E_o(t)$ at which a state-transition automatically occurs. In Fig. 3.3, state (b) and (c) are auto-excitatory states. State (a) has an integration constant of 0, which is also called a degenerated or stable state. An external trigger is required to initiate a state-transition between states (a) and (b). The state-duration of an

auto-excitatory state can be calculated using (3.1), where E_x is the threshold value of state X.

$$T_x = \frac{E_x - E_o(0)}{\alpha} \tag{3.1}$$

If the previous state was also auto-excitatory, $E_o(0)$ will be the threshold value of the previous state. Also, because α is 0 in a stable state, the output value of the integrator will not change in that state. Therefore, the state-duration in a monostable multivibrator can be accurately known with careful design of α, E_b and E_c.

There are four essential functions that need to be performed in a practical oscillator[72]:

1. Integration
2. Comparison
3. Switching the sign of α
4. Memorization

In practical oscillators, the input signal is often an accurately defined constant current and integration of the current is done using a capacitor [72]. The voltage over the capacitor is then $E_o(t)$. Switching the sign of α is necessary in practical oscillators to be able to create periodical signals. In case of an integrating capacitor, the output voltage would approach infinity if α does not change sign. In practice, this would lead to distortion of the output signal. Memorization is needed for the system to know to which threshold value $E_o(t)$ should be compared. As the system described in Fig. 3.3 has only two threshold values (E_b and E_c), a single bit memory is sufficient.

3.3.2. Ideal Circuit Operation

In the proposed circuit the integration current is not constant and thus, the pulse duration will also not be constant. Instead, a monostable circuit is used to deliver a defined amount of charge for each UHF pulse. The timing diagram for the proposed circuit is illustrated in Fig. 3.4. In Fig. 3.5 the signals of the control loop during a single UHF pulse are depicted. An UHF pulse is initiated by an external trigger signal V_{trig}, triggering the SR-latch. Output Q of the latch controls SW_{mod} and current starts to flow through the tissue. A capacitor C_{sense} in series with the tissue integrates the current through the tissue. A comparator compares the voltage on C_{sense} to a reference voltage, V_{ref}. When the reference voltage has been reached, the comparator resets the latch. Consequently SW_{mod} will open, stopping the current going into the tissue. Also, SW_{dis} is closed, causing C_{sense} to discharge. The amount of charge applied to the tissue during a single pulse is equal to $Q_{UHF} = C_{sense}V_{ref}$. During a phase of length t_{ph}, N UHF pulses will be applied to the tissue, where $N = t_{ph}f_{sw}$. Combining all above, the total amount of charge applied to the tissue during one stimulation phase is described by (3.2).

$$Q_{ph} = Q_{UHF}N = C_{sense}V_{ref}t_{ph}f_{sw} \tag{3.2}$$

The trigger signal as well as the H-bridge switches are controlled by a digital control circuit in order to create biphasic stimulation pulses with defined phase durations.

The circuit incorporates all essential oscillator functions using separate components: Current integration with capacitor C_{sense}, a comparator to compare the output of the integrator to V_{ref}, reversal of the integration signal using switches SW_{mod} and SW_{dis}, and a SR-latch as a one-bit memory. Separation of the essential functions by individual components is advantageous as each component can be optimized for its specific function [72].

The system has three states: S_0, S_1 and S_2, as indicated in Fig. 3.5. It can be represented using the state-model of Fig. 3.3. S_0 is the degenerated state of the system. Switch SW_{mod} prevents current from flowing into the tissue while SW_{dis} ensures V_{sense} to be 0 V. The stable state is not auto-excitatory and a state transition can only occur using an external trigger signal on the input of the SR-latch. After an external trigger is applied (V_{trig} = *HIGH*), the system transits to state S_1. During S_1, SW_{dis} is open and SW_{mod} is closed, allowing current to flow trough the load and to charge up the integrating capacitor C_{sense}. Using the linearized ETI model as load, the current through the load during S_1 is described by (3.3). Where $V_{Cdl,0}$ is the voltage built up over C_{dl} at the beginning of the pulse and $\tau_1 = R_{tis}(\frac{C_{dl}C_{sense}}{C_{dl}+C_{sense}})$.

$$I_{S1}(t) = \frac{(V_{stim} - V_{Cdl,0})e^{-t/\tau_1}}{R_{tis}} \tag{3.3}$$

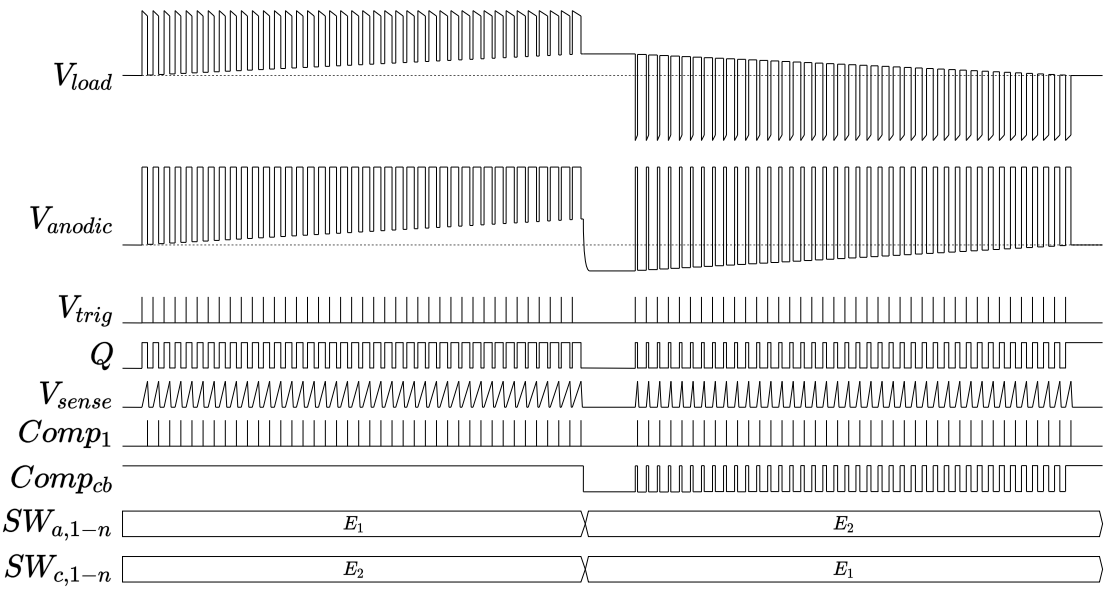

Figure 3.4: Timing diagram for the proposed circuit for one biphasic stimulation pulse.

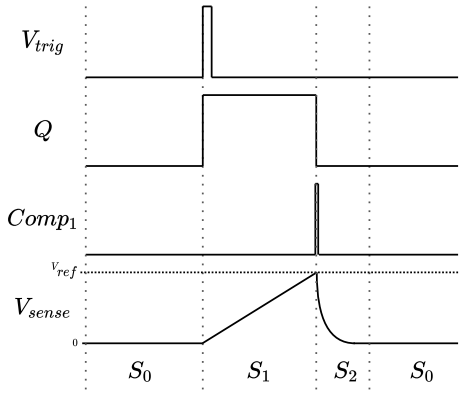

Figure 3.5: Timing diagram for the proposed control loop for a single UHF pulse. System states are indicated at the bottom.

When the integrator is chosen such that $C_{sense} \ll C_{dl}$, the time constant can be approximated to $\tau_1 \approx R_{tis}C_{sense}$. Furthermore, the integrator output during S_1 is given by (3.4).

$$E_{o,S1}(t) = \frac{1}{C_{sense}} \int_0^t I_{S1}(t)dt = \frac{Q(t)}{C_{sense}} \tag{3.4}$$

When $E_o(t) = V_{ref} = Q_{UHF}/C_{sense}$, the system becomes excited and a transition to the last state, S_2, occurs. The state duration of S_1, found by solving (3.4) for t, is given by (3.5).

$$T_{S1} = -\tau_1 \ln(1 - \frac{Q_{UHF}R_{tis}}{(V_{stim} - V_{Cdl,0})\tau_1}) \tag{3.5}$$

During S_2, SW_{mod} is opened and thus no current will flow into the tissue. SW_{dis} closes and discharges C_{sense} at a rate of $\tau_2 = R_{on}C_{sense}$, where R_{on} is the on-resistance of SW_{dis}. Discharging C_{sense} means that the integration signal has switched sign and the integrator output is expressed using (3.6).

$$E_{o,S2}(t) = V_{ref}e^{-t/\tau_2}. \tag{3.6}$$

After $5\tau_2$, C_{sense} is considered to be fully discharged and the system automatically transitions to S_0 waiting for a next trigger signal. The state duration of S_2 is given by (3.7).

$$T_{S2} = 5R_{on}C_{sense} \tag{3.7}$$

For correct operation of the circuit, it is important that the system has returned to the stable state before a new trigger signal is given. Therefore, the system should be designed such that $T_{S1}+T_{S2} < T_{sw} = \frac{1}{f_{sw}}$. Also, stimulation of the tissue only happens during S_1 and thus for maximal stimulation capability, T_{S2} should be much smaller than T_{S1}.

3.3.3. Position of Integration Capacitor

The control loop requires an integration capacitor in series with the tissue. There are three possible locations along the signal path for said capacitor, as illustrated in Fig. 3.6. For a monopolar electrode configuration, all channels share a common return electrode. Location 3 makes a monopolar configuration with multiple stimulation sources impossible as the integrator will sense current from all active channels in the system. For both locations 1 and 2, a differential amplifier is required to measure the voltage across the sensing capacitor. This adds area, power and inaccuracy to the system. Moreover, the monopolar configuration would require a separate control loop for anodic and cathodic stimulation phases, increasing power consumption and size of the stimulator even more. Lastly, locations 1 and 2 will suffer more from switching artifacts as one terminal of the capacitor is connected to SW_{mod}. During stimulation this switch switches the voltage between 0 and V_{stim}. Switching artifacts, including charge injection and clock feed-through, will put charge on the integrating capacitor causing a measurement error. On the other hand, at location 3 the capacitor is connected to ground and the side of the tissue that is not switching during stimulation. In conclusion, unless a monopolar electrode configuration is absolutely necessary for the application, location 3 is favorable for the integrating capacitor. For multichannel stimulation, a bipolar electrode configuration has several benefits over monopolar as explained in Section 2.1.2. Therefore, the proposed circuit has a bipolar configuration with the integrating capacitor placed at location 3. It should be noted that additional H-bridge switches around the tissue are required for bipolar stimulation.

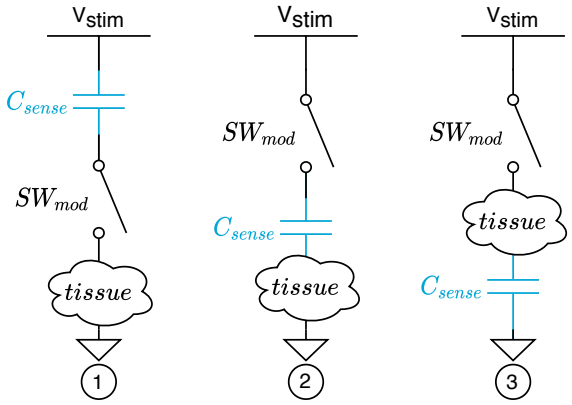

Figure 3.6: Three possible locations for the integration capacitor C_{sense} in series with the tissue.

3.3.4. Circuit Implementation Non-Idealities

Up until now, ideal components have been considered to describe the system. However, real components are non-ideal and will lead to inaccuracy of the measured stimulation charge. It is important to identify sources of inaccuracy to consider trade-offs in the circuit design.

First of all, a delay introduced by the control loop leads to inaccuracy. This is illustrated by Fig. 3.7. The charge error that is introduced by the delay can be calculated with (3.8).

$$Q_{err} = \int_{T_{S1}}^{T_{S1}+\Delta t} I_{S1}(t)dt = \frac{V_{err}}{C_{sense}} \tag{3.8}$$

The severity of this error depends on the tissue impedance and T_{S1}. For decreasing tissue resistance, $I_{S1}(t)$ and thus Q_{err} increase. Furthermore, the error is a fraction of the ideal charge proportional to $\frac{\Delta t}{T_{S1}}$. Thus, the same time delay introduces a bigger error for short UHF pulses. Additionally, the time

delay is not constant as the propagation delay of the comparator depends on the overdrive voltage at its input. Since the error is not constant, the system can not be calibrated to compensate for this inaccuracy.

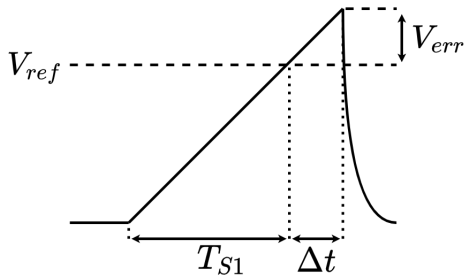

Figure 3.7: Output signal of the integrator for a single UHF pulse with delay Δt caused by the control loop. The pulse should stop when V_{ref} has been reached. The time delay results in a charge inaccuracy.

Second, parasitic capacitance at both sides of the tissue lead to measurement errors. Parasitics originate from the switches and comparator inputs connected to either node. At node V_{sense}, parasitic capacitance to ground leads to a gain error as $E_{0,S1}(t) = Q(t)/(C_{sense} + C_p)$ instead of (3.4). This error can be compensated for by calibration of the circuit. During S_1, parasitic capacitance at node V_{anodic} will be charged to V_{stim}. When the system transitions to S_2 and SW_{mod} opens, the capacitance will discharge over the tissue. If the capacitance discharges completely, this will introduce a charge error equal to $C_p V_{stim}$ for each pulse. As the error is not tissue dependent, the system could be calibrated for this error. Instead, if the capacitance can not discharge completely in between UHF pulses, the error becomes unpredictable and thus can not be compensated for.

Last, switching artifacts of switch SW_{dis} will cause sensing errors. When the switch opens at the beginning of S_1, clock feedthrough and charge injection cause some charge on the integration capacitor. It is important to notice that scaling C_{sense} does not change the measurement error. In integrated circuit technology, several compensation techniques exist to minimize switching artifacts such as the use of dummy switches.

3.3.5. Stimulation Intensity Control

As described above, the proposed circuit is able to produce UHF pulses with a defined amount of charge, Q_{UHF}. In order to control the intensity of stimulation, Q_{ph} should be adjustable. Looking at (3.2), it can be seen that three parameters can be used to scale Q_{ph} independently of t_{ph}: f_{sw}, C_{sense} & V_{ref}.

Important considerations on which parameter should be scaled are: effect of scaling on charge error, power efficiency and ease of implementation. First of all, scaling f_{sw} effectively scales the number of UHF pulses in one phase. The errors identified in the previous section apply to a single UHF pulse and thus scale with the number of pulses in each phase. Moreover, switching losses increase for higher f_{sw} and consequently the power efficiency of the circuit will decrease. Also, the trigger signal can not be used among multiple stimulation sources. When a fixed f_{sw} is used, the trigger signal can be shared which saves area and power. Second, scaling C_{sense} adds complexity to the charge integrator. Switches required to change the capacitor value introduce more parasitic capacitance to the node and, as C_{sense} changes, the effect of the parasitic capacitance is not constant. This implementation requires accurate capacitors which can not be calibrated after production. Last, scaling V_{ref} has some advantages over the other parameters. The charge error caused by parasitics around C_{sense} and switching artifacts is constant for all intensities and can be compensated for. Therefore, the accuracy of C_{sense} is also not critical for linearity in this case. Moreover, energy loss of charging C_{sense} scales proportional to the stimulation intensity. Also, multiple stimulation sources can share the voltage converter to save area and power.

Considering all of the above, the circuit has been implemented with a fixed f_{sw} and C_{sense} while stimulation intensity is controlled using V_{ref}.

3.4. Active Charge Balancing

Active charge balancing is important in order to prevent potential harmful conditions at the ETI, as has been explained in Chapter 2. The purpose of active charge balancing is to leave no residual charge on the capacitive double layer after stimulation. In other words, the voltage drop across C_{dl} should be 0V at the end of a stimulation pulse. In current mode stimulation, the voltage across the interface capacitance can not be measured during stimulation due to the voltage drop across the resistive part of the tissue. Therefore, most existing charge balancing methods restore charge balance after a completed stimulation pulse. In this method, the second phase 'overcompensates' the injected charge and charge balancing has to restore the overcompensated amount of charge. Fortunately, the pulsed characteristic of UHF stimulation allows for charge monitoring during stimulation. This prevents overcompensation of the second phase and leads to a safer and more power efficient charge balancing method.

The proposed design requires one comparator connected to V_{anodic} (see Fig. 3.2) for charge balancing. The implemented method works as follows. In Fig. 3.4, it can be observed that the voltage at V_{anodic} returns to V_{load} in between UHF pulses. Because there is no current flow through the tissue, this voltage represents the voltage drop over C_{dl}. During the interphase delay, the load is reversed and thus V_{anodic} is charged towards $-V_{Cdl}$ in the second phase. During the second stimulation phase, this voltage slowly rises towards 0V. In order to detect charge balance, a zero-crossing of this inter-pulse voltage has to be measured. The charge balancing comparator $COMP_{cb}$ compares V_{anodic} to ground in the proposed circuit. During an UHF pulse, $V_{anodic} = V_{stim}$ resulting in a $HIGH$ output of the comparator. In between the pulses, when V_{anodic} is negative, the comparator output is LOW. This information is used in the digital control circuit to determine when to stop the second stimulation phase. After a trigger signal is given, the control circuit waits for the comparator output to change to LOW. When this happens, a new trigger is given to the circuit. If the comparator output does not change to LOW, it means that charge balance has been reached and the stimulation will stop. The active charge balancing process can be followed by a passive discharge phase by connecting both electrodes to V_{sense}, while SW_{dis} is closed.

3.5. Prototype PCB

A prototype PCB was developed for validation of the proposed design. The circuit diagram of the implemented PCB, which includes the proposed design of Fig. 3.2 with additional components for correct operation of the circuit, is depicted in Fig. 3.8. The additions to the circuit will be discussed in the next section. As seen in Fig. 3.8, the PCB has 8 output pins, labeled with $El_0 - El_7$. In this way, multi-channel operation of the circuit can be verified for up to 4 stimulation channels. The digital control of the circuit is implemented using a Digilent Cmod S7 field programmable gate array (FPGA) module.

3.5.1. PCB circuit implementation

The switches in the circuit have been implemented using analog switch integrated circuits (IC) from *Analog Devices*. Analog switch ICs are optimized for minimal switching artifacts. Moreover, controlling the switches can be done using digital signals whereas using MOSFETs as switches would require additional drivers for high-side switching. In Fig. 3.8, a white box represents an IC with input/output signals, supply voltages and possibly control signals.

An important step in the design was selecting values for the circuit parameters C_{sense},V_{ref},f_{sw} and V_{stim}. A switching frequency of 200 kHz was chosen based on the frequency used in [55]. This leads to a period of $\frac{1}{f_{sw}}$= 5 µs. Increasing the switching frequency increases switching losses and charge inaccuracy from control loop delays. From the system requirement of charge injection (1 nC–20 nC), using (3.2), it follows that the charge of each UHF pulse has to be $Q_{UHF} = V_{ref}C_{sense}$= 25 pC–500 pC. When V_{ref} is chosen too big, it will limit the current and thus increase the duration of UHF pulses. On the other hand, a low value of V_{ref} suffers from inaccuracy due to switching artifacts and comparator offset. Also, a large value for C_{sense} is desired to minimize influence of parasitic capacitance and noise on the capacitor. For the prototype a value of C_{sense}= 400 pF has been chosen, resulting in a range of V_{ref}= 62.5 mV–1.25 V. In the 0.18 µm CMOS technology node, the typical area for integrated capacitors is in the order of 12 fF/µm^2 [73]. Thus, an area of approximately 0.03 mm^2 would be required to implement C_{sense} on an integrated circuit. To reduce the value of C_{sense}, either f_{sw} or V_{ref} could be increased. The PCB design allows for changing the value of C_{sense} as the capacitor is not soldered to the board. Since

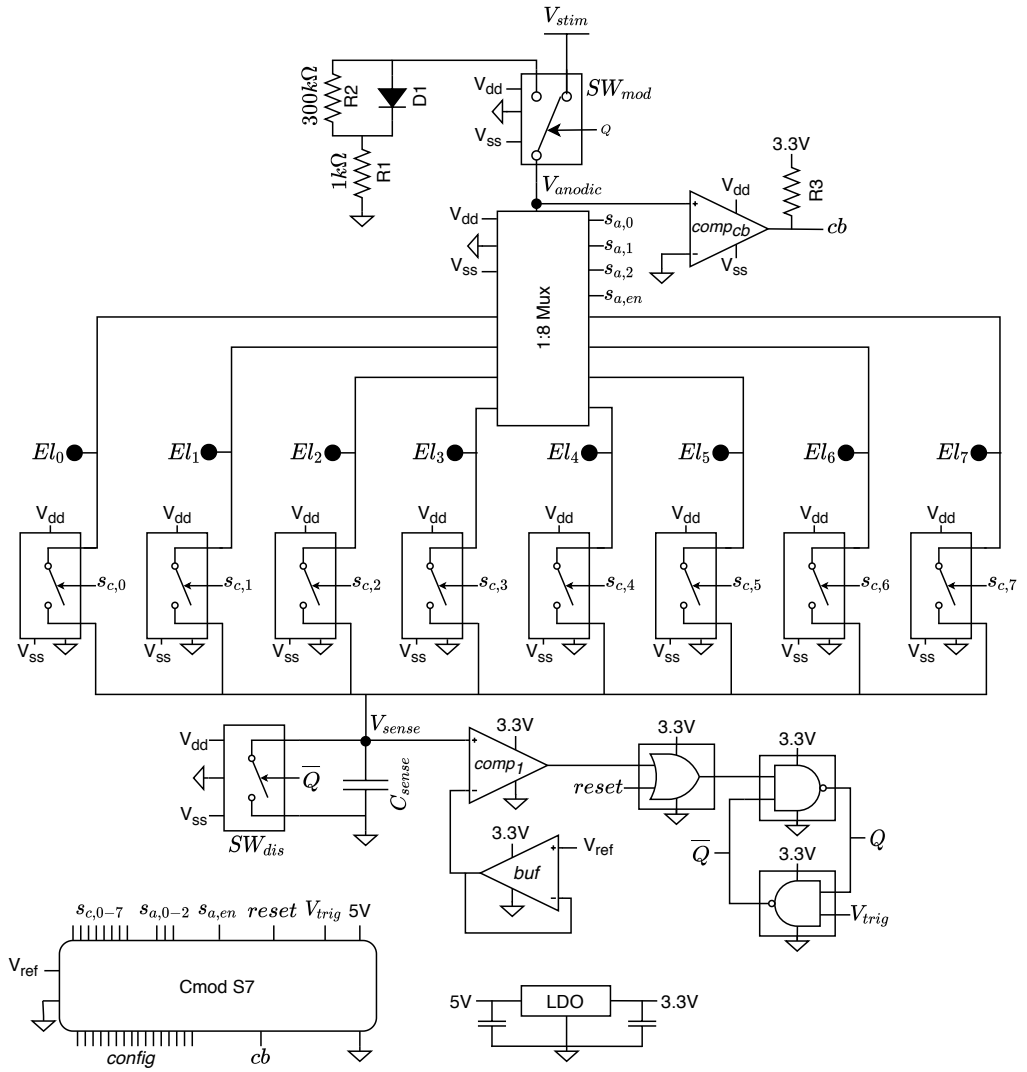

Figure 3.8: Circuit diagram of the implemented PCB. Each white box represents an integrated circuit (IC). Except for Q and $\overline{Q}$, all control signals are connected to the Cmod S7 FPGA module.

f_{sw} is created by the FPGA, an interchangeable sensing capacitor allows the PCB to be configured for a wide range of Q_{ph}. Finally, the required stimulation voltage can be calculated by solving (3.5) using the values mentioned above. Doing this with $Q_{UHF,max}$, $R_{tis,max}$ and assuming V_{Cdl}= 1 V at the end of the waveform, a required stimulation voltage of V_{stim} ≈16.6 V is found. Due to the compliance voltage of the chosen switches, V_{stim} is limited to 15 V for the PCB implementation. As a result, the circuit will not be able to deliver 20 nC when R_{tis}= 150 kΩ. This limitation only applies to combinations of high R_{tis} and high Q_{ph}.

A pull-down network has been added to the circuit, which is placed at the modulation switch SW_{mod}. This modification has to do with the parasitic capacitance at node V_{anodic}. In the previous section it was identified that this capacitance would cause a charge inaccuracy as the capacitance discharges over the load after SW_{mod} is opened. For the PCB, the parasitic capacitance C_p at that node is estimated in the order of 10 pF. On a tissue resistance of 50 kΩ to 150 kΩ, the time constant of discharging becomes 0.5 µs to 1 µs. Given the chosen switching frequency of 200 kHz, the discharging of C_p is not fast enough. If the capacitance is not completely discharged between UHF pulses, it creates an unpredictable charge error. Moreover, this also slows down the proposed charge balancing method. For this reason, the pull-down network ($R_1 - R_2 \parallel D_1$) was added. Instead of leaving V_{anodic} floating, SW_{mod} will switch V_{anodic} between V_{stim} during a pulse and the pull-down network in between UHF pulses. For this purpose, SW_{mod} is implemented using the *ADG1219 SPDT switch*. Requirements

for the impedance of the pull-down network, Z_{pd}, are contradicting. At the end of an UHF pulse, C_p should be discharged as fast as possible to minimize the charge error introduced, e.g. a low Z_{pd} is wanted. On the other hand, low Z_{pd} inhibits the proposed charge balancing method because V_{anodic} is discharged towards ground. Consequently, V_{Cdl} can not be measured. Therefore, high Z_{pd} is desired for the charge balancing method. The solution to this is a combination of two resistors and a diode as can be seen in Fig. 3.8. As long as the forward voltage across the diode is larger than its threshold voltage V_T, the diode will conduct current. For that case, the impedance of the pull-down network is approximately R_1. When V_{D1}<V_T, $D1$ is in reverse bias. This ensures that the pull-down network has a high impedance when V_{anodic} is negative. To prevent break down of the diode, it is important that $|V_{Cdl}| < |V_{breakdown}|$. The value of R_1 is chosen to limit peak currents and R_2 should be bigger than R_{tis} to monitor V_{Cdl} during the second phase.

For charge balancing, $COMP_{cb}$ is implemented using a *LT1011 Voltage Comparator* from *Linear Technology*. This voltage comparator has low input bias current (max. 25 nA), a response time of 250 ns and an open collector output. The output is connected to a pull-up resistor to 3.3 V. In this way, the output of the comparator can be used as input to the FPGA module.

The multi-channel H-bridge is implemented using a 1:8 channel multiplexer (ADG1208) for the anodic switches and 8 separate switches (ADG1201) for the cathodic switches. For the anodic switches, a multiplexer can be used since there is always only a single electrode connected to V_{anodic}. Multiplexing the anodic switches has the advantage of lowering the parasitic capacitance at V_{anodic}, which is important to minimize the charge error. For the cathodic switches, a multiplexer is not sufficient because during the passive discharge phase multiple electrodes have to be connected to V_{sense}.

For the control loop, components were mainly selected to minimize propagation delay as it is the dominant source of error. Furthermore, all components operate at 3.3 V. As for the comparator, the *LT1719* from *Linear Technology* with a propagation delay of 4.5 ns is used. An additional OR-gate has been added to the loop. The OR-gate can be used to reset the circuit from the FPGA. Last, the SR-latch is implemented using two NOR-gates. Logic gates from the *SN74LVC*-series from *Texas Instruments* were chosen, having a propagation delay of only 4 ns. Combined, the delay adds up to approximately 12 ns. The total delay of the control loop is dominated by the turn-on time of SW_{mod}, which is around 150 ns. As an example, this introduces a charge error of approximately 25 pC to each UHF pulse for a resistive load of 100 kΩ. The reference voltage for intensity control is generated using a *Pmod R2R Module*, which is an 8-bit R2R-ladder add-on for the Cmod Module with V_{dd}= 3.3 V. The output voltage is buffered using a *AD8541* opamp from *Analog Devices*.

In total, four voltage levels are used on the PCB. The control loop operates on 3.3 V, which is generated from a 5 V output of the FPGA module using the *ZLDO1117G33TA* low dropout regulator from *Diodes Incorporated*. Furthermore, all switches have a rail-to-rail input compliance operating from an external ±15 V power supply. V_{stim} can be configured to be connected to V_{dd} or supplied from a separate supply, where the condition $V_{stim} \leq V_{dd}$ should hold. A lower stimulation voltage might be wanted when stimulating a low-impedance load.

The PCB prototype is shown in Fig. 3.9 and a summary of the selected components is listed in Table 3.1.

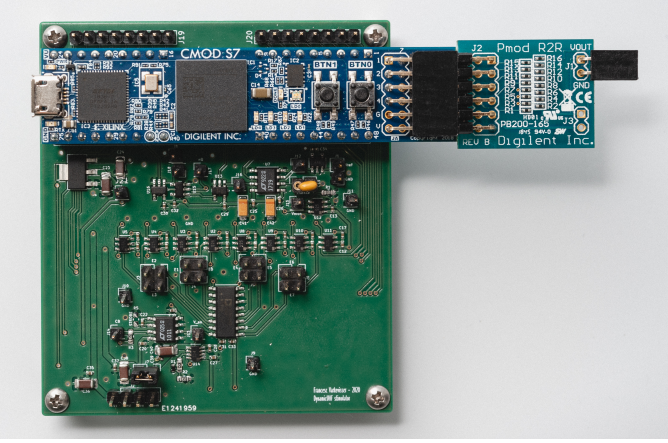

Figure 3.9: The prototype PCB with the *CMOD S7 FPGA Module* and *Pmod R2R DAC module* connected to it.

Table 3.1: List of selected components for PCB implementation.

Function	Selected Component
SW_{mod}	ADG1219 SPDT Switch
$COMP_{CB}$	LT1011 Comparator
$SW_{a,0-7}$	ADG1208 1:8 Multiplexer
$SW_{c,0-7}$	8x ADG1201 SPST Switch
SW_{dis}	ADG1201 SPST Switch
$COMP_1$	LT1719 Comparator
Reset OR	SN74LVC1G02 OR Gate
SR-Latch	2x SN74LVC1G32 NOR Gate
V_{ref} DAC	PMOD R2R DAC Module
V_{ref} Buffer	AD8541 Gen. Purpose Amplifier
Digital Control	CMOD S7 FPGA Module
3.3 V LDO	ZLDO1117QG33TA

3.5.2. Digital control

Digital control of the prototype is implemented using a *Digilent Cmod S7 FPGA Module*, a small development board built around a *Xilinx Spartan 7 FPGA*. An FPGA platform was chosen to facilitate generation of the trigger signal while controlling the H-bridge switches and the reference voltage. The module has 32 digital in/output pins; 14 pins are used as output for control signals of the circuit, 1 output is used for the trigger signal and 1 input is used for the charge balance comparator. The remaining pins are used for configuration of the stimulation signals. The FPGA can be programmed in single or multi-channel mode. In single channel mode, the configuration pins can be used to select the stimulation channel and stimulation intensity. For multi-channel mode, the stimulation parameters are preprogrammed because there are not enough configuration pins. In both modes, charge balancing and passive discharge can be turned on or off with a configuration pin for testing purposes.

The FPGA was programmed in VHDL. The implemented VHDL design consists of a finite state machine (FSM) and a trigger module. The system clock of 12 MHz is scaled down to 10 MHz to ease timing of the control signals. When enabled, the trigger module generates 100 ns (1 clock period) pulses at a frequency of 200 kHz. This module is enabled by the FSM. The state diagram of the implemented FSM is depicted in Fig. 3.10. In the *Idle* state $reset$ is high, maintaining the system in its stable state. Moreover, all cathodic switches are closed such that all electrodes are connected to V_{sense}. Using a push button on the FPGA module, stimulation is initiated. The *Init* state sets the circuit up for the first stimulation pulse. States Ph1 (first phase), Iph (inter phase delay) and Ph2 (second phase) create a biphasic stimulation pulse by switching the right H-bridge switches and enabling the trigger signal. If charge balancing is disabled, the duration of Ph2 is set equal to Ph1. On the other hand, when charge balancing is enabled, the second phase is only half as long as the first phase. Next, the charge balancing method is performed using two states. In *CB_wait*, the system waits for a change in the output signal of the comparator. If the output is *LOW*, the trigger module is enabled for a short time in state *CB_pulse*. When the comparator output is *HIGH*, the system returns to *CB_wait* to wait for a change in the comparators output. If 30 µs pass without a change in $COMP_{CB}$, the system continues to the inter pulse (IP) state. If passive discharge is enabled, the electrodes are connected to V_{sense} in this state. Otherwise, all cathodic switches are open. Depending on the number of pulses and the number of channels, the system will go to *Ph1* for a new pulse or return to the *Idle* state if stimulation is done.

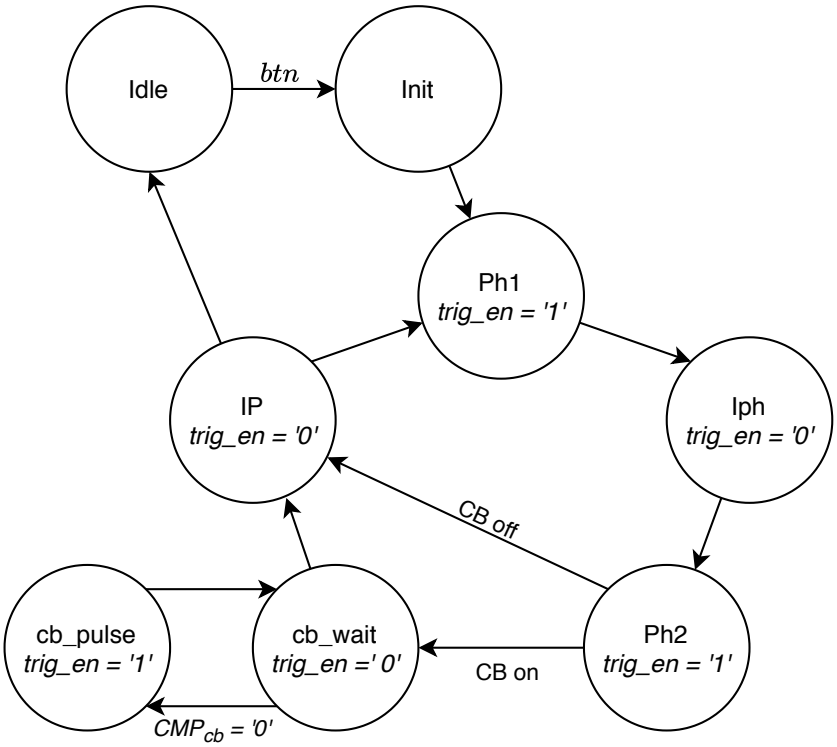

Figure 3.10: Finite State Machine (FSM) implemented on FPGA. Here, *trig_en* is the internal signal used to enable the trigger signal V_{trig}.

4

System Validation

Several steps have been taken to validate the designed system. First, the circuit was simulated using LTspice® circuit simulation software. Later, the designed PCB has been tested using both the linear tissue model as well as a micro-electrode probe submerged in phosphate-buffered saline (PBS) as load. As a last step of validation, power efficiency of the designed circuit was analysed.

4.1. Circuit Simulations

The final circuit design presented in Fig. 3.8 was simulated using LTspice software. The components in the circuit were implemented using spice models provided by their respective manufacturers. In all simulations, the linear ETI model was used to create a stimulation channel between El_0 and El_1. For this model, C_{dl} of 20 nF was used while R_{tis} ranged from 50 kΩ to 150 kΩ.

To verify correct operation of the circuit, a single stimulation pulse with a phase width of t_{ph}= 200 µs, an interphase delay of t_{iph}= 50 µs and stimulation intensity of Q_{ph}= 10 nC was simulated using a load of R_{tis}= 100 kΩ. The results are shown in Fig. 4.1, where $V_{load} = V_{El,0}$-$V_{El,1}$. It can be seen that V_{anodic} charges towards a negative voltage between UHF pulses during the second stimulation phase, which is needed for the charge balancing method. Moreover, the residual voltage of −40 mV at the end of the stimulation pulse indicates charge imbalance. For a perfect current mode stimulator, charge balancing is not required for linear loads because $Q_{ph1} = Q_{ph2}$. However, the residual voltage on C_{dl} indicates that $Q_{ph1} \neq Q_{ph2}$ for the proposed circuit. One cause for this imbalance is the charge error of the circuit due to non-idealities, as identified in Section 3.3.4. Voltage built up over C_{dl} slightly changes $I_{S1}(t)$ and thus the charge error of an UHF pulse changes as well. Due to this, the cumulative charge error made in the second phase is not equal to the error of the first phase, resulting in a charge imbalance. Another contribution to the imbalance is the discharge of C_{dl} in between stimulation pulses through Z_{pd}. Last, the simulation results show an expected overshoot of V_{sense} after crossing V_{ref}. For the first UHF pulse, the time delay is approximately 118 ns, resulting in a charge error of 15 pC. As explained above, this error is not constant as the voltage over C_{dl} changes.

Next, the charge injection accuracy of the circuit was assessed. The injected charge was measured for stimulation pulses programmed with intensity, Q_{ph}, ranging from 1 nC to 20 nC applied to tissue loads, R_{tis}, ranging from 50 kΩ to 150 kΩ. Measuring the injected charge is done by measuring the voltage across C_{dl} during the interphase delay, as $Q_{inj} = V_{Cdl}C_{dl}$. Figure 4.2 shows the absolute accuracy of the injected charge.

To characterize the absolute accuracy, Q_{inj} is compared to Q_{ph}, where $Q_{ph} = V_{ref}C_{sense}N$. As described in Chapter 3, the stimulation intensity is scaled using V_{ref}, while C_{sense}= 400 pF and $N = t_{ph}f_{sw}$= 40 for all measurements. The results in Fig. 4.2, show an offset and gain error. In Section 3.3.4, the main sources for this error were identified. A bigger I_{S1} for low tissue impedance results in a bigger error made by the circuit. Moreover, for a combination of high tissue impedance and Q_{ph}, it can be seen that Q_{inj} approaches $Q_{ph}/2$. The cause for this is shown in Fig. 4.3, depicting V_{sense} during the first UHF pulse for Q_{ph}= 20 nC and different values for R_{tis}. It can be seen that S_1 takes more than 5 µs for R_{tis}= 150 kΩ. Because of this, the control loop is not triggered for every trigger input, effectively reducing the number of UHF pulses to $N/2$. This effect determines an upper limit for the allowable

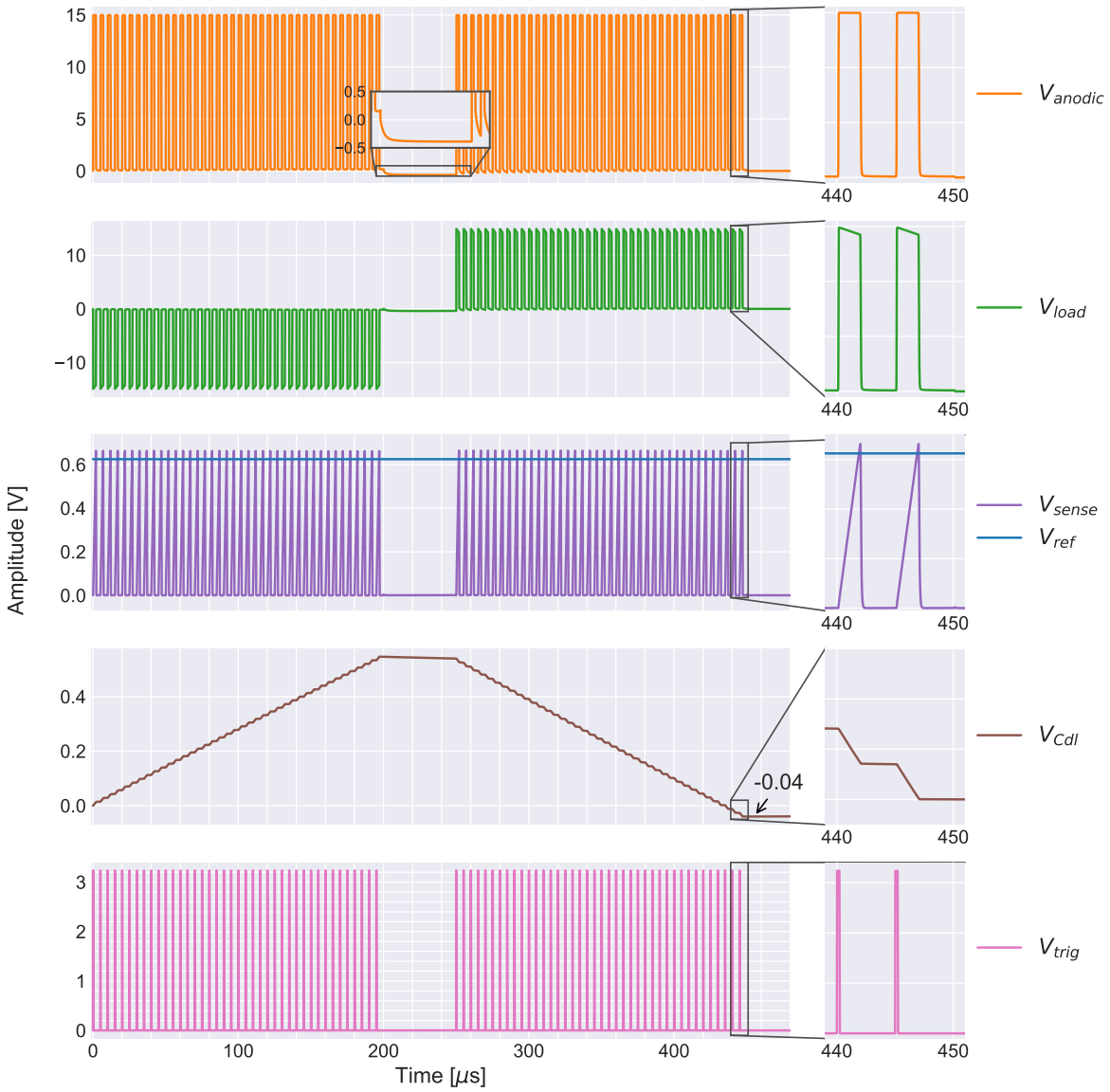

Figure 4.1: LTSpice® simulation using real components. Figure shows stimulation of a single stimulation pulse with t_{ph}= 200 µs and Q_{ph}= 10 nC to a linear tissue load with R_{tis}= 100 kΩ and C_{dl}= 20 nF.

tissue impedance for correct operation of the circuit. To allow higher impedance electrodes, V_{stim} has to be increased.

In Fig. 4.4, the relative charge injection accuracy is shown. Here, the relative accuracy is measured as the change in Q_{inj} for changing R_{tis}, normalized to the value of Q_{inj} at R_{tis}= 100 kΩ (referred to as Q_0 and R_0 in Fig. 4.4). The circuit was designed to have constant charge injection for changing load impedance, thus an ideal circuit implementation would result in a horizontal line. Additionally, the relative accuracy for UHF voltage stimulation with static duty cycle is depicted. The simulations show a clear improvement with respect to the static duty cycle implementation. Also, the simulation shows an improved accuracy when the stimulation intensity is increased, as it approaches the ideal line. However, when Q_{ph}= 20 nC and R_{tis}>120 kΩ the same error (effective $N = N/2$) as seen in the absolute accuracy plot becomes apparent.

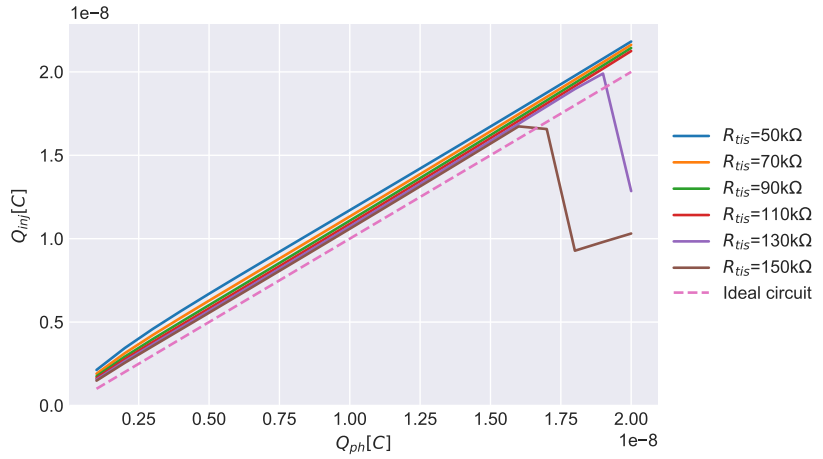

Figure 4.2: Simulated absolute accuracy of the injected charge for different tissue resistance values, Q_{ph} is the programmed charge and Q_{inj} is the measured injected charge. A step size of 1 nC was used for the simulations.

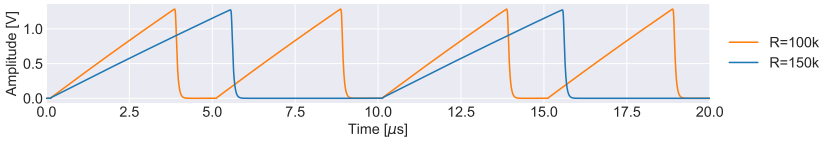

Figure 4.3: Signal V_{sense} for $Q_{ph} = 20nC$. When R_{tis}= 150 kΩ, the system can not be triggered at f_{sw}= 200 kHz, reducing the number of UHF pulses.

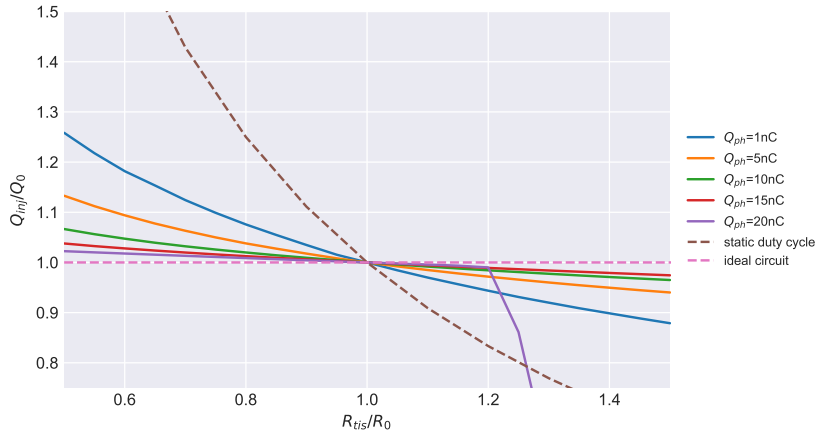

Figure 4.4: Simulated relative accuracy of the injected charge for different stimulation intensities. R_0= 100 kΩ and $Q_0 = Q_{inj}$ at R_0.

4.2. PCB Measurements Linear Tissue Model

The performance of the implemented PCB was assessed in a similar manner as the circuit simulations. For the measurements, a *GW Instek GPP-4323* power supply was used to generate supply voltages of ±15 V. The signals were measured on a *Tektronix 2014C* Oscilloscope and averaging of the signal to reduce noise was used when possible. In order to measure the voltage across C_{dl}, a *pico Technology ta045* differential probe was used. Moreover, a breadboard was used to connect the configuration pins to either 3.3 V or ground. A diagram of the setup for the linear model measurements is depicted in Fig. 4.5. For electrode measurements, the linear model is replaced with the electrode connections and the differential probe is not longer used.

Using the FPGA in single-channel mode, a stimulation channel between node El_3 and El_4 was created. The tissue load was modelled using a 20 nF capacitor in series with a variable resistor. A

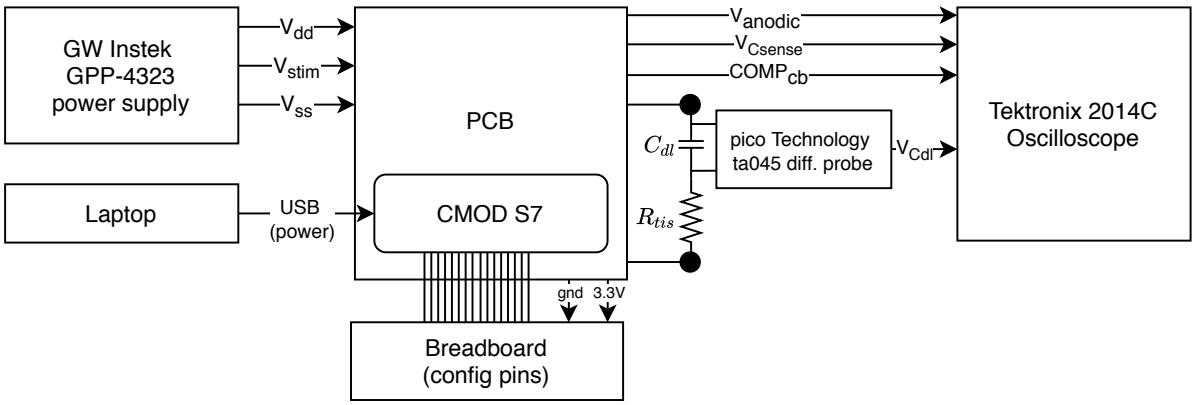

Figure 4.5: Block diagram of the test setup for measurements on the linear tissue model incorporating the PCB, power supply, differential probe and oscilloscope. A laptop is used to power the CMOD S7 module via USB and the configuration pins are set using a breadboard.

single stimulation pulse with t_{ph}= 200 µs, t_{iph}= 50 µs and Q_{ph}= 10 nC was applied to a load of R_{tis}= 100 kΩ. The resulting waveforms are depicted in Fig. 4.6. For this measurement, charge balancing was disabled. The measured waveforms are similar to the simulations, with a few differences worth noticing. First of all, a residual voltage of −132 mV is measured. This is more than simulations showed and emphasizes the need for active charge balancing in the implemented circuit. Moreover, a small voltage step (~50 mV) on V_{sense} can be noticed at the beginning of each UHF pulse, which is caused by channel cross-talk. To minimize this effect, El_3 and El_4 where chosen as output nodes as the traces on the PCB are far apart. Furthermore, the connections to the load are made as short as possible. Last, spikes can be observed in the voltage waveform of V_{Cdl}. To measure the voltage across C_{dl}, a differential probe with a built-in differential amplifier was used. In the second phase, C_{dl} is connected to V_{anodic} by the H-bridge. Thus, the voltage at both terminals of the capacitor switches rapidly between 0 and V_{stim}. Even though the amplifier has a high common mode rejection ration (CMRR) of −80 dB, the switching can be observed in the measured waveform. During the first phase, the capacitor is connected to V_{sense} and thus the probed nodes do not switch as much.

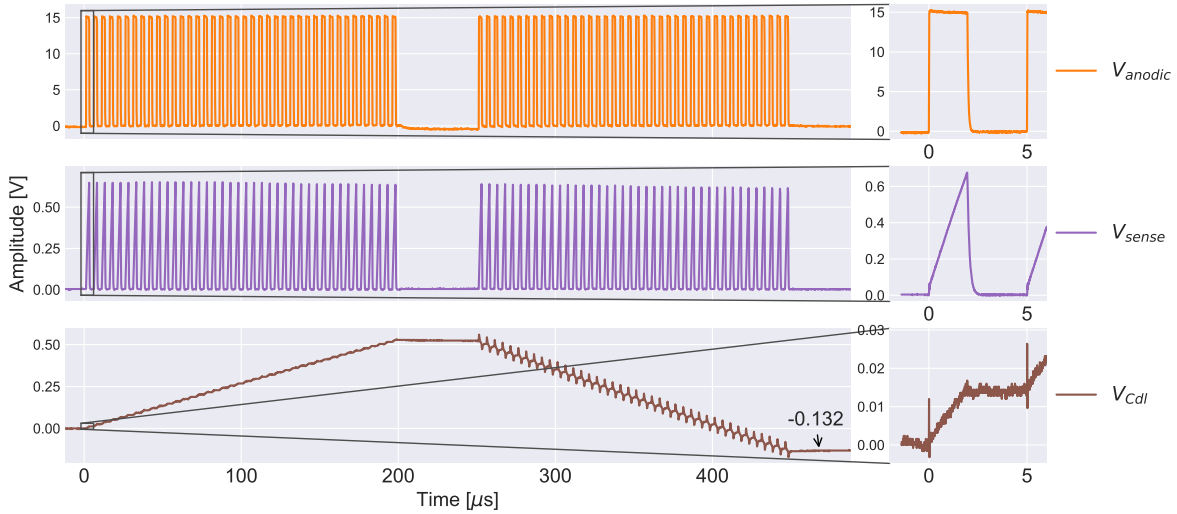

Figure 4.6: Stimulation pulse generated by the prototype PCB. Stimulation parameters: t_{ph}= 200 µs, t_{iph}= 50 µs, Q_{ph}= 10 nC and CB disabled. Load: R_{tis}= 100 kΩ between El_3 and El_4.

The measured absolute and relative accuracy of the implemented circuit are depicted in Figs. 4.7a and 4.7b respectively. For the absolute accuracy, it can be observed that the limitation for high-impedance loads start at a lower value of Q_{ph} compared to the simulation results. Parasitic capacitance added by the PCB trace at node V_{sense} increase the effective value of C_{sense}. This increases the charge

error made by the circuit and effectively increases the width of UHF pulses. This effect limits the charge injection capability of the implemented circuit. The relative accuracy plot shows a noticeable increase in charge error for low values of Q_{ph}. To stimulate with an intensity of Q_{ph}= 1 nC, V_{ref} is set to 62.5 mV. The voltage step on V_{sense}, as noticed in Fig. 4.6, is in the same order of magnitude. Therefore, the UHF pulse width for this intensity is dominated by delay time of the control loop and the width of the trigger pulse. Due to this, the dynamic duty cycle control has no effect and the relative accuracy approaches the static duty cycle line.

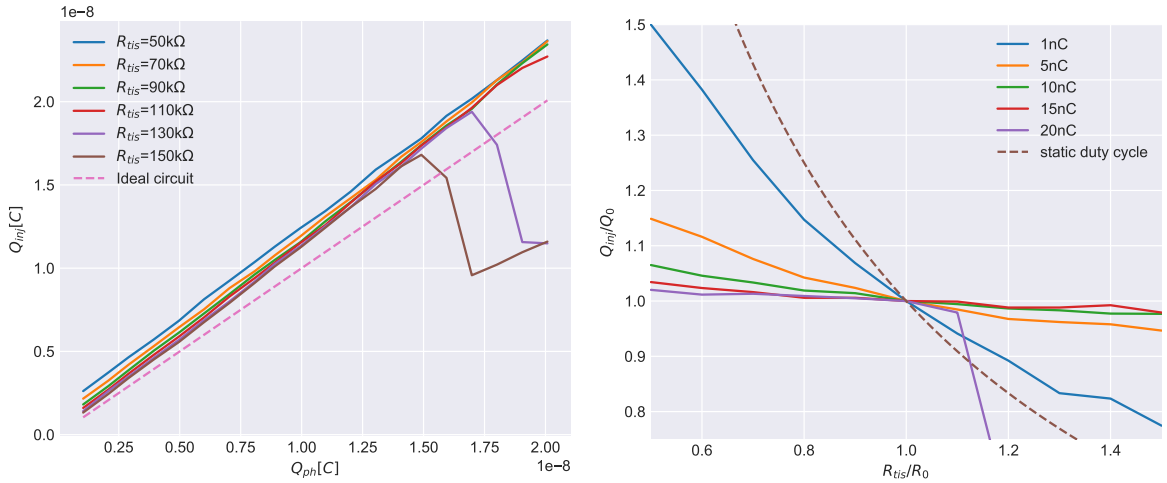

(a) (b)

Figure 4.7: Measured charge injection accuracy of the implemented PCB. (a) Absolute accuracy, measured injected charge Q_{inj} versus programmed stimulation intensity Q_{ph} for different values of R_{tis}, (b) Relative accuracy of Q_{inj} for change in R_{tis}, measured for different values of Q_{ph}. The relative accuracy is normalized to the measured value at R_{tis}= 100 kΩ.

To verify the implementation of active charge balancing, a single stimulation pulse with charge balancing enabled and disabled are compared in Fig. 4.8. Up until t= 350 µs, the waveforms are identical. After 350 µs, the output of $COMP_{CB}$ is used to regulate the UHF pulses. As stated before, different definitions for the required accuracy of charge balancing are used in literature [74]. In terms of residual voltage, a safety limit of $\pm$50 mV [69] or $\pm$100 mV [70] is often considered. The figure shows that the implemented charge balancing method successfully reduces the residual voltage on C_{dl} well within that safety limit.

To show the importance of an active charge balancing circuit, the voltage over C_{dl} is measured over multiple stimulation pulses in Fig. 4.9. The measurement shows a rapid build up of voltage offset when neither active nor passive charge balancing is used. Moreover, it can be seen that the passive discharge time is long relative to the stimulation pulse. The time in between stimulation pulses is used to stimulate parallel channels in multi-channel mode and thus there is no time to passively discharge the interface. Last, with active charge balancing turned on, the residual voltage is quickly returned within the safety limit after each stimulation pulse.

The stimulation source is designed to stimulate multiple channels in an interleaved manner. With the implemented PCB, up to four channels can be stimulated. Figure 4.10 illustrates the multi channel operation with a measurement of two stimulation pulses applied to four different stimulation channels. For this measurement, the multi-channel FSM was used with charge balancing enabled. The channels have different stimulation parameters as can be seen by comparing the phase widths. The measurement shows that the circuit is capable of interleaved stimulation. Up to ten stimulation channels with comparable stimulation parameters could be stimulated using a single stimulation source.

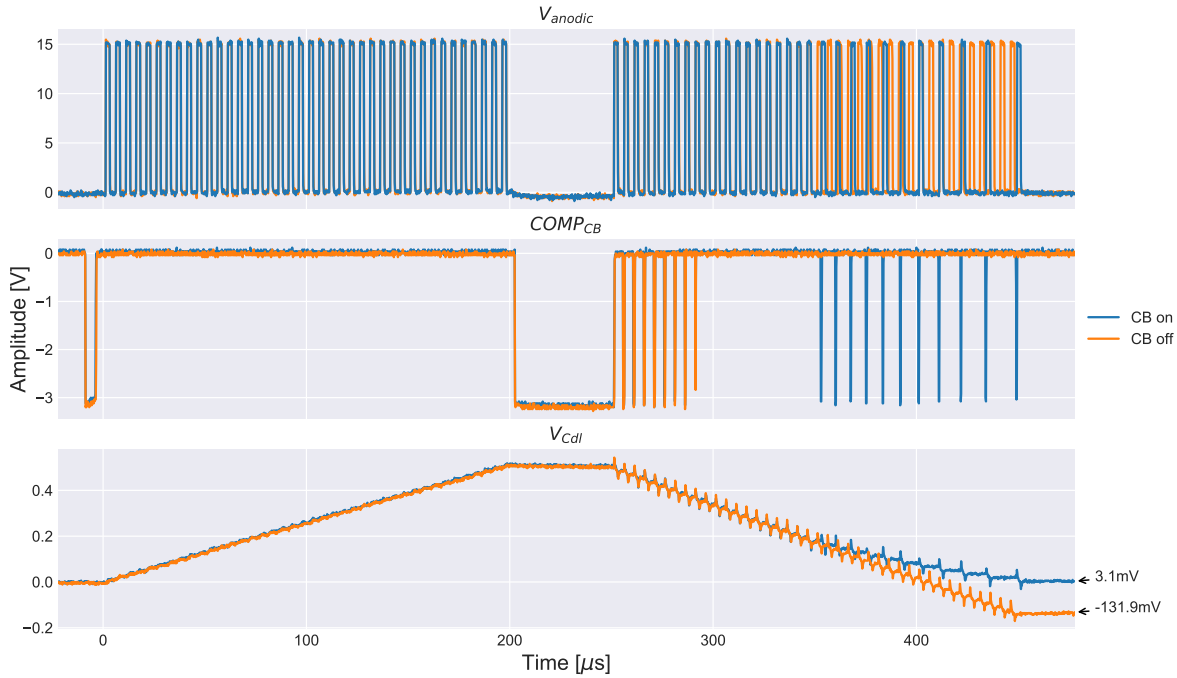

Figure 4.8: Stimulation signal with and without active charge balancing. The effect of charge balancing can be seen from t= 350 µs onward. With charge balancing enabled, the V_{cdl} is successfully returned close to 0 V.

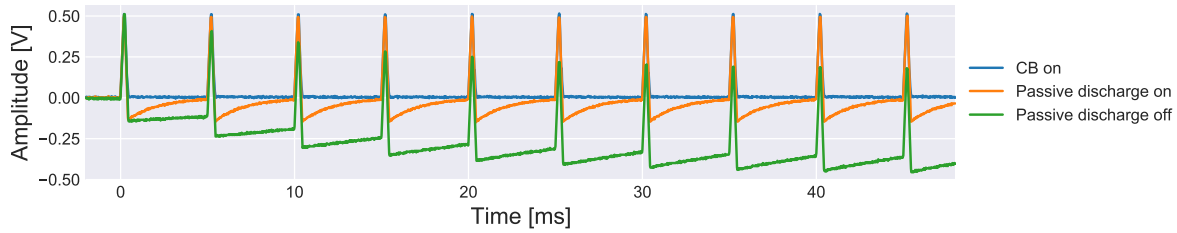

Figure 4.9: Voltage across C_{dl} over multiple stimulation pulses, comparing the effects of active charge balancing and passive discharge on the residual voltage.

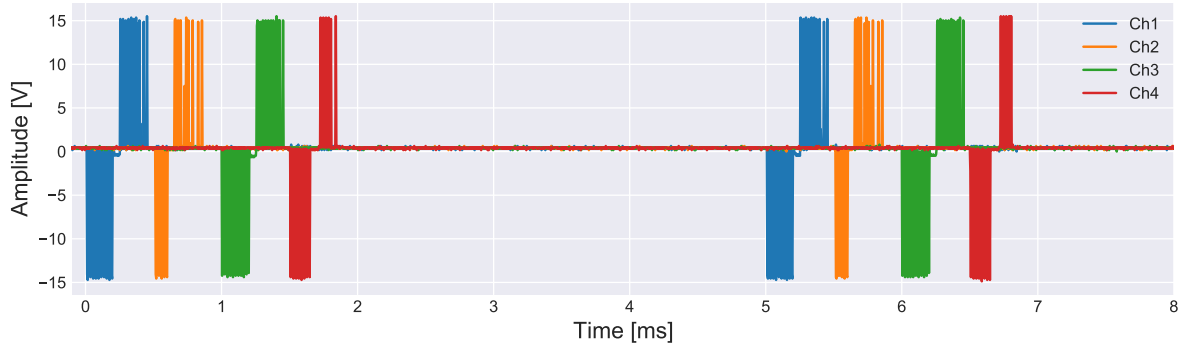

Figure 4.10: 4-channel stimulation measurement for two consecutive stimulation pulses, showing the interleaved stimulation pattern. t_{ph} and V_{ref} can be configured independently for each stimulation channel.

4.3. PCB Measurements *in Vitro*

To verify the circuit operation for non-linear ETI impedance, some *in vitro* measurements are conducted. For these measurements, a *NeuroNexus a1x32-5mm-25-177 Electrode Array*, shown in Fig. 4.11, is used. The array consists of 32 circular Iridium electrodes with a diameter of 15 µm [75]. A stimula-

tion channel is created by connecting two electrodes to El_2 and El_7 of the PCB. The electrode array is submerged in a 1x Phosphate Buffered Saline (PBS) solution to model a tissue environment. The impedance characteristics of the used electrodes is unknown. However, an approximation of the electrode parameters can be deducted from the measured waveforms. Based on the measurement results it is expected that the impedance of the electrodes is much higher than 150 kΩ. This results in a limited performance of the PCB on the used electrodes, which is supported by the limitations found for the linear model.

Figure 4.11: NeuroNexus a1x32-5mm-25-177 Electrode Array used for *in vitro* measurements of the prototype PCB.

In Fig. 4.12, the measured waveforms for a stimulation pulse of t_{ph}= 200 µs and Q_{ph}= 5 nC are shown. From the measurement, it can be seen that the PCB successfully applies an UHF pulsed stimulation pulse to the electrodes. Using the slope on V_{sense}, R_{tis} is approximated to be 600 kΩ. This is much higher than the anticipated impedance, therefore the charge injection capability of the stimulator is limited for these electrodes. This can be observed on V_{anodic} as well: A stimulation pulse of Q_{ph}= 5 nC on the electrodes requires an UHF pulse of ~3 µs, as opposed to ~2 µs for Q_{ph}= 10 nC when R_{tis} is 100 kΩ (Fig. 4.6). Furthermore, the voltage measured at V_{anodic} during the interphase delay can be used as approximation for V_{Cdl}. In the electrode measurement, V_{Cdl} ≈893 mV after a pulse of 5 nC, while V_{Cdl} ≈518 mV for a stimulation pulse of 10 nC on the linear tissue model. This indicates that the voltage build up on C_{dl} is bigger than expected, which also limits the performance of the circuit. Another noticeable result in the measured waveform is the initial step in V_{sense}. As explained before, this step is caused by cross-talk between the stimulation electrodes. For the measurements on the linear model, connections were kept as short as possible to minimize this effect. In Fig. 4.11, it can be seen that the traces between the connector and the electrode are routed close to each other. Because of this, cross-talk has increased for the electrode measurements.

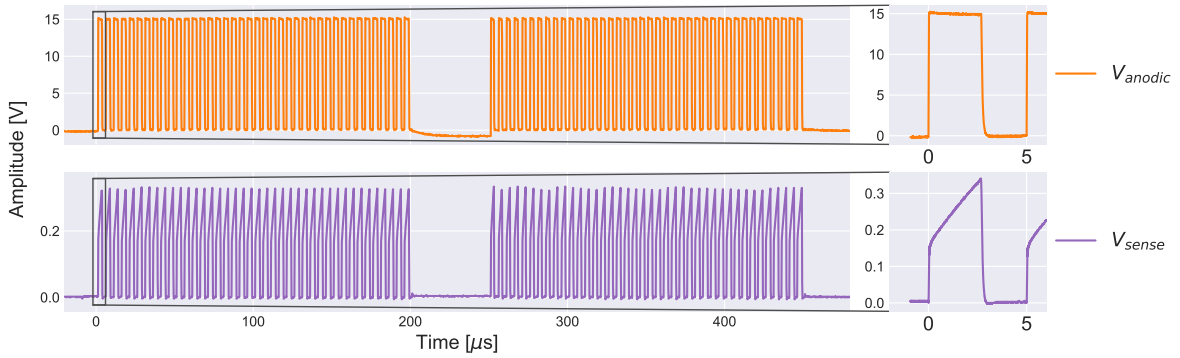

Figure 4.12: Measured waveforms for a stimulation pulse of t_{ph}= 200 µs and Q_{ph}= 5 nC applied to two electrodes of the NeuroNexus electrode array.

To illustrate the consequences of the high electrode impedance and cross-talk, V_{sense} for the first UHF pulse for different values of Q_{ph} is depicted in Fig. 4.13. This measurement shows that the duration of the pulses is affected by the initial voltage step on C_{dl}. It should be noted that the step is equal for different stimulation intensities and tissue impedance, therefore the system can be calibrated to cancel out the error. Also, it can be seen that the duration of the UHF pulse for Q_{ph}= 10 nC takes more than 5 µs, which will cause a charge injection error as has been shown in previous measurements and simulations. Apart from this, the pulses and scaling of the stimulation intensity behaves as expected.

Because there is no physical node between C_{dl} and R_{tis}, it is impossible to directly measure V_{Cdl} on the electrodes. As a result, the accuracy of the charge balancing method can not be measured *in vitro*.

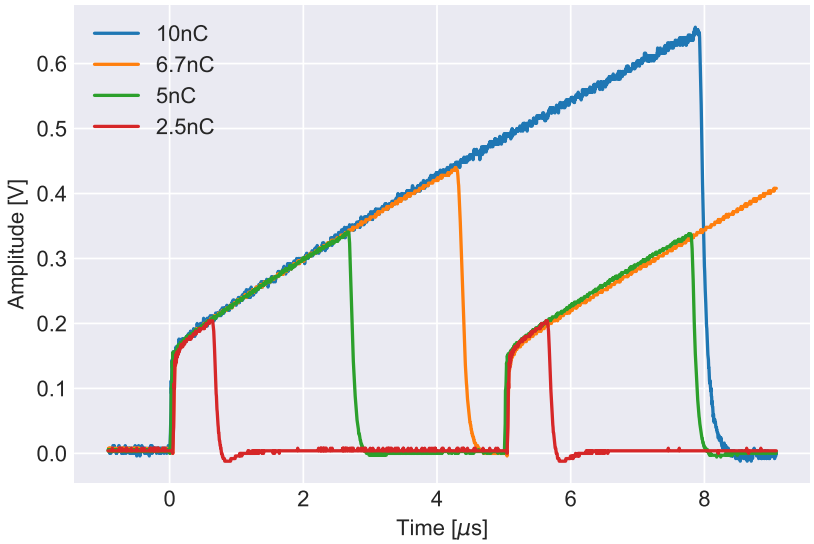

Figure 4.13: V_{sense} measured on the electrodes for the first UHF pulse in a stimulation pulse of t_{ph}= 200 µs and different values of Q_{ph}.

Nevertheless, the operation of the charge balancing method is demonstrated with a measurement of V_{load} for a single stimulation pulse with charge balancing enabled in Figure 4.14. For this measurement, the waiting time of CB_{wait} was increased, as the original delay was not enough for the high impedance electrodes. As can be seen, the second phase starts with 100 µs of normal stimulation pulses. The first charge balancing pulse follows after approximately 130 µs, which is much longer than for the linear model measurements. The cause of the longer inter pulse time is twofold. First of all, from previous measurements it has been established that the impedance of the electrodes is high. In the FSM-state CB_{wait}, the voltage at V_{anodic} discharges towards V_{Cdl} with a time constant proportional to R_{tis}, C_{dl} and C_p. Thus, high impedance electrodes cause an increase in the waiting time of the charge balancing method. Second, due to tissue non-linearity, it is expected that the residual voltage at t= 350 µs is already small. The waiting time of the charge balancing method becomes longer if the residual voltage is small. To demonstrate this, charge balancing is started immediately after the interphase delay in the measurement shown in Fig. 4.15. It can be seen that for the first pulses, when V_{Cdl} is still high, the delay between CB pulses is relatively short. As the residual voltage decreases with each UHF pulse, the delay between CB pulses increases.

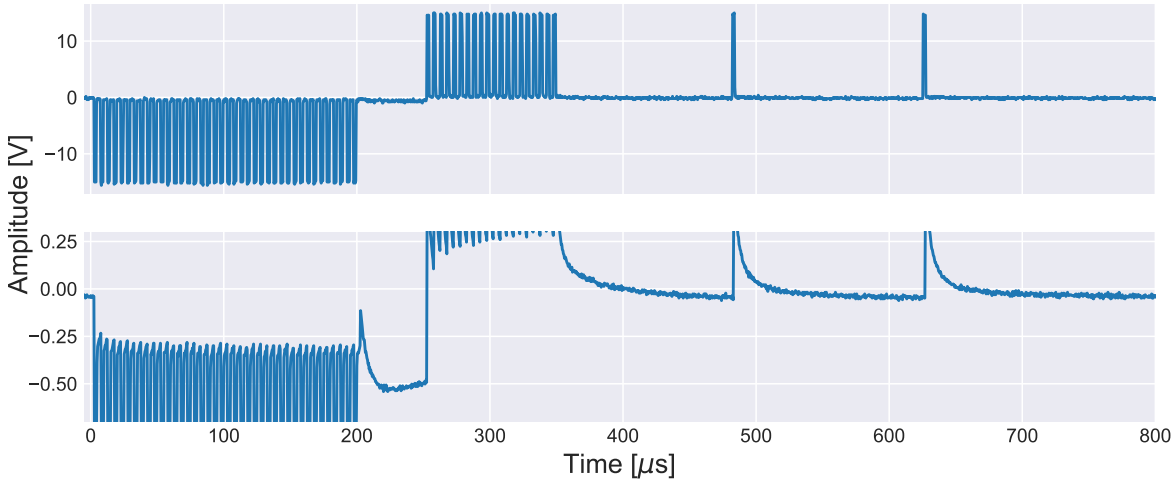

Figure 4.14: V_{load} measured for a stimulation pulse on electrode array with charge balancing enabled. Bottom plot shows a zoom of the signal around V=0. When V_{load}<0, a new UHF pulse is applied.

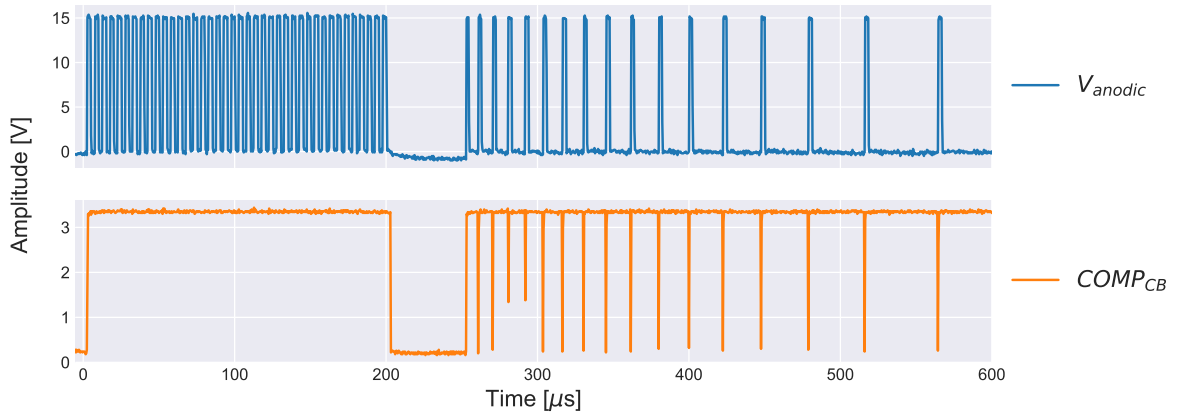

Figure 4.15: V_{anodic} and $COMP_{CB}$ for stimulation pulse on electrodes with charge balancing enabled directly after the interphase delay.

4.4. Power Efficiency Analysis

Power efficiency was one of the reasons to implement the UHF voltage stimulation method. An ideal implementation of the method could reach a theoretical power efficiency of 100% as was explained in Chapter 2. However, the real implementation of the circuit suffers from energy losses mainly caused by switching effects. To analyse the power efficiency of the implemented circuit, power losses are divided in resistive losses and capacitive losses. Generally, it is assumed that losses in the electrode capacitance are negligible compared to the resisitive losses [26]. Therefore, tissue is modeled by a resistor, R_{tis}, for the efficiency calculations. Furthermore, losses of the switches are assumed mainly to be caused by the on-resistance R_{on} and charging of the gate capacitance C_{gate}. Considering the switches in the signal path, the resistive efficiency is calculated using (4.1).

$$\eta_R = \frac{R_{tis}}{R_{tis} + R_{on,SW_{mod}} + R_{on,SW_{cat}} + R_{on,SW_{an}}} \tag{4.1}$$

The capacitive losses in the circuit are mainly caused by switching C_{gate} of SW_{mod} and SW_{dis}, the parasitic capacitance C_p at V_{anodic} and the sensing capacitor C_{sense}. The power consumption of charging and discharging a capacitor C to a voltage V at a frequency f_{sw} is calculated using (4.3). In the circuit, C_p and C_{gate} are charged to V_{stim} for each UHF pulse, while C_{sense} is charged to V_{ref}. Furthermore, the average power delivered to the tissue can be calculated using (4.2), where I_{S1} is the stimulation current described by (3.3), T_{S1} is state duration described by (3.5) and T is the UHF period ($\frac{1}{f_{sw}}$). The capacitive efficiency of the circuit is calculated using (4.4). Finally, by combining (4.1) and (4.4), the total efficiency of the circuit is calculated with (4.5).

$$P_{out,avg} = \frac{R_{tis}}{T}\int_0^{T_{S1}} I_{S1}^2(t)dt = Q_{UHF} f_{sw}(V_{stim} - \frac{V_{ref}}{2}) \tag{4.2}$$

$$P_C = CV^2 f_{sw} \tag{4.3}$$

$$\eta_C = \frac{P_{out,avg}}{P_{out,avg} + P_{Cgate} + P_{Csense} + P_{Cp}} = \frac{Q_{UHF}(V_{stim} - \frac{V_{ref}}{2})}{Q_{UHF}(V_{stim} - \frac{V_{ref}}{2}) + V_{stim}^2(C_p + C_{gate})} \tag{4.4}$$

$$\eta = \eta_R \eta_C \tag{4.5}$$

In IC technology, switch transistors can be scaled with factor *M* to change the parasitic parameters. For a High Voltage (20 V) transistor in AMS 0.18 µm technology, typical values are: R_{on}= 1.416 kΩ/M and C_{gate}=M111 fF [55]. Scaling of the switches is a trade-off between η_R and η_C. Because of the high load impedance in this application, the power efficiency does not suffer a lot from high R_{on} (see (4.1)). On the other hand, M should be as small as possible to minimize switching losses of C_{gate}. Thus, a scaling factor of M=1 was chosen for the calculations. The power efficiency is calculated for Q_{UHF} in the

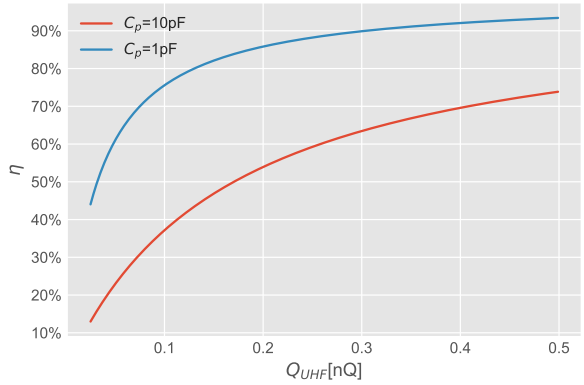

Figure 4.16: Calculated total power efficiency of the designed circuit for different values of C_p and R_{tis} = 100 kΩ.

range of 25 pC to 500 pC, which corresponds to Q_{ph}= 1 nC–20 nC for a stimulation pulse of t_{ph}= 200 µs and f_{sw}= 200 kHz. Figure 4.16 shows the calculated total efficiency for two different values of C_p. The figure shows a decline in power efficiency for low values of Q_{UHF}. The reason for this is that $P_{out,avg}$ scales with Q_{UHF}, while the switching losses of C_{gate} do not change at all. Moreover, the difference in the two lines shows that the efficiency suffers a lot from switching node V_{anodic}. Clearly, this node requires careful layout design to minimize the parasitic capacitance. Additionally, from (4.3) and (4.4) it can be seen that the power efficiency could be improved by scaling down V_{stim}.

As a comparison, the power efficiency for a conventional current mode stimulator (CMS) can be calculated using (4.6), where V_{load}=$I_{stim}R_{tis}$. In Fig. 4.17, CMS and the implemented circuit are compared with the following assumptions: V_{stim}=V_{supply}, Q=Q_{UHF}, T=$\frac{1}{f_{sw}}$ and C_P= 10 pF. This comparison shows that power efficiency of the proposed method is less susceptible to changes in R_{tis} than power efficiency of CMS. Moreover, the power efficiency of CMS exceeds the efficiency of the proposed method only when both R_{tis} and Q are high. In practice, both values will vary between channels and over time.

$$\eta_{CMS} = \frac{I_{stim}^2 R_{tis}}{I_{stim} V_{supply}} = \frac{Q}{t}\frac{R_{tis}}{V_{supply}} = \frac{V_{load}}{V_{supply}} \tag{4.6}$$

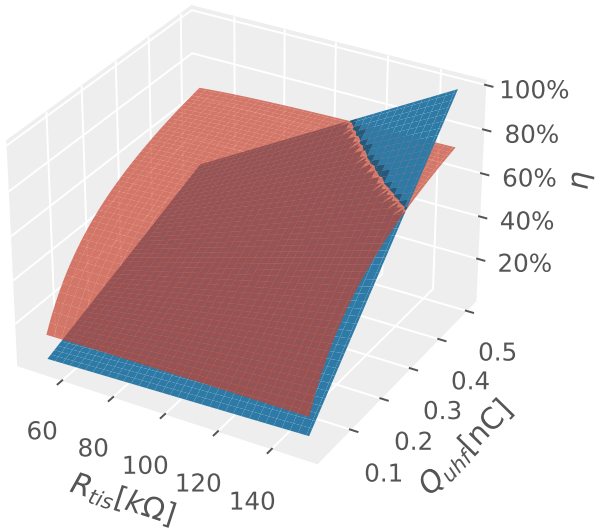

Figure 4.17: Power efficiency of (red) the proposed circuit compared to (blue) conventional CMS for different load impedance R_{tis} and charge Q_{UHF}.

Up until now, power efficiency $\eta = \frac{P_{out}}{P_{in}}$ is considered, where P_{out} is the power delivered to the tissue and P_{in} is the total power delivered by the supply. From Fig. 4.17, it can be seen that the proposed method outperforms CMS in this respect. However, the generated stimulation waveform, and thus P_{out}, is different for both methods. For fair comparison, this effect should be taken into account. This is done by calculating the average input power required to apply the same amount of charge for both methods. The average output power for the proposed method is already calculated in (4.2). For CMS, the required power for delivering Q_{UHF} in a time period T is calculated with (4.7).

$$P_{out,CMS} = (\frac{Q_{UHF}}{T})^2 R_{tis} = \frac{I_{stim} R_{tis} Q_{UHF}}{T} = V_{load} Q_{UHF} f_{sw} \tag{4.7}$$

Combining (4.2), (4.6) and (4.7) with the fact that $V_{ref} \ll V_{stim}$, gives (4.8). Finally, the average input power of both methods is compared using (4.9), (4.10) and (4.11). Given that η_{UHF}<1, this result shows that UHF stimulation appears to be fundamentally more power consuming than CMS under the stated assumptions.

$$P_{out,UHF} = P_{out,CMS} \frac{V_{stim} - \frac{V_{ref}}{2}}{V_{load}} \approx \frac{P_{out,CMS}}{\eta_{CMS}} \tag{4.8}$$

$$P_{in,UHF} = \frac{P_{out,UHF}}{\eta_{UHF}} \approx \frac{P_{out,CMS}}{\eta_{UHF}\eta_{CMS}} \tag{4.9}$$

$$P_{in,CMS} = \frac{P_{out,CMS}}{\eta_{CMS}} \tag{4.10}$$

$$P_{in,UHF} \approx \frac{P_{in,CMS}}{\eta_{UHF}} \tag{4.11}$$

5

Discussion & Conclusion

5.1. Discussion

Throughout this thesis, the main research question was *"How can stimulation pulses be delivered to multiple intracortical microelectrodes in a safe and efficient manner to effectively evoke phosphenes?"* From existing literature, stimulation parameters to effectively evoke phosphenes and typical characteristics of intracortical microelectrodes were extracted. One thing that was found to be primarily important for stimulation efficacy and safety was charge control. During stimulation, enough charge should be injected to initiate cell activation, while too much charge should be avoided as it could cause damage to electrodes and tissue. After a stimulation pulse, the residual voltage at the electrode tissue interface should be minimal to prevent charge building up over repeated stimulation as that can lead to tissue and electrode damage. Furthermore, it was found that current mode stimulation, using rectangular current pulses, is widely used because of the precise charge control it offers. However, especially in multi-channel stimulation, this conventional method is inefficient because of power dissipated in the current source. On the other hand, voltage mode stimulation has better power efficiency performance but lacks control over the injected charge. Therefore, the goal of the thesis was to design a multi-channel stimulation source that is effective, safe and efficient. It was hypothesized that UHF voltage stimulation combined with charge control and active charge balancing could provide effective, safe and efficient multi-channel stimulation.

5.1.1. Charge Control of the Implemented Design

A novel charge control circuit was implemented to dynamically scale the duty cycle of UHF pulses. Measurements on a linear tissue model have shown successful control of the injected charge during stimulation. However, some limitations were found. First of all, charge monitoring errors limit the accuracy of the injected charge. Four sources of error have been identified that affect the accuracy of charge monitoring: a time delay introduced in the multivibrator control loop, parasitic capacitance at V_{anodic} & V_{sense}, switching artifacts of switch SW_{dis} and cross-talk between traces. The time delay of the control loop is not constant making it impossible to calibrate the system for this error. Hence, f_{sw} should be chosen such that the delay is small compared to the duration of a single UHF pulse to minimize this error. Contrarily, to reduce size of C_{sense} for area reduction of the circuit, f_{sw} could be increased. Thus, the time delay of the control loop inhibits scalability of the design because of the limitation on f_{sw}. The parasitic capacitance parallel to C_{sense} adds a gain error to the monitored charge. Absolute accuracy of the injected charge is not very important as the stimulation intensity will be set using a threshold procedure. Therefore, the accuracy of C_{sense} is not critical in the presented design and the effect of the parasitic capacitance is calibrated out of the system during the threshold procedure. The other error sources introduce an offset error of the injected charge. The measurements in Fig. 4.7b suggest that this error affects the relative accuracy of pulses with low stimulation intensity. However, the charge error is constant over impedance and intensity changes and could thus be compensated for. Compensation could be implemented by increasing V_{ref} or with techniques counteracting charge injection. Second, a clear limitation has been found for high impedance tissue loads. The system is designed to inject 1 nC–20 nC during a stimulation phase of t_{ph}= 200 µs on tissue loads of R_{tis}= 50 kΩ–150 kΩ. Due

to the implemented control loop, the duty cycle of UHF pulses will increase for increasing stimulation intensity and/or tissue impedance. A combination of both can lead to the situation that $T_{S1} > \frac{1}{f_{sw}}$. When that happens, the circuit is not triggered at f_{sw} anymore and the injected charge is limited. The measurement in Fig. 4.7a clearly shows this limitation for a tissue resistance of 130 kΩ and 150 kΩ. Since the tissue resistance is not adjustable, this limitation can only be omitted by increasing V_{stim}. It is important to notice that this limitation will always cause less charge to be injected and thus will never lead to harmful stimulation. In practice, tissue impedance is unknown and it would be valuable to detect this limitation in the circuit. A possible implementation for this could be the detection of a trigger pulse while signal Q is still high. Last, errors in charge monitoring inherently lead to charge imbalance. The error in the monitored charge is dependent on the current of the UHF pulses (I_{S1})). Due to the charge accumulation at C_{dl}, the voltage on R_{tis} decreases during the first phase, while in the second phase the polarity is reversed and thus V_{Cdl} increases the voltage on R_{tis}. Because of this, I_{S1} changes and the charge error in the first phase is not equal to the error of the second phase. Therefore, a stimulation pulse will lead to charge imbalance even when a linear tissue model is used. This effect was found in simulations as well as in the testing of the implemented PCB. This error emphasizes the need of the active charge balancing method implemented in the system design.

5.1.2. Implemented Active Charge Balancing Method

The implemented active charge balancing method is simple, requiring only a single comparator. With measurements on the linear tissue model, effectiveness of this method has been validated as the residual voltage on C_{dl} was brought back to 3.1 mV. Furthermore, the importance of charge balancing has been shown in Fig. 4.9 by comparing V_{Cdl} over multiple stimulation pulses with and without charge balancing. It can be observed that the voltage at the interface gradually builds up when no charge balancing is used. When only passive charge balancing is used, it takes a long time to bring the residual voltage back to zero. Finally, with the active charge balancing method enabled, the residual voltage is brought back within the safety window immediately and stays constant in between stimulation pulses. For the *in vitro* measurements, the voltage on C_{dl} could not be measured to validate the accuracy of active charge balancing. Nevertheless, the measurement presented in Fig. 4.15 shows that the circuit is able to detect residual voltage on the non-linear electrode. Moreover, the charge balance measurement on the electrode shows how the wait time of this method is affected by the impedance of the electrode. If the impedance becomes too high, this might lead to limited performance of the charge balancing method. To fully verify this method, more measurements using electrodes with lower impedance should be conducted.

5.1.3. Power Efficiency of the Implemented Design

In order to stimulate as many channels as possible with the limited power available for the implanted neurostimulator, multiple measures have been taken into account in the proposed design.

The first way to minimize instantaneous power consumption of the circuit is the implementation of spatio-temporal stimulation. The waveforms typically used in the application of intracortical visual stimulation allow for interleaving of the channels. By interleaving, the stimulator circuit can be shared among multiple channels. Not only does this save valuable chip area but it also relaxes the power requirements of the system. The interleaved stimulation method has been validated on four channels using the prototype PCB in Fig. 4.10. Second, the UHF voltage stimulation method was chosen to improve power efficiency. In the power efficiency analysis it has been shown that the proposed circuit has improved power efficiency for most of the stimulation parameters when compared to conventional CMS. However, it was also shown that the required input power has not decreased with the efficiency improvement under the current assumptions. Instead, power dissipation in the load has increased due to the new waveform shape. This analysis shows that comparison of the proposed stimulation method and CMS with respect to power efficiency is not straightforward. One of the assumptions in this analysis and throughout this thesis is that the required charge to initiate cell activation Q_{th}, is equal for both stimulation methods. However, there is evidence that the strength duration curve parameters are dependent on the used stimulation waveform [76]. Analytical studies with neuron models have indicated that a rectangular stimulus waveform is not energy-optimal in some cases [76] and that other waveforms might require less energy to activate neurons. To truly compare the proposed UHF stimulation method with conventional CMS, an analysis comparable to [76] should be done for the UHF waveform with

stimulation parameters of intracortical stimulation. With this analysis, the effect of scaling f_{sw} to cell activation and energy efficiency could also be researched.

5.1.4. Stimulation Parameters & Electrode Characteristics

Measurements have shown that performance of the designed circuit is limited for the extreme cases of the set requirements for the system. The requirements for stimulation intensity and load impedance were determined based on existing literature. However, reported values of both parameters are very inconsistent. Some literature suggest phosphene thresholds at 25 µA (5 nC)[13], while currents up to 100 µA (20 nC) are used in other studies [37]. Also, for intracortical micro-electrodes a wide range of electrical properties is reported. The impedance of an electrode depends, among other things, on its geometry and material type. The wide range for both parameters has led to the design of a system with high dynamic range. If the electrodes that will be used with the stimulator are characterized properly and more physiological research leads to a better understanding of phosphene thresholds, the performance of the circuit could be improved. If the range of values can be narrowed down, a lower stimulation voltage could be used. It has already been shown that this will also lead to better power efficiency. On the other hand, if more research confirms that a wide range of parameters should be used, the circuit could be improved for better performance at extreme values.

5.1.5. Electrode Configuration

The implemented circuit is only capable of bipolar stimulation, while monopolar stimulation is commonly used to research the potential of intracortical visual stimulation. While deciding the location of the sensing capacitor for this design, it has been established that the proposed charge control loop suffers a lot from switching artifacts when the sensing capacitor is placed at the same side of the tissue as the modulation switch. For this reason, the sensing capacitor was placed between the return electrode and ground. In order to be able to access the return electrode, bipolar stimulation has to be used. With monopolar stimulation, the return electrode is located far from the stimulation site and is shared among channels. In that case, this electrode can not be accessed to sense the charge of a single stimulation channel. The implementation of a bipolar stimulator has multiple advantages for circuit design. Moreover, it is expected that bipolar will have to be used in a system incorporating 1000 channels, as monopolar stimulation leads to cross-talk in multi-channel stimulation. However, it is unknown what effect the change from mono- to bipolar has on the required stimulation parameters. The electric field in bipolar stimulation is more localized, which might lead to a decrease in phosphene threshold. Physiological research is needed to compare the electrode configurations and to establish stimulation parameters for bipolar intracortical stimulation.

5.2. Conclusion and Contributions

The development of a intracortical visual prosthesis requires an implantable neurostimulator that is able to stimulate more than 1000 micro-electrodes. It is important that the device can stimulate neurons in an effective, safe and efficient manner. For stimulation efficacy and safety, control over the injected charge during stimulation is particularly important. Moreover, at the end of a stimulation pulse the residual charge should be small to prevent harmful conditions for both the electrodes and tissue. Conventional stimulation methods have disadvantages for this application because current mode stimulation is inefficient in multi-channel configuration and voltage mode stimulation lacks control over the injected charge.

In this thesis, a novel stimulation method has been introduced: charge controlled UHF voltage stimulation. Ultra high frequency voltage stimulation was chosen based on the multi-channel efficiency of this method. However, the method lacks control over the injected charge when a static duty cycle is used. Therefore, a charge controller was added to the method to improve efficacy and safety. The novel charge control scheme uses a mono-stable multivibrator implementation to dynamically control the duty cycle of the UHF pulses. Moreover, the chosen stimulation method allows for preventive active charge balancing in the second stimulation phase. This was implemented using a single comparator, that detects a zero-crossing of the double layer voltage in between UHF pulses. The proposed design was implemented on a printed circuit board (PCB) for validation.

Measurements of the PCB using a linear tissue model as well as micro-electrodes have shown correct operation of the proposed design. It has been shown that the novel implementation successfully

controls the injected charge of a stimulation pulse for varying tissue impedance. Using a switching frequency of 200 kHz, a sensing capacitor of 400 pF and a reference voltage between 62.5 mV and 1.25 V, the prototype was able to stimulate with an intensity of 1 nC to 20 nC over a period of 200 µs. The PCB implementation has high flexibility in stimulation parameters which is beneficial for future experiments.

Importance of an active charge balancing scheme was shown by measuring the residual charge on the double layer capacitor in the linear tissue model. Without any form of charge balancing, repetitive stimulation led to a rapid build up of an offset voltage on the capacitor. Furthermore, passive discharging was not sufficient as the discharge time was long compared to the stimulation pulse. With the use of the proposed active charge balancing scheme, the residual voltage was brought back well within the safety window of $\pm$50 mV at the end of a stimulation pulse. This result is promising because it improves safety of the stimulation signal.

To facilitate multi-channel stimulation, the stimulator circuit is shared between channels in a interleaved manner. The operation of this method was demonstrated on the prototype as well. Between eight output pins, multiple output channels can be created. For validation purposes, four channels were created using linear tissue models. The prototype was able to stimulate each channel with channel specific stimulation parameters.

Last, power efficiency of the implemented design was evaluated. It has been shown that the implemented design has better power efficiency than conventional current mode stimulation over a large range of stimulation parameters and tissue impedance. However, the analysis also revealed the importance of energy efficient stimulation waveforms. Future research should make the comparison of the stimulation methods complete.

In conclusion, the presented design is able to create safe and effective multi-channel stimulation pulses in an efficient manner. The work in this thesis contribute to the development of implantable multi-channel neurostimulators for intracortical stimulation.

5.3. Recommendations for Future Work

- **Electrode and stimulation parameters -** With further knowledge on electrode characteristics and stimulation parameters, performance of the circuit can be improved. Moreover, the difference between monopolar and bipolar intracortical stimulation should be researched. With a better understanding of the expected stimulation intensity and electrode parameters, a power budget for the complete system could be established.

- **Energy efficiency UHF waveform -** An analytical study with a neuron model should be done to get insight in the energy efficiency of UHF stimulation. This analysis could help to determine an optimal switching frequency for this stimulation method and to compare the technique to conventional current mode stimulation.

- ***In vitro* measurements with characterized electrodes -** The measurements presented in this thesis have shown that the circuit is compatible with a non-linear load impedance. However, the electrodes used for these measurements were not optimal for the system. Using well characterized electrodes, the complete performance of the circuit can be tested.

- **High voltage stimulator driver -** With the presented work, it has become clear that high supply voltage is required for the stimulator in this application. A high voltage driver should be designed to generate the voltage from incoming wireless power.

- **System improvements:**

  - The system should be able to detect when Q_{ph} is limited because the tissue impedance is too high. Detecting this error could be implemented with monitoring the control signal Q.
  - The measurements have shown that it is important to minimize the parasitic capacitance at V_{sense} to improve system performance. Also, cross-talk between the channels should be minimized with careful design of the H-bridge traces as well as the leads connecting the electrodes.

  - For low stimulation intensity, power efficiency as well as charge accuracy is affected because of the high stimulation voltage. A scalable stimulation voltage could improve the system performance for low stimulation intensity.
  - Last, FPGA control of the circuit could be improved. In the current design, two separate VHDL codes are used to switch between single- and multi-channel mode. Moreover, external pins are used for configuration of the stimulation signal. The FPGA module has an on-board usb-UART interface which could be used to communicate with the stimulator. Improvement of the VHDL code is beneficial for future *in vitro* and *in vivo* measurements with the PCB.

- **Integrated Circuit implementation -** Eventually, the circuit should be integrated to create an implantable device. On the IC, multiple of the proposed stimulation sources should be combined with integrated control logic and power management circuitry. The size of C_{sense} will be limited with the available area on the IC. To scale the circuit, C_{sense} should be chosen as large as possible. Consequently, f_{sw} and V_{ref} can be scaled according to the stimulation requirements.

Bibliography

[1] W. H. Dobelle, W. H. Dobelle, D. O. Quest, J. L. Antunes, T. S. Roberts, and J. P. Girvin, "Artificial Vision for the Blind by Electrical Stimulation of the Visual Cortex," *Neurosurgery*, vol. 5, no. 4, pp. 521–527, 10 1979. [Online]. Available: https://academic.oup.com/neurosurgery/article/5/4/521/2746552

[2] E. Fernandez and R. Normann, "Introduction to Visual Prostheses," in *Webvision: The Organization of the Retina and Visual System*, Salt Lake City (UT): University of Utah Health, 2016. [Online]. Available: http://www.ncbi.nlm.nih.gov/pubmed/27809426

[3] J. Sommerhalder and A. Pérez Fornos, "Prospects and Limitations of Spatial Resolution," in *Artificial Vision*, V. P. Gabel, Ed. Springer International Publishing, 2017, pp. 29–45. [Online]. Available: http://link.springer.com/10.1007/978-3-319-41876-6_4

[4] C. Stangor and J. Walinga, *Introduction to Psychology - 1st Canadian Edition*. BCcampus, 2010. [Online]. Available: https://opentextbc.ca/introductiontopsychology/

[5] M. Schmolesky, "The Primary Visual Cortex," in *Webvision: The Organization of the Retina and Visual System*. Salt Lake City (UT): University of Utah Health: Elsevier, 2005, pp. 1039–1070. [Online]. Available: https://www.ncbi.nlm.nih.gov/books/NBK11524/pdf/Bookshelf_NBK11524.pdf

[6] E. Genç, J. Bergmann, W. Singer, and A. Kohler, "Surface Area of Early Visual Cortex Predicts Individual Speed of Traveling Waves During Binocular Rivalry," *Cerebral Cortex*, vol. 25, no. 6, pp. 1499–1508, 6 2015. [Online]. Available: https://academic.oup.com/cercor/article-lookup/doi/10.1093/cercor/bht342

[7] Opthamology Training, "Visual Cortex," (accessed: Nov. 10, 2020). [Online]. Available: https://www.ophthalmologytraining.com/core-principles/ocular-anatomy/visual-pathway/visual-cortex

[8] S. Niketeghad and N. Pouratian, "Brain Machine Interfaces for Vision Restoration: The Current State of Cortical Visual Prosthetics," *Neurotherapeutics*, vol. 16, no. 1, pp. 134–143, 1 2019. [Online]. Available: http://link.springer.com/10.1007/s13311-018-0660-1

[9] P. M. Lewis, H. M. Ackland, A. J. Lowery, and J. V. Rosenfeld, "Restoration of vision in blind individuals using bionic devices: A review with a focus on cortical visual prostheses," *Brain Research*, vol. 1595, pp. 51–73, 1 2015. [Online]. Available: http://dx.doi.org/10.1016/j.brainres.2014.11.020https://linkinghub.elsevier.com/retrieve/pii/S0006899314015674

[10] S. Hanneton, M. Auvray, and B. Durette, "The Vibe: a versatile vision-to-audition sensory substitution device," *Applied Bionics and Biomechanics*, vol. 7, no. 4, pp. 269–276, 12 2010. [Online]. Available: http://content.iospress.com/doi/10.1080/11762322.2010.512734

[11] O. Deroy and M. Auvray, "Reading the World through the Skin and Ears: A New Perspective on Sensory Substitution," *Frontiers in Psychology*, vol. 3, no. NOV, pp. 1–13, 2012. [Online]. Available: http://journal.frontiersin.org/article/10.3389/fpsyg.2012.00457/abstract

[12] A. Najarpour Foroushani, C. C. Pack, and M. Sawan, "Cortical visual prostheses: from microstimulation to functional percept," *Journal of Neural Engineering*, vol. 15, no. 2, p. 021005, 4 2018. [Online]. Available: https://doi.org/10.1088/1741-2552/aaa904https://iopscience.iop.org/article/10.1088/1741-2552/aaa904

[13] E. M. Schmidt, M. J. Bak, F. T. Hambrecht, C. V. Kufta, D. K. O'Rourke, and P. Vallabhanath, "Feasibility of a visual prosthesis for the blind based on intracortical micro stimulation of the visual cortex," *Brain*, vol. 119, no. 2, pp. 507–522, 1996. [Online]. Available: https://academic.oup.com/brain/article-lookup/doi/10.1093/brain/119.2.507

[14] K. Cha, K. Horch, and R. A. Normann, “Simulation of a phosphene-based visual field: Visual acuity in a pixelized vision system,” *Annals of Biomedical Engineering*, vol. 20, no. 4, pp. 439–449, 7 1992. [Online]. Available: http://link.springer.com/10.1007/BF02368135

[15] M. Piedade, J. Gerald, L. Sousa, G. Tavares, and P. Tomas, “Visual neuroprosthesis: a non invasive system for stimulating the cortex,” *IEEE Transactions on Circuits and Systems I: Regular Papers*, vol. 52, no. 12, pp. 2648–2662, 12 2005. [Online]. Available: http://ieeexplore.ieee.org/document/1556773/

[16] E. Fernández, F. Pelayo, S. Romero, M. Bongard, C. Marin, A. Alfaro, and L. Merabet, “Development of a cortical visual neuroprosthesis for the blind: the relevance of neuroplasticity,” *Journal of Neural Engineering*, vol. 2, no. 4, pp. R1–R12, 12 2005. [Online]. Available: https://iopscience.iop.org/article/10.1088/1741-2560/2/4/R01

[17] J. Coulombe, M. Sawan, and J.-F. Gervais, “A Highly Flexible System for Microstimulation of the Visual Cortex: Design and Implementation,” *IEEE Transactions on Biomedical Circuits and Systems*, vol. 1, no. 4, pp. 258–269, 12 2007. [Online]. Available: http://ieeexplore.ieee.org/document/4432298/

[18] K. Cha, K. W. Horch, and R. A. Normann, “Mobility performance with a pixelized vision system,” *Vision Research*, vol. 32, no. 7, pp. 1367–1372, 7 1992. [Online]. Available: https://linkinghub.elsevier.com/retrieve/pii/004269899290229C

[19] K. Torab, T. S. Davis, D. J. Warren, P. A. House, R. A. Normann, and B. Greger, “Multiple factors may influence the performance of a visual prosthesis based on intracortical microstimulation: nonhuman primate behavioural experimentation,” *Journal of Neural Engineering*, vol. 8, no. 3, p. 035001, 6 2011. [Online]. Available: https://iopscience.iop.org/article/10.1088/1741-2560/8/3/035001

[20] J. Malmivuo and R. Plonsey, *Bioelectromagnetism: Principles and Applications of Bioelectric and Biomagnetic Fields*. Oxford University Press, 10 1995, vol. 15, no. 1. [Online]. Available: https://oxford.universitypressscholarship.com/view/10.1093/acprof:oso/9780195058239.001.0001/acprof-9780195058239

[21] “Membrane Potential, Ion Transport and Nerve Impulse,” 2009, (accessed: Nov. 10, 2020). [Online]. Available: https://wikispaces.psu.edu/display/230/Membrane+Potential%2C+Ion+Transport+and+Nerve+Impulse

[22] D. R. Merrill, M. Bikson, and J. G. Jefferys, “Electrical stimulation of excitable tissue: Design of efficacious and safe protocols,” pp. 171–198, 2005. [Online]. Available: https://www.sciencedirect.com/science/article/abs/pii/S0165027004003826

[23] P. H. Gorman and J. T. Mortimer, “The Effect of Stimulus Parameters on the Recruitment Characteristics of Direct Nerve Stimulation,” *IEEE Transactions on Biomedical Engineering*, vol. BME-30, no. 7, pp. 407–414, 7 1983. [Online]. Available: http://ieeexplore.ieee.org/document/4121663/

[24] J. Simpson and M. Ghovanloo, “An Experimental Study of Voltage, Current, and Charge Controlled Stimulation Front-End Circuitry,” in *2007 IEEE International Symposium on Circuits and Systems*. IEEE, 5 2007, pp. 325–328. [Online]. Available: https://ieeexplore.ieee.org/document/4252637/

[25] M. N. van Dongen and W. A. Serdijn, “A Power-Efficient Multichannel Neural Stimulator Using High-Frequency Pulsed Excitation From an Unfiltered Dynamic Supply,” *IEEE Transactions on Biomedical Circuits and Systems*, vol. 10, no. 1, pp. 61–71, 2 2016. [Online]. Available: http://ieeexplore.ieee.org/document/6965660/

[26] S. K. Kelly and J. L. Wyatt, “A Power-Efficient Neural Tissue Stimulator With Energy Recovery,” *IEEE Transactions on Biomedical Circuits and Systems*, vol. 5, no. 1, pp. 20–29, 2 2011. [Online]. Available: http://ieeexplore.ieee.org/document/5701725/

[27] W.-Y. Hsu and A. Schmid, “Compact, Energy-Efficient High-Frequency Switched Capacitor Neural Stimulator With Active Charge Balancing,” *IEEE Transactions on Biomedical Circuits and Systems*, vol. 11, no. 4, pp. 878–888, 8 2017. [Online]. Available: http://ieeexplore.ieee.org/document/7982639/

[28] L. Tacchetti, W. A. Serdijn, and V. Giagka, “An Ultrasonically Powered and Controlled Ultra-High-Frequency Biphasic Electrical Neurostimulator,” in *2018 IEEE Biomedical Circuits and Systems Conference (BioCAS)*, no. January 2019. IEEE, 10 2018, pp. 1–4. [Online]. Available: https://ieeexplore.ieee.org/document/8584718/

[29] M. Ghovanloo and K. Najafi, “A Compact Large Voltage-Compliance High Output-Impedance Programmable Current Source for Implantable Microstimulators,” *IEEE Transactions on Biomedical Engineering*, vol. 52, no. 1, pp. 97–105, 1 2005. [Online]. Available: http://ieeexplore.ieee.org/document/1369592/

[30] P. B. Matteucci, S. C. Chen, D. Tsai, C. W. D. Dodds, S. Dokos, J. W. Morley, N. H. Lovell, and G. J. Suaning, “Current Steering in Retinal Stimulation via a Quasimonopolar Stimulation Paradigm,” *Investigative Opthalmology & Visual Science*, vol. 54, no. 6, p. 4307, 6 2013. [Online]. Available: http://iovs.arvojournals.org/article.aspx?doi=10.1167/iovs.13-11653

[31] D. Jiang and A. Demosthenous, “A Multichannel High-Frequency Power-Isolated Neural Stimulator With Crosstalk Reduction,” *IEEE Transactions on Biomedical Circuits and Systems*, vol. 12, no. 4, pp. 940–953, 8 2018. [Online]. Available: https://ieeexplore.ieee.org/document/8370051/

[32] C.-Y. Lin and M.-D. Ker, “Overview of On-Chip Stimulator Designs for Biomedical Applications,” *Journal of Neuroscience and Neuroengineering*, vol. 1, no. 2, pp. 204–212, 12 2012.

[33] M. Ghovanloo, K. Wise, and K. Najafi, “Towards a button-sized 1024-site wireless cortical microstimulating array,” in *First International IEEE EMBS Conference on Neural Engineering, 2003. Conference Proceedings.*, vol. 2003-Janua, no. June. IEEE, 2003, pp. 138–141. [Online]. Available: http://ieeexplore.ieee.org/document/1196776/

[34] M. Hasanuzzaman, B. G. Motlagh, F. Mounaim, A. Hassan, R. Raut, and M. Sawan, “Toward an Energy-Efficient High-Voltage Compliant Visual Intracortical Multichannel Stimulator,” *IEEE Transactions on Very Large Scale Integration (VLSI) Systems*, vol. 26, no. 5, pp. 878–891, 5 2018. [Online]. Available: https://ieeexplore.ieee.org/document/8294053/

[35] P. R. Troyk, D. E. Detlefsen, and G. A. DeMichele, “A 16-channel stimulator ASIC for use in an intracortical visual prosthesis,” *10th Annual Conference of the International FES Society*, no. July, pp. 1–2, 2005.

[36] S. Kim, T. Callier, and S. J. Bensmaia, “A Computational Model That Predicts Behavioral Sensitivity to Intracortical Microstimulation,” *Journal of Neural Engineering*, vol. 14, no. 1, p. 016012, 2 2017. [Online]. Available: https://iopscience.iop.org/article/10.1088/1741-2552/14/1/016012

[37] T. S. Davis, R. A. Parker, P. A. House, E. Bagley, S. Wendelken, R. A. Normann, and B. Greger, “Spatial and temporal characteristics of V1 microstimulation during chronic implantation of a microelectrode array in a behaving macaque,” *Journal of Neural Engineering*, vol. 9, no. 6, p. 065003, 12 2012. [Online]. Available: https://iopscience.iop.org/article/10.1088/1741-2560/9/6/065003

[38] E. A. DeYoe, J. D. Lewine, and R. W. Doty, “Laminar Variation in Threshold for Detection of Electrical Excitation of Striate Cortex by Macaques,” *Journal of Neurophysiology*, vol. 94, no. 5, pp. 3443–3450, 11 2005. [Online]. Available: https://www.physiology.org/doi/10.1152/jn.00407.2005

[39] E. J. Tehovnik and W. M. Slocum, “Depth-dependent detection of microampere currents delivered to monkey V1,” *European Journal of Neuroscience*, vol. 29, no. 7, pp. 1477–1489, 4 2009. [Online]. Available: http://doi.wiley.com/10.1111/j.1460-9568.2009.06695.x

[40] R. Normann, “A penetrating, cortical electrode array: design considerations,” in *1990 IEEE International Conference on Systems, Man, and Cybernetics Conference Proceedings*. IEEE, 1990, pp. 918–920. [Online]. Available: http://ieeexplore.ieee.org/document/142258/

[41] P. Campbell, K. Jones, R. Huber, K. Horch, and R. Normann, “A silicon-based, three-dimensional neural interface: manufacturing processes for an intracortical electrode array,” *IEEE Transactions on Biomedical Engineering*, vol. 38, no. 8, pp. 758–768, 1991. [Online]. Available: http://ieeexplore.ieee.org/document/83588/

[42] Blackrock Microsystems, “The benchmark for multichannel, high-density neural recording,” (accessed: Jun. 26, 2020). [Online]. Available: https://www.blackrockmicro.com/electrode-types/utah-array/

[43] E. M. Maynard, C. T. Nordhausen, and R. A. Normann, “The Utah Intracortical Electrode Array: A recording structure for potential brain-computer interfaces,” *Electroencephalography and Clinical Neurophysiology*, vol. 102, no. 3, pp. 228–239, 3 1997. [Online]. Available: https://linkinghub.elsevier.com/retrieve/pii/S0013469496951760

[44] S. Ethier, M. Sawan, E. M. Aboulhamid, and M. El-Gamal, “A ±9 V fully integrated CMOS electrode driver for high-impedance microstimulation,” in *Midwest Symposium on Circuits and Systems*. IEEE, 8 2009, pp. 192–195. [Online]. Available: http://ieeexplore.ieee.org/document/5236121/

[45] M. Straka, B. Shafer, S. Vasudevan, C. Welle, and L. Rieth, “Characterizing Longitudinal Changes in the Impedance Spectra of In-Vivo Peripheral Nerve Electrodes,” *Micromachines*, vol. 9, no. 11, p. 587, 11 2018. [Online]. Available: http://www.mdpi.com/2072-666X/9/11/587

[46] Y. T. Wong, T. Feleppa, A. Mohan, D. Browne, J. Szlawski, J. V. Rosenfeld, and A. Lowery, “CMOS stimulating chips capable of wirelessly driving 473 electrodes for a cortical vision prosthesis,” *Journal of Neural Engineering*, vol. 16, no. 2, p. 026025, 4 2019. [Online]. Available: https://iopscience.iop.org/article/10.1088/1741-2552/ab021b

[47] A. Urso, V. Giagka, M. van Dongen, and W. A. Serdijn, “An Ultra High-Frequency 8-Channel Neurostimulator Circuit With 68% Peak Power Efficiency,” *IEEE Transactions on Biomedical Circuits and Systems*, vol. 13, no. 5, pp. 882–892, 10 2019. [Online]. Available: https://ieeexplore.ieee.org/document/8727437/

[48] I. Williams and T. G. Constandinou, “An Energy-Efficient, Dynamic Voltage Scaling Neural Stimulator for a Proprioceptive Prosthesis,” *IEEE Transactions on Biomedical Circuits and Systems*, vol. 7, no. 2, pp. 129–139, 4 2013. [Online]. Available: http://ieeexplore.ieee.org/document/6508875/

[49] Z. Luo, M.-D. Ker, T.-Y. Yang, and W.-H. Cheng, “A Digitally Dynamic Power Supply Technique for 16-Channel 12 V-Tolerant Stimulator Realized in a 0.18- μm 1.8-V/3.3-V Low-Voltage CMOS Process,” *IEEE Transactions on Biomedical Circuits and Systems*, vol. 11, no. 5, pp. 1087–1096, 10 2017. [Online]. Available: http://ieeexplore.ieee.org/document/7983416/

[50] A. Rashidi, N. Yazdani, and A. M. Sodagar, “Fully-implantable, multi-channel, microstimulator with tracking supply ribbon and energy recovery,” in *2016 38th Annual International Conference of the IEEE Engineering in Medicine and Biology Society (EMBC)*, vol. 2016-Octob. IEEE, 8 2016, pp. 1818–1821. [Online]. Available: http://ieeexplore.ieee.org/document/7591072/

[51] S. Ha, A. Akinin, J. Park, C. Kim, H. Wang, C. Maier, G. Cauwenberghs, and P. P. Mercier, “A 16-channel wireless neural interfacing SoC with RF-powered energy-replenishing adiabatic stimulation,” in *2015 Symposium on VLSI Circuits (VLSI Circuits)*, vol. 2015-Augus, no. c. IEEE, 6 2015, pp. C106–C107. [Online]. Available: http://ieeexplore.ieee.org/document/7231341/

[52] S. F. Cogan, “Neural Stimulation and Recording Electrodes,” *Annual Review of Biomedical Engineering*, vol. 10, no. 1, pp. 275–309, 8 2008. [Online]. Available: http://www.annualreviews.org/doi/10.1146/annurev.bioeng.10.061807.160518

[53] M. Schwarz and M. Maschmann, “Area saving stimulator cells for multielectrode arrays featuring adaptive waveform generation and monitoring,” in *The 26th Annual International Conference of the IEEE Engineering in Medicine and Biology Society*, vol. 4. IEEE, 2004, pp. 4314–4317. [Online]. Available: http://ieeexplore.ieee.org/document/1404201/

[54] S. K. Arfin and R. Sarpeshkar, “An Energy-Efficient, Adiabatic Electrode Stimulator With Inductive Energy Recycling and Feedback Current Regulation,” *IEEE Transactions on Biomedical Circuits and Systems*, vol. 6, no. 1, pp. 1–14, 2 2012. [Online]. Available: http://ieeexplore.ieee.org/document/6036003/

[55] M. N. van Dongen and W. A. Serdijn, “A transistor-only power-efficient high-frequency voltage-mode stimulator for a multichannel system,” in *2013 IEEE Biomedical Circuits and Systems Conference (BioCAS)*. IEEE, 10 2013, pp. 93–96. [Online]. Available: http://ieeexplore.ieee.org/document/6679647/

[56] M. N. van Dongen, F. E. Hoebeek, S. K. E. Koekkoek, C. I. De Zeeuw, and W. A. Serdijn, “Efficacy of high frequency switched-mode stimulation in activating Purkinje cells,” 2014. [Online]. Available: http://arxiv.org/abs/1406.7185

[57] M. N. van Dongen and W. A. Serdijn, “Design of a low power 100 dB dynamic range integrator for an implantable neural stimulator,” in *2010 IEEE Biomedical Circuits and Systems Conference, BioCAS 2010*. IEEE, 11 2010, pp. 158–161. [Online]. Available: http://ieeexplore.ieee.org/document/5709595/

[58] F. Kolbl, R. Guillaume, J. Hasler, S. Joucla, B. Yvert, S. Renaud, and N. Lewis, “A closed-loop charge balancing FPAA circuit with sub-nano-amp DC error for electrical stimulation,” in *2014 IEEE Biomedical Circuits and Systems Conference (BioCAS) Proceedings*. IEEE, 10 2014, pp. 616–619. [Online]. Available: http://ieeexplore.ieee.org/document/6981801/

[59] R. Ranjandish, O. Shoaei, and A. Schmid, “A Fully Fail-Safe Capacitive-Based Charge Metering Method for Active Charge Balancing in Deep Brain Stimulation,” in *2018 14th Conference on Ph.D. Research in Microelectronics and Electronics (PRIME)*. IEEE, 7 2018, pp. 249–252. [Online]. Available: https://ieeexplore.ieee.org/document/8430327/

[60] S. Luan and T. G. Constandinou, “A charge-metering method for voltage-mode neural stimulation,” *Journal of Neuroscience Methods*, vol. 224, pp. 39–47, 3 2014. [Online]. Available: https://linkinghub.elsevier.com/retrieve/pii/S0165027013004172

[61] X. Fang, J. Wills, J. Granacki, J. LaCoss, A. Arakelian, and J. Weiland, “Novel Charge-Metering Stimulus Amplifier for Biomimetic Implantable Prosthesis,” in *2007 IEEE International Symposium on Circuits and Systems*, no. 07. IEEE, 5 2007, pp. 569–572. [Online]. Available: http://ieeexplore.ieee.org/lpdocs/epic03/wrapper.htm?arnumber=4252698http://ieeexplore.ieee.org/document/4252698/

[62] K. Sooksood, T. Stieglitz, and M. Ortmanns, “An experimental study on passive charge balancing,” *Advances in Radio Science*, vol. 7, pp. 197–200, 5 2009. [Online]. Available: https://www.adv-radio-sci.net/7/197/2009/

[63] M. Ortmanns, A. Rocke, M. Gehrke, and H.-J. Tiedtke, “A 232-Channel Epiretinal Stimulator ASIC,” *IEEE Journal of Solid-State Circuits*, vol. 42, no. 12, pp. 2946–2959, 12 2007. [Online]. Available: http://ieeexplore.ieee.org/document/4381458/

[64] C. Rathna, “PI controller scheme for charge balance in implantable electrical stimulators,” *Sadhana - Academy Proceedings in Engineering Sciences*, vol. 41, no. 1, pp. 31–45, 1 2016. [Online]. Available: http://link.springer.com/10.1007/s12046-016-0461-3

[65] L. Zheng, S. Shin, and S.-M. S. Kang, “Design of a neural stimulator system with closed-loop charge cancellation,” in *2012 IEEE/IFIP 20th International Conference on VLSI and System-on-Chip (VLSI-SoC)*, vol. 07-10-Octo. IEEE, 10 2012, pp. 1–6. [Online]. Available: http://ieeexplore.ieee.org/document/7332067/

[66] L. Yao, P. Li, and M. Je, “A pulse-width-adaptive active charge balancing circuit with pulse-insertion based residual charge compensation and quantization for electrical stimulation applications,” in *2015 IEEE Asian Solid-State Circuits Conference (A-SSCC)*. IEEE, 11 2015, pp. 1–4. [Online]. Available: http://ieeexplore.ieee.org/document/7387478/

[67] R. Ranjandish and A. Schmid, “An active charge balancing method based on self-oscillation of the anodic current,” in *2016 IEEE Biomedical Circuits and Systems Conference (BioCAS)*. IEEE, 10 2016, pp. 496–499. [Online]. Available: http://ieeexplore.ieee.org/document/7833840/

[68] R. Ranjandish and O. Shoaei, “A simple and precise charge balancing method for voltage mode stimulation,” in *2014 IEEE Biomedical Circuits and Systems Conference (BioCAS) Proceedings*. IEEE, 10 2014, pp. 376–379. [Online]. Available: http://ieeexplore.ieee.org/document/6981741/

[69] E. Maghsoudloo, M. Rezaei, M. Sawan, and B. Gosselin, “A new charge balancing scheme for electrical microstimulators based on modulated anodic stimulation pulse width,” in *2016 IEEE International Symposium on Circuits and Systems (ISCAS)*, vol. 2016-July. IEEE, 5 2016, pp. 2443–2446. [Online]. Available: https://ieeexplore.ieee.org/document/7539086

[70] K. Sooksood, T. Stieglitz, and M. Ortmanns, “An Active Approach for Charge Balancing in Functional Electrical Stimulation,” *IEEE Transactions on Biomedical Circuits and Systems*, vol. 4, no. 3, pp. 162–170, 6 2010. [Online]. Available: http://ieeexplore.ieee.org/document/5406039/

[71] S. Kameda, Y. Hayashida, Y. Tanaka, D. Akita, and T. Yagi, “A multichannel current stimulator chip for spatiotemporal pattern stimulation of neural tissues,” in *2014 36th Annual International Conference of the IEEE Engineering in Medicine and Biology Society*. IEEE, 8 2014, pp. 5011–5015. [Online]. Available: http://ieeexplore.ieee.org/document/6944750/

[72] C. Verhoeven, “First order oscillators,” Ph.D. dissertation, Delft University of Technology, 1990. [Online]. Available: https://repository.tudelft.nl/islandora/object/uuid%3Aadf76c81-fb5d-45d7-b8ce-4428bd10c6b0

[73] B. P. Wong, A. Mittal, Y. Cao, and G. Starr, *Nano-CMOS Circuit and Physical Design*. Hoboken, NJ, USA: John Wiley & Sons, Inc., 11 2004. [Online]. Available: http://doi.wiley.com/10.1002/0471653829

[74] G. L. E. Rueda, M. Ballini, N. Van Hellepute, and S. Mitra, “Analysis of passive charge balancing for safe current-mode neural stimulation,” in *2017 IEEE International Symposium on Circuits and Systems (ISCAS)*. IEEE, 5 2017, pp. 1–4. [Online]. Available: http://ieeexplore.ieee.org/document/8050621/

[75] NeuroNexus, “Electrode Arrays A1x32-5mm-25-177,” (accessed: Oct. 24, 2020). [Online]. Available: https://neuronexus.com/electrode-array/a1x32-5mm-25-177/

[76] M. Sahin and Y. Tie, “Non-rectangular waveforms for neural stimulation with practical electrodes.” in *Journal of neural engineering*, 9 2007, vol. 4, no. 3, pp. 227–233. [Online]. Available: https://iopscience.iop.org/article/10.1088/1741-2560/4/3/008